55
2/12/92 JS (2)

PREPARED FOR THE U.S. DEPARTMENT OF ENERGY,
UNDER CONTRACT DE-AC02-76-CHO-3073

PPPL-2812
UC-420,426

PPPL-2812

MeV ION LOSS DURING ^{3}He MINORITY HEATING IN TFTR

BY

S.J. ZWEBEN, G. HAMMETT, R. BOIVIN, C. PHILLIPS, AND R. WILSON.

January 1992

PPPL
PRINCETON
PLASMA PHYSICS
LABORATORY

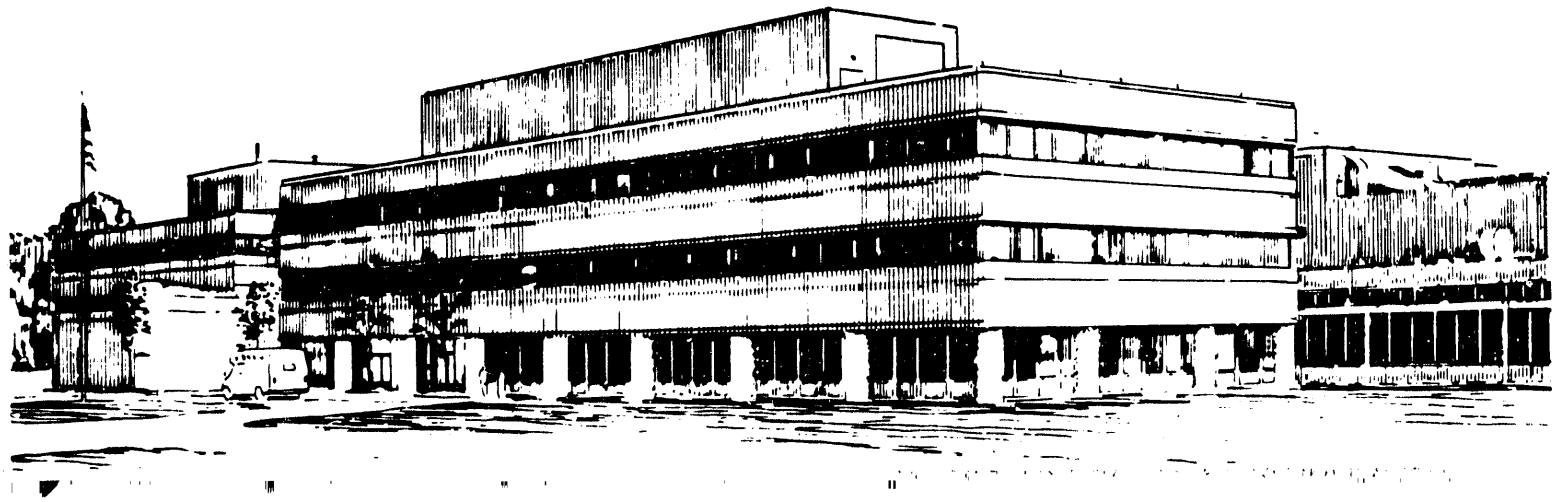

NOTICE

NOTICE

PPPL--2812

DE92 006655

MeV Ion Loss During ^{3}He Minority Heating in TFTR

S.J. Zweben, G. Hammett, R. Boivin, C. Phillips, R. Wilson

Abstract

The loss of MeV ions during ^{3}He ICRH minority heating experiments has been measured using scintillator detectors near the wall of TFTR. The observed MeV ion losses to the bottom (90^0 poloidal) detector are generally consistent with the expected first-orbit loss of D-^{3}He alpha particle fusion products, with an inferred global reaction rate up to $\approx 10^{16}$ reactions/sec. A qualitatively similar but unexpectedly large loss occurs 45^0 poloidally below the outer midplane. This additional loss might be due to ICRH tail ions or to ICRH wave-induced loss of previously confined fusion products.

1. Introduction

The fusion reaction D+^{3}He->p(14.6 MeV)+α(3.7 MeV) creates an alpha particle with nearly the same energy as in D+T->n(14.1 MeV)+α(3.5 MeV). Therefore alpha particle confinement and loss measurements in D-^{3}He plasmas are of considerable interest for anticipating and planning the upcoming D-T experiments in TFTR and JET (and future D-T tokamaks).

D-^{3}He fusion reaction rates equal to or higher than the best D-D reaction rates have recently been obtained in JET[1] as a by-product ^{3}He minority Ion Cyclotron Resonance Heating (ICRH), and similar ^{3}He ICRH experiments have been performed at TFTR [2]. This paper describes measurements and modeling of MeV ion losses observed during the 1990 ^{3}He ICRH experiments on TFTR. These are the most extensive measurements to date of alpha particle loss from a tokamak.

An advantage of using D-^{3}He alphas for simulating D-T alpha particle physics is that the experiments can be done without the possibly large background due to the D-T neutrons, well before the D-T experiments on TFTR. The main disadvantage of D-^{3}He is that the achievable reaction rates with ^{3}He ICRF minority heating are only about 1% of those which can be obtained in the same machine with D-T, so that a full study of collective alpha effects[3] is apparently not possible. However, that the D-^{3}He reaction rate might be increased to about 10% that of D-T by using an injected 0.5 MeV beam instead of the ICRH tail, as proposed recently for JT-60-U[4].

Another disadvantage of D-^{3}He is that the reaction rate can not be diagnosed using neutrons as it can be in D-T (and D-D). Although considerable information has been obtained at JET[5] by measuring the γ emission from the weak secondary branch of the reaction D+^{3}He-> γ(16.6 MeV)+^{5}Li, this information is yet not routinely available on TFTR[6]. Therefore the D-^{3}He reaction rate (and particularly its profile)

are not directly measured for the TFTR discharges described in this paper.

Nevertheless, some interesting results have been obtained using the escaping MeV ion detectors previously used for D-D experiments[7], which are also to be used for D-T. This paper begins in Sec. 2 with a discussion of several possible loss mechanisms for MeV ions during ^{3}He minority ICRH. Section 3 contains a brief review of previous results and a description of the present TFTR MeV ion loss detectors. The new measurements of the MeV ion loss are discussed in Sec. 4, and some modeling pertaining to these results is in Sec. 5. Note that ICRH *hydrogen* minority heated discharges have a very different behavior with respect to MeV ion loss, and will be discussed elsewhere.

2. Mechanisms of MeV Ion Loss During ICRH

There are at least three possible mechanisms for ICRH-induced MeV ion loss during these ^{3}He minority heating experiments (in addition to the usual first-orbit and MHD-induced D-D fusion product loss described previously for TFTR NBI experiments [7]), namely:

1) first-orbit loss of the D-^{3}He fusion products,
2) loss of the high energy part of the ^{3}He minority tail itself, and
3) ICRH-wave-induced deconfinement of fusion products.

The first mechanism is the simplest one, in which D-^{3}He charged fusion products are lost on their first orbits similarly to D-D fusion products[7]. Since the gyroradius of the 3.7 MeV D-^{3}He alpha particle is only about 10% larger than that of the 1 MeV triton or 3 MeV proton from D-D reactions, the alpha particle first-orbit loss characteristics (e.g. the pitch angle distribution) should be approximately the same as those for D-D fusion products (although the fusion product source profile

could differ between ICRF-minority and NBI heating). Note that the first-orbit loss of the 14.6 MeV protons from D-^{3}He should always accompany the first-orbit loss of the 3.7 MeV alphas (see Sec. 4.3).

The second MeV ion loss mechanism is direct loss of the high energy minority tail ions, as previously seen in *hydrogen* minority ICRH experiments in PLT[8] and TFTR[9]. This can not be "first-orbit" loss, since these tail ions are gradually accelerated up to MeV energies by the RF fields, although some neoclassical loss is possible[10]. Since the energy input into the minority tail is usually $>10^2$ times larger than the energy output in D-^{3}He fusion reactions (corresponding to $Q<.01$), this direct tail loss could be considerably larger than the first-orbit fusion product alpha loss (in terms of lost ions/sec). However, in JET[1,5] the tail confinement appears to be consistent with classical expectations (i.e. no detectable diffusion or loss), and no clear evidence for ^{3}He minority tail loss has yet been found in either JET or TFTR.

The third possible MeV ion loss mechanism is due to ICRH-wave-induced deconfinement of previously confined D-D or D-^{3}He fusion products, i.e. due to the perturbing effect of the electric and/or magnetic fields associated with the RF waves themselves. For example, during ^{3}He minority heating the RF waves might also heat 1 MeV tritons at their second harmonic. The ICRH-wave-induced transport of the minority tail itself has been calculated[11], and an RF-induced radial transport of partially thermalized alphas has been proposed as an ash removal mechanism for tokamaks[12]. Such an RF-wave-driven diffusion of D-D or D-^{3}He fusion products might be occurring in the present experiment, as discussed at the end of Sec. 4.6.

It is important to emphasize that the high energy part of the ^{3}He minority tail can have some properties in common with the fusion-produced D-^{3}He alpha particles. For example, the creation rate of D-^{3}He alphas is proportional to the population of the high energy ^{3}He ions (at a few-hundred keV), implying that the time dependences of their

creation and loss during a discharge could be similar. Both species also can have a similar energy distribution function inside the plasma (although it is unlikely that the tail ions loss would occur only near the first-orbit loss energy of the alphas). Furthermore, any ICRH-wave-induced deconfinement process would most likely affect both types of ions similarly. Thus the process of experimentally distinguishing between these three loss mechanisms within a particular ICRH+NBI discharge can be non-trivial, particularly with detectors like ours which are not sensitive to species differences, e.g. between ^{3}He, ^{4}He, and ^{1}H (only to gyroradii).

Note, incidentally, that small source rates of both 3.5 MeV D-T alphas and 3.7 MeV D-^{3}He alphas are also present with D-D NBI due the burnup of the 1.0 MeV triton and 0.8 MeV ^{3}He ions normally created by D-D fusion reactions. However, these source rates are typically only 1% of the D-D source rate and so are not separately observable in the present experiments, which are dominated by either D-D or ICRH-induced D-^{3}He fusion products. Also, a source of alphas due to D injected ions reacting with thermal ^{3}He should also be present (proportional to the D-D source rate), but since the cross section for beam-target D-^{3}He is about x2 less than that for D-D, and since the density of thermal ^{3}He is $<<10\%$ than that of thermal D, then this D-^{3}He reaction rate should be $<<5\%$ that the D-D reaction rate, which is negligible in the present experiments.

3. MeV Ion Loss Detectors

The first and up to now the only measurements of MeV alpha loss in a tokamak were done on ICRH-heated D-^{3}He plasmas in PLT using a time-integrating plastic track detector[13]. In that experiment the plasma current was only about 600 kA, therefore even alphas created near the plasma center could escape from the plasma and be detected at

the wall.

However, several measurements have been made of the loss of 14.6 MeV protons from the D-^{3}He reaction, such as those on PLT[14], PDX[15], TFTR[16], and JET[17]. In these experiments the 14.6 MeV proton was measured using a silicon surface barrier detector, which has good energy resolution but little or no pitch angle resolution. For Refs. [15-16] the 14.7 MeV protons came from the burnup of the ^{3}He created by D-D reactions, while for Refs. [13-14] and [17] the protons were created during ICRH minority heating of ^{3}He. In PLT[14] and to a greater extent in JET[17] the proton loss during ICRH ^{3}He minority heating was observed to be strongly modulated by sawteeth.

The location and design of the scintillation detectors for the present TFTR experiment is shown in Figs. 1 and 2. Their pinhole/slit aperture is similar to that used in PLT[13], but the track detector is replaced by a ZnS(Ag) scintillator screen in order to form a time-resolved 2-D image the lost MeV ions on the scintillator plane. The ions are internally dispersed by the aperture pair according to their toroidal pitch angle χ (i.e. magnetic moment) in one direction and their gyroradius (i.e. energy) in the other. The 3μ aluminum foil behind the slit aperture blocks low energy ions (e.g. alphas <1 MeV) and plasma light. This detector design and associated detector orbit calculations have been discussed previously in the context of D-D fusion product loss measurements[7].

For TFTR plasma currents of interest (1-2 MA), the first-orbit loss of 3.7 MeV D-^{3}He alphas should come from radii typically $r/a>0.3$, similar to D-D fusion products. It would be interesting to simultaneously measure the loss of the 14.6 MeV protons, since their first-orbit loss should come from regions nearer to the magnetic axis. However the present scintillator was not designed for this, and is too thin to respond to the 14.6 MeV protons (see Sec. 4.3).

The scintillator light emission from the present TFTR alpha detectors is monitored either with an intensified video camera or a bank of photomultiplier tubes (but not both together). The camera provides 2-D images of the scintillator plane at a rate of up to 60 frames/sec (presently digitized at 30 fields/sec), while the PM tubes provide much faster time response (≈20 kHz), but for only a few points within the 2-D image.

4. Measurements of MeV Ion Loss During ^{3}He Minority Heating

This section describes MeV ion loss measurements made with ^{3}He minority heating during the 1990 TFTR run. Several different conditions of plasma current and different mixes of auxiliary power (ICRF and NBI) were investigated, as summarized in Table 1. Except for Secs 4.6 and 4.7, the MeV ion data described below was from the "bottom" detector about 90^0 below the outer midplane, i.e. detector #6 in Fig. 2.

In all the cases ^{3}He was used in the minority heating mode with concentrations in the range of a few percent in D majority plasmas, with an ICRH frequency of 37 MHz and a resonant layer location within about ±5 cm of the plasma major radius of R_0=2.6 m at a toroidal magnetic field on axis of B=4.6-4.9 T. The plasma current range used here was 1.4-2.0 MA, and the maximum ICRF power was 5.2 MW. The ICRH-only cases also had deuterium pellet fueling just before the start of the ICRH. The cases with NBI+ICRH used the standard 100 keV parallel deuterium neutral beams in TFTR.

The approach of the present paper is to describe these new measurements and check whether the observed loss is consistent with the simplest possible loss mechanism (1) described in Sec. 2, namely the first-orbit loss of the D-^{3}He fusion-product alpha particle. Since the physics of the possible tail ion loss and/or ICRF-wave-induced

deconfinement is not well understood theoretically, and not yet documented experimentally, it is so far only possible to identify these other losses by eliminating the simplest possibility.

4.1 Time Dependences

The measured time dependence of the scintillator light emission for a typical discharge with both ICRH and NBI heating (#51731) is shown in Fig. 3(a), along with the 2.5 MeV neutron emission rate. For this discharge the plasma current was 1.4 MA, the major and minor radii were R_0=2.6 m and a=0.95 m, the NBI power was 19.5 MW during 3.0-4.0 sec, and the ICRH power was 3.1 MW during 3.3-3.8 sec. An identically prepared 1.4 MA discharge with NBI-only (#51734) is a shown in Fig. 3(b). For both of these shots the scintillator light from the MeV ions was monitored near the peak of the 2-D light emission pattern by a single PM tube, and the 2.5 MeV neutron signal was normalized to the scintillator detector signal for the NBI-only shot at 3.3 sec, with the same normalization carried over to the NBI+ICRH shot.

The main result illustrated by Fig. 3 is that the scintillator light signal due to MeV ions increases during ICRH even without a significant increase of the D-D neutron rate. Since the signal during NBI-only is normally due to the first-orbit loss of D-D fusion products[7], which is proportional to the neutron rate (except during strong MHD activity, which is not present during this discharge), then extra signal during ICRH is evidently *not* due to the normal loss D-D fusion products.

Also evident from Fig. 3(a) are fairly large and rapid time variations of the ICRH-induced MeV ion loss (e.g. a 50% change within about 30 msec), commonly seen when using the PM detection system. These variations do not appear to be caused by MHD or sawteeth in the plasma, but seem to be due to to changes in the ICRH coupling to the

minority ions (ICRH pickup can be excluded since electrically equivalent PM tubes not viewing the scintillator show only the usual small neutron/gamma background). This interesting aspect of the time variation will not be pursued further in the present paper, since most of the data was obtained using the relatively slow video camera detection system.

Two examples of the video camera measurement of the total ICRH-induced MeV ion loss vs time are shown in Fig. 4(a) and 4(b). Fig. 4(a) is for a 1.4 MA shot similar to that of Fig. 3(a), but with up to 5.2 MW of ICRF was applied during 19 MW of NBI (#54271). This figure also shows a very similar shot with NBI-only (#54272) plotted on the same scale. Evidently the MeV ion loss signal increases by about a factor of 2-3 during ICRH, even though the 2.5 MeV neutron emission vs time is almost identical with or without ICRH.

Fig. 4(b) shows a shot in which 4.6 MW of ICRH is applied *without* NBI to a 1.4 MA discharge previously fueled with deuterium pellet injection (#55540). The lost MeV ion signal level in this ICRH-only case is still rather high, i.e. about 0.3 times that observed for D-D fusion product loss in the 19 MW NBI-only phase of the discharge shown in Fig. 4(a). Notice that the neutron rate in this ICRH-only discharge is only $\approx 3 \times 10^{13}$ n/s, which is negligible compared to $\approx 10^{16}$ n/sec for the NBI-only case, as shown in Fig. 4(c).

Thus the application of ICRH heating to D-^{3}He plasmas produces a loss of MeV ions not normally seen during D-D NBI plasmas. This loss starts and stops just after the ICRH heating waveform, with a delay of at least 10's of msec at both ends. The loss can also be strongly varying with time during the RF pulse in an irregular way from shot-to shot, most likely due to variations in the ICRH coupling efficiency to the plasma and not to MHD activity, at least for shots like that in Fig. 3(a).

4.2 Pitch Angle and Gyroradius Distributions

Figs. 5(a) and (b) show a comparison between the 2-D scintillator light emission patterns for a typical ICRH-only (#55540) and a NBI-only discharge (#54274). These two patterns were obtained from digitized video images integrated over the duration of the respective heating pulses. The ICRH-only pattern comes from the same 1.4 MA, 4.6 MW shot shown in Fig. 4(b), and the NBI-only pattern comes from a 1.4 MA, 23 MW shot similar to that in Fig. 4(b).

The grid superimposed on the patterns in Fig. 5 represents the toroidal pitch angle (χ) vs gyroradius (ρ) coordinate system mapped onto the scintillator plane, as derived from a detector simulation identical to that described previously[7]. Note that these grid points represent only the *centroids* of the expected impact positions of particles with a given (χ,ρ), and that in particular the ρ distribution are significantly broadened by the finite detector resolution. The foil energy attenuation factor was taken to be 0.8 for both cases, as it was previously for the D-D fusion products and also should be for 3.7 MeV alpha particles[18].

The examples of Fig. 5 illustrate the general trend that the (χ,ρ) distributions for the ICRH-only case are at least qualitatively similar to those for the NBI-only case. This is consistent with the expectation that the MeV ion loss mechanism during D-^{3}He is simple first-orbit loss of the 3.7 MeV alpha particles, which should have (χ,ρ) distribution similar to the D-D fusion products.

The (χ,ρ) comparison between ICRH-only and NBI-only shots is examined in more detail in Figs. 6 and 7, which show the separate pitch angle and gyroradius distributions of the data of Figs. 5(a) and (b). The pitch angle distributions are averaged over the gyroradius range ρ=2-11 cm, and the gyroradius distributions are averaged over the pitch angle range $\chi=45^0$-90^0 (both corresponding to the grid region shown in Fig. 5).

Note that the neutron/gamma background has been subtracted in both cases using a portion of the scintillator not hit by fusion products (this background is negligible in the ICRH-only shots).

The measured pitch angle distributions for the NBI-only and ICRH-only cases shown in Fig. 6(a) are quite similar to each other, with peaks at χ=66^0 and 68^0, respectively, and FWHM of 14^0 and 15^0, respectively. Pitch distributions for all other ICRH-only and ICRH+NBI discharges are quite similar to the cases shown. Since the D-D pitch distributions have been consistent with the first-orbit loss model[7], this implies that the pitch distribution with ICRH-only is roughly consistent with the first-orbit loss of 3.7 MeV alphas.

To check this, two calculated pitch angle distributions for first-orbit loss of 3.7 MeV alphas are also shown in Fig. 6(b). These curves were obtained from the standard ORBIT code calculation[19], which takes into account the magnetic structure derived from the SNAP analysis code for this shot, and the known detector and optical broadening effects as in Ref. [7]. For one curve the alpha source profile shape was taken to be a Gaussian with FWHM/a=0.5, as is typical for D-D source profile (see Sec. 4.5), while for the other curve a very narrow profile was chosen with FWHM/a=0.2 (used in Sec. 4.6).

The calculated pitch angle curve with FWHM/a=0.5 agrees quite well with the measured ICRH-only data, implying that this data is consistent with first-orbit loss of 3.7 MeV alphas. Note that the expected peak pitch angle for first-orbit loss is rather insensitive to the assumed alpha energy, varying by only $\pm 3^0$ over the alpha energy range 3.7±2 MeV (the expected D-D fusion product location is also only about 1^0 smaller than that for the 3.7 MeV alpha peak). However, the escaping 15 MeV protons has a significantly different pitch distribution, as discussed in Sec. 4.3.

Fig. 7 shows the measured gyroradius distributions for these same

two NBI-only and ICRH-only shots. Although the two gyroradius distributions are qualitatively similar to each other, they have a different peak location and shape, with the peak at $\rho \approx 5$ cm for the NBI-only case and at $\rho \approx 6.8$ cm for the ICRH-only case. The ICRH-only case also has a particularly high signal at large gyroradii $\rho > 7$ cm, independent of the ICRH power level. The expected gyroradius for first-orbit loss of 3.7 MeV alphas at this detector is $\rho = 5.4$ cm, i.e. only about 10% larger than that for D-D fusion products ($\rho = 4.9$ cm).

Recall that the ρ coordinate of Fig. 7 measures only the *centroids* of the impact zones for ions of a given incident energy (converted to a 90^0 gyroradius ρ), and that most of the spread in the data along this coordinate is due to the finite resolution of the detector apertures. Thus these distributions need to be compared with those calculated using the detector analysis code, such as the one for D-D fusion products also shown in Fig. 7. After including the detector geometric and optical broadening effects, the expected gyroradius distribution for D-D fusion products is similar to the NBI-only data, as shown in Fig. 7. However, there is a discrepancy between the measured and expected distributions for 3.7 MeV alphas, as discussed in Sec. 4.3, which is could due to the presence of 15 MeV protons or to the large Doppler broadening of the alphas. Note that the measured D-D distribution in Fig. 7 may also affected by the Doppler shift due to beam-target reactions, not included in the modeling.

In summary, the pitch angle distribution of the MeV ions lost during ICRH minority heating agrees with that expected for first-orbit loss of the 3.7 MeV alpha particle. However, the gyroradius distribution during ICRH-only shows a peak ρ about 25% higher than expected, and a broad signal at higher $\rho > 7$ cm. This anomaly is examined further in the next section.

4.3 Effects of 15 MeV Protons and Alpha Doppler Broadening

The expected first-orbit loss rate for 15 MeV protons is actually larger than that for the 3.7 MeV alphas, since the orbits of the 15 MeV protons can escape to the detector from nearer the plasma center. For example, Fig. 8(a) shows the 3.7 MeV alpha and 15 MeV proton loss orbits which pass nearest to the plasma center for a 1.4 MA ICRH-only discharge (#55540), and Fig. 8(b) shows these "fattest banana" orbits for a 2.0 MA discharge (#54316).

At both these currents the 15 MeV proton orbits can be lost from the plasma center to the bottom detector, while the 3.7 MeV alpha orbits are lost only from about $r/a>0.3$. Therefore the calculated first-orbit loss for 15 MeV protons is somewhere between 2-5 times larger that for 3.7 MeV alphas (for the 1.4 MA case), assuming D-^{3}He source profiles shapes with FWHM/a=0.5 and FWHM/a=0.3, respectively.

However, the present detector was not designed to measure 15 MeV protons, which tend to pass right through the 10μ thick ZnS scintillator without interaction. At the expected angle of incidence of $\approx 15^0$ to the scintillator surface a 15 MeV proton should deposit only about $\approx$0.5 MeV in the scintillator[18,20], whereas a 3 MeV proton should deposit about 1.0-1.5 MeV[18], and a 3.7 MeV alphas should deposit its entire energy in the scintillator. However, the ZnS scintillator light output for 3.5 MeV alphas is about 6 times that for 3 MeV protons, as measured in a D-D test stand [18] (the higher light output/energy deposited is probably due to the larger charge of the alpha). Therefore the expected ratio of the light output for a 15 MeV proton relative to a 3.7 MeV alpha is only $\approx$0.1-0.05. Note that since this ratio has not yet been measured for these scintillators, this is only an approximate estimate.

We now reexamine the pitch and gyroradius distributions of Sec. 4.2 in order to look for signs of 15 MeV proton first-orbit loss. Fig. 9 shows a comparison between the expected gyroradius distribution for 15

MeV protons and that for 3.7 MeV alphas (where both distributions have been normalized to the peak height of the data from the previous ICRH-only discharge). An equal weighting of these two distributions could reproduce the measured peak location at $\rho \approx 6.8$ cm, and could roughly explain the unexpectedly large signal at high $\rho > 7$ cm. However, this would imply an escaping proton flux of about 10-20 times the escaping alpha flux, in contrast to the expected proton first-orbit loss rate of 2-5 times the alpha first-orbit loss rate estimated from the orbit code for the source profile FWHM/a=0.3-0.5.

Fig. 10 shows the expected pitch angle distribution for the first-orbit loss of 15 MeV protons, along with the calculated first-orbit loss distribution for 3.7 MeV alphas assuming a source profile shape FWHM/a=0.3. The 15 MeV protons signal should peak at a pitch angle of $\chi \approx 78^0$, which is significantly higher than the expected peak at 67^0 for 3.7 MeV alphas and the measured peak at 68^0. Therefore the measured pitch angle distribution does *not* seem to allow the presence of a large 15 MeV first-orbit loss component comparable to the 3.7 MeV alpha component (as suggested by the gyroradius distribution), even assuming a narrower source profile, since the peak of the resulting pitch distribution would be at a larger angle than observed.

This conclusion is further supported by Fig. 11, which shows a comparison between the measured pitch angle distributions for the ICRH-only case for two different gyroradii ranges ρ=3-5 cm and ρ=9-11 cm. The measured pitch distribution at large gyroradii shows only a slight feature near 78^0 which could be attributed to 15 MeV protons, corresponding to an additional signal <about 0.1 times the 3.7 MeV alpha signal (i.e. roughly consistent with the expected 15 MeV proton flux from the first-orbit calculations). Thus the first-orbit loss of 15 MeV protons can not explain the higher than expected ρ distributions in ICRH-only cases.

However, a different effect which *can* in principle explain both the

gyroradius and pitch distributions in ICRH-only shots is the unusually large Doppler broadening of the 3.7 MeV alphas expected due to the high energy of the ^{3}He ion tail distribution[21]. For example, a ^{3}He ion with a plausible energy of 0.4 MeV fusing with a stationary D will create a fusion product alpha of energy $\approx$5.6 MeV in the lab frame, which has a gyroradius (at a 90^0 pitch angle) very close to the observed peak of the measured distribution at $\rho\approx$6.8 cm. As mentioned previously, the expected pitch angle distribution for first-orbit loss is quite insensitive to the alpha birth energy, so that even 5.6 MeV alphas should be lost near the measured ICRH-only pitch angle of Fig. 10.

The conclusion of this section is that because of their relatively low light output (per ion) the 15 MeV protons do not contribute significantly to the observed signals. However, the anomaly in the observed gyroradius distribution can probably be explained by the Doppler-broadened energy spectrum of the 3.7 MeV alphas, as described in more detail in Sec. 5.2.

4.4 Plasma Current Dependence

If the lost MeV ion signals observed during ICRH minority heating were due to first-orbit loss of the D-^{3}He alpha particles, then these signals should have the same dependence on plasma current as seen previously for D-D fusion products[7]. The two main changes seen with increasing current were a decrease in lost ion flux (per neutron) and a shift in the pitch angle distribution to smaller χ. Unfortunately, the former can not be checked here, since there was no independent monitor of the D-^{3}He reaction rate to use in normalizing the lost ion flux.

The measured MeV ion loss vs time for a typical 2 MA, 3.7 MW ICRF+23 MW NBI discharge (#54316) is shown in Fig. 12(a) (still with B_0=4.9 T and R_0=2.6 m). This curve shows the time dependence of the

total loss to the bottom detector, integrated over pitch and gyroradius in the video camera mode as for Fig. 4(a). The MeV ion flux again increases during ICRH without a corresponding increase in the D-D reaction rate, e.g. by a factor of 2 during the ICRH time from 3.5-3.9 sec in this shot. A 2 MA shot with 4 MW of ICRH-only (#55451) behaves at least qualitatively similarly, as shown in Fig. 12(b).

Fig. 13 shows the pitch angle distribution of the signal during ICRH for the two shots in Fig. 12, along with a NBI-only D-D fusion product distribution for a similar 2.0 MA discharge (#54308). All of these distributions show a peak near $\chi \approx 62^0$, instead of $\chi \approx 68^0$ for the 1.4 MA case (Fig. 6). This shift of the peak toward lower pitch angle agrees fairly well with the expected first-orbit distribution for 3.7 MeV alphas in the ICRH+NBI shot, also shown in Fig. 13 (calculated assuming a source profile with FWHM/a=0.5). However, the pitch distribution at 2.0 MA is somewhat broader than expected from the model shown, suggesting a somewhat broader than normal source profile shape for this case.

The gyroradius distribution for the 2.0 MA ICRH-only shot is similar to that for the 1.4 MA ICRH-only shot described previously, with a peak gyroradius of ≈7 cm, i.e. significantly larger than that for a 2.0 MA NBI-only shot (≈5 cm). The distribution for the ICRH+NBI shot peaks between 5 cm and 6 cm, as expected for first-orbit loss of a mixture of D-D ions D-^{3}He alphas.

4.5 Inference of the Radial Alpha Source Profile

A detector at the vessel bottom "see" first-orbit loss from different radial zones, depending only on the pitch angle at the detector at a given plasma current and current distribution[7]. Therefore the radial birth profile of a fusion product source can in principle be

inferred from the pitch angle distribution of the loss. Note that this inference requires the assumption that the observed MeV ion loss is only due to first-orbit loss.

A fairly good agreement has already been shown in Fig. 6(b) between the measured pitch angle distribution for a 1.4 MA ICRH-only shot and a pitch angle distribution calculated using a Gaussian source profile of FWHM/a=0.5 for 3.7 MeV alphas. This agreement was considerably better than that for an assumed FWHM/a=0.2, for which the calculated distribution was much too narrow to fit the data. The implied distribution with FWHM/a≈0.5 is typical of NBI neutron source profiles at 1.4 MA[22].

Another way to infer the D-^{3}He source profile is to examine ICRH+NBI shots in which the pitch angle distribution can be compared within the *same shot* between the ICRF+NBI an NBI-only time periods, as shown for example in Fig. 14. For both the 1.4 MA case in Fig. 14(a) and the 2.0 MA case in Fig. 14(b) the pitch distributions are essentially the same during ICRH+NBI and NBI-only, implying that the D-^{3}He alpha source profile is nearly the same as the D-D source profile. The D-D reaction rate profile inferred from multichannel neutron collimator measurements for these particular shots had FWHM/a=0.6-0.7 for 1.4 MA (with or without ICRH) and FWHM/a=0.4-0.5 for 2.0 MA (with or without ICRH)[23].

Therefore the D-^{3}He reaction rate profiles inferred through the pitch angle distribution from the bottom detector (assuming that the observed loss is due to first-orbit loss) are similar to those for the D-D reaction rate during NBI, i.e. FWHM/a=0.55±.15. The calculated D-^{3}He source profile is quite close to this, as discussed in Sec. 5.1.

4.6 Results from the 45^0 Poloidal Detector

Since detectors at different poloidal locations sample first-orbit loss from different regions of the source profile, another way to infer the D-^{3}He radial source profile from the assumption of first-orbit loss uses the relative signals between MeV ion loss detectors at two different poloidal locations. For example, Fig. 15(a) shows that for a 1.4 MA case the "fattest" 3.7 MeV alpha banana orbit to a detector 45^0 poloidally below the midplane passes nearly through the plasma center, while the fattest 3.7 MeV alpha banana orbit to the detector 90^0 below the midplane samples regions only at somewhat larger radii. Fig. 15(b) shows a similar effect at 2.0 MA.

Thus a 45^0 detector should have a relatively larger response for a very peaked source profile. Fig. 16 shows the calculated ratio of the detection efficiency for the 45^0 detector to that for the 90^0 detector as a function of the assumed Gaussian source profile. This particular plot is for 3.7 MeV alpha loss at 1.4 MA, where the detection efficiency was summed over all orbits in the range 45^0-90^0 in both cases. This calculation shows that the ratio of the first-orbit loss at 45^0, normalized to that at 90^0, should decrease with increased source profile width, due to the differences in orbit geometry like that shown in Fig. 15.

Two examples of the total lost MeV ion signal vs time for the 45^0 detector are shown in Fig. 17, with 17(a) for a 1.4 MA shot (#54271) and 17(b) for a 2.0 MA shot (#54316). Both these shots were used previously to illustrate the 90^0 signals for ICRH+NBI discharges. During ICRH the MeV ion loss signal at 45^0 increases by over x10 above the NBI-only level, which is much greater than the analogous increase of x2-3 above the NBI-only level seen during ICRH in the 90^0 detector. Therefore the 45^0 detector sees relatively more loss during ICRH than does the 90^0 detector, possibly consistent with the supposition that the D-^{3}He source profile is more peaked than the D-D source profile.

A database of the measured ratio of the $45^0/90^0$ MeV ions signals vs ICRH power is shown in Fig. 18, based on data like that of Fig. 17 (with all shots at 1.4 MA). In this database there are some shots with NBI-only (15-23 MW), some with ICRH-only (1.0-4.5 MW) and some with ICRF+NBI (with 1.0-4.5 MW ICRH +15-23 MW NBI). The signals are taken using the video camera, and averaged over the pixel/line ranges near the peak of light pattern for both detectors (i.e. pixels 14-20, lines 17-23 for the 90^0 detector and pixels 26-32 and lines 9-15 for the 45^0 detector). For all shots the signals are averaged over most of the ICRH pulse (e.g. 3.5-3.8 sec NBI+ICRH), and the measured $45^0/90^0$ signal ratio is corrected for the measured $45^0/90^0$ instrumental sensitivity ratio of 0.64 [18].

The first result of this analysis is that for NBI-only the $45^0/90^0$ signal ratio is $\approx$0.3-0.6. This is close to the calculated ratio of 0.4 for the total first-orbit loss of D-D fusion products at $45^0/90^0$, assuming a source profile with FWHM/a=0.5 for the NBI-only cases. The scatter among these points is presumably due to fusion product source and plasma current profile variations.

However, Fig. 18 also shows that the measured $45^0/90^0$ signal ratio shows a systematic *increase* with increasing ICRH power, particularly with simultaneous NBI, such that the $45^0/90^0$ ratio goes up by about a factor of three at ICRH powers of >4 MW. Therefore since the NBI-only cases had a measured neutron source profile in the range FWHM/a$\approx$0.5, then according to Fig. 16 in order to explain this result in terms of first-orbit loss of alphas the ICRH cases must have had a much narrower source profile, with a FWHM/a$\approx$0.15-0.20. Thus at first sight this method of inferring the radial source profile gives a different result than that from the pitch angle distribution from the 90^0 detector in Sec. 4.5.

There are several possible resolutions to this apparent inconsistency. The simplest is that the large Doppler shifts due to the

^{3}He tail energy distribution (see Sec. 4.3) might invalidate these orbit code results. However, since this effect would primarily change the energy spectrum of the loss and not their radial profile or isotropy, it is unlikely to effect the calculated poloidal distribution (in fact, a larger alpha birth energy would imply a smaller $45^0/90^0$ first orbit loss ratio). Another relatively simple possibility is that the source profile driven by the ^{3}He ions is spatially asymmetric, as suggested by the orbits of typical ^{3}He tail ions in Fig. 15(c), thus possibly allowing preferential first-orbit loss to the 45^0 detector. However, the modeling of this possibility done so far can not explain such a large change in the $45^0/90^0$ loss ratio, as discussed Sec. 5.3.

A third "classical" possibility is that part of the signal at 45^0 is *not* due to first-orbit loss, but rather to stochastic toroidal field-induced ripple loss[24] which has been seen to dominate the observed loss at another detector $\approx 20^0$ below the outer midplane (not used for the present experiments). However, calculations for 1.4 MA and 1.8 MA discharges similar to the ones of Fig. 17 show a negligible ripple-induced enhancement of the expected loss at 45^0[18].

The other general possibility is that the losses to the detector at 45^0 are not due to either first-orbit loss or TF ripple loss, but rather to the ICRH-minority tail itself or to ICRH-deconfined D-D fusion products, as discussed in Sec. 2. One way to test these various possibilities is to examine the 2-D scintillator patterns for the 45^0 detector. Figure 19 shows three examples of the 2-D patterns (χ,ρ) patterns for the 1.4 MA discharge types used in the database of Fig. 18: 19(a) had 16 MW NBI-only (#53220) with a $45^0/90^0$ ratio of 0.65, shot (b) had 4.4 MW ICRH-only (#55540) with a $45^0/90^0$ ratio of 1.2, and shot (c) had 4.6 MW ICRH+19 MW ICRF with a $45^0/90^0$ ratio of 1.25 (#54271). The last shot (d) was at 1.8 MA, and had 4.2 MW ICRH+19 MW with a very large $45^0/90^0$ ratio of 2.8 (#54282).

The NBI-only pattern at 45^0 shown in Fig. 19(a) has a peak near

$\chi \approx 56^0$ and $\rho \approx 7.3$ cm, which is close to the expected D-D fusion product first-orbit loss peaks at $\chi \approx 53^0$ and $\rho \approx 7$ cm (due to the smaller toroidal field at this detector). The ICRH-only pattern at 45^0 shown in Fig. 19(b) had a pitch angle peak at 57^0 and a slightly higher ρ peak at 8.8 cm (similar to the ρ distribution in the 90^0 detector). Therefore both the NBI-only and the ICRH-only losses at 45^0 seem to be consistent with first-orbit loss, albeit at an unexpectedly large rate for the ICRH-only case.

However, there was often a fairly clear distortion in the shape of the 2-D light pattern with ICRH+NBI, e.g. for the shot of Fig. 19(c) which had a high $45^0/90^0$ ratio. The shape in Fig. 19(c) extends to significantly lower ρ and higher χ than for the ICRH-only case, even though the signal during ICRH seems to be dominated by the ICRH-induced losses, as shown in Fig. 17(a).

The separate ρ and χ distributions for these three 1.4 MA cases are shown in Fig. 20. The ρ distribution for the ICRH-only case has a larger gyroradius than that for the NBI-only case, which was previously explained for the similar 90^0 data by a Doppler-shifted first-orbit loss of the D-^{3}He alphas, while the ICRH+NBI case has a lower gyroradius distribution than expected for the first-orbit loss of D-^{3}He alphas (in fact, one surprisingly similar to the NBI-only case). Interestingly, the χ distribution of the ICRH+NBI case peaks at a higher χ than either the ICRH-only or NBI-only, again suggesting some non-first-orbit loss process. These (χ,ρ) distortions seen at 1.4 MA are qualitatively similar at 1.8 MA (Fig. 19(d)), and also in the 2.0 MA data (not shown); in particular, the ρ distribution extends to even lower gyroradii in those cases.

Since the low-ρ, high-χ shape distortions like that shown in Fig. 19(c-d) appear to occur only with NBI+ICRH and not with ICRH-only, they appear at first to be due to deconfined D-D or D-^{3}He fusion products, rather than loss of the ICRH tail itself (which should also be present

with ICRH-only). The most likely wave-deconfined fusion product is the 1 MeV triton, which sees a second-harmonic ICRH wave in these experiments. However, the effect of direct ICRH tail loss can not be excluded, since the ICRH tail most likely has a higher energy in the ICRH+NBI case (see Sec 4.7).

Further information can be obtained from the relative time dependences of the ICRH-induced loss at 45^0 and 90^0. For ICRH-only these two signals are quite similar vs time, consistent with first-orbit alpha loss. However, they are often (but not always) somewhat dissimilar with ICRH+NBI, as can be seen by comparing Fig. 4(a) to 17(a), and Fig. 12(a) and 17(b). This difference in time dependence is again most likely due to an additional non-first-orbit MeV ion loss at 45^0 with ICRH+NBI.

In summary, the ICRH-induced MeV ion loss observed at 45^0 poloidally is unexpectedly larger than the analogous NBI-only loss by a factor of up to x3-4. This extra loss at 45^0 might be explained in part by various classical effects, e.g. due to an asymmetric source profile. However, for some ICRH+NBI discharges there is often a coincident shift in the (χ,ρ) spectrum to lower ρ and higher χ which can not be explained by first-orbit loss. This latter effect is possibly consistent with the ICRF-wave-induced deconfinement of some of the previously-confined D-D (or D-^{3}He) fusion products, although the loss of ^{3}He tail ions can not be ruled out. Further experiments and modeling are needed to clarify the relative contributions of various possible non-first-orbit loss mechanisms at 45^0.

4.7 Variation of MeV Ion Loss with ICRH Power

Several scans of ICRH power in the ^{3}He minority mode were done during the 1990 TFTR run. Fig. 21 shows the results for a scan with

ICRH-only power at 1.4 MA. The total MeV ion loss signals for both the 90^0 and 45^0 detectors increased proportionally to $\approx$(ICRH power)^3 in the power range $\approx$1.0-4.5 MW. The (χ,ρ) location of the peak signal was approximately constant over this power range, consistent with the assumption of a simple first-orbit loss process. This MeV ion loss is most likely due to alphas from the D-^{3}He reaction rate, although the $45^0/90^0$ signal ratio is not quite understood (Sec 4.6).

Fig. 22 shows the relative ICRH-induced MeV ion loss signal at 90^0 vs ICRH power during 1.4 MA and 1.6 MA ICRH+NBI power scans, as monitored by a PM tube as in Fig. 3(a). This ICRH-induced MeV ion loss level was derived by subtracting from the net signal during ICRH+NBI the expected contribution from the D-D fusion products, as inferred from NBI-only loss signal earlier in the same shot. The relative ICRH-induced MeV ion loss increases with ICRH power similarly to the ICRH-only case in Fig. 21. The lost ion flux at 1.4 MA tended to be slightly larger than that at 1.6 MA, as at least qualitatively as expected for the improved first-orbit confinement at the higher current (although the D-^{3}He reaction rate per unit ICRH power may also be changing with current).

The variation of the ICRH-induced MeV loss signals vs ICRH power with and without $\approx$15-20 MW of NBI is shown in Fig. 23, this time for data taken with the video camera for the 90^0 detector at 1.4 MA. The ICRH-induced MeV ion loss with ICRH+NBI is again derived by subtracting out the expected contribution from D-D fusion products (as for Fig. 21). For a given level of applied ICRH power, the ICRH-induced loss to the bottom detector during NBI is about 5-10 times larger than that obtained during an ICRH-only discharge.

The ICRH-induced MeV ion loss at 90^0 described by Figs. 22 and 23 are again most likely due to simple first-orbit alpha loss from the D-^{3}He reaction, since none of their 2-D patterns (χ,ρ) patterns shows any anomalous distortion in the 90^0 detector, even for the same shot with a large 45^0 distortion, i.e. Fig. 19(c). Note that the same type of high-χ,

low-ρ distortion in 45^0 detectors was also observed for many the shots of Fig. 21, and that the signal at 45^0 is often much larger than expected due to first-orbit alpha loss.

Tentatively assuming that the 90^0 detector is measuring first orbit alpha loss (and that the D-^{3}He source profiles are similar with and without NBI), Fig. 22 implies that the D-^{3}He reaction rate is larger for a given ICRH power level with simultaneous 15-20 MW NBI. This is plausible since the central electron temperature is higher with NBI, implying less ion drag and therefore a higher ^{3}He tail temperature and reaction rate. For example, in two typical cases (#55540 vs #54271) without NBI $T_e(0)\approx 5.5$ keV at $n_e(0)=5\times10^{13}$ cm^{-3}, and with NBI $T_e(0)\approx 8$ keV at $n_e(0)=4\times10^{13}$ cm^{-3}; thus the high energy ion drag is lower with NBI by a factor of ≈ 2. Uncertainty in the relative ^{3}He concentration between these two cases makes a more precise comparison difficult.

The absolute magnitude of the D-^{3}He reaction rate can also be estimated based on the measured 90^0 ICRH-induced MeV ion loss, assuming again that the loss process is first-orbit loss of 3.7 MeV alphas. This was done by assuming that the source profile was the same for the D-D and D-^{3}He reactions, so that at a given current the loss rate of alphas normalized to the loss rate of D-D fusion products (during NBI-only) is proportional to the source rate of alphas normalized the (known) source rate of D-D fusion products. Note that the measured light output for a 3.7 MeV alpha particle is ≈ 3 times that of the combined 1 MeV triton and 3 MeV proton pair[18], and that one 2.5 MeV neutron is created for each (T+P) pair. Therefore when the D-^{3}He alpha component of the MeV ion loss signal is equal to three times the D-D (T+P) component, then the inferred global D-^{3}He reaction rate is equal to the measured global D-D reaction rate.

The vertical axes of Figs. 21 and 22 have been labelled in terms of this inferred D-^{3}He reaction rate, in units of 10^{15} reactions/sec. The

inferred D-^{3}He reaction rate during ≈4 MW of ^{3}He minority ICRH+NBI heating is ≈0.5-1.0x10^{16} reactions/sec (this can also be seen directly from the ICRH+NBI signal vs time in Fig. 4). Thus the D-^{3}He fusion power is ≈20 kW with ≈4 MW ICRH, implying an *incremental* dQ/dP(ICRH)≈0.05. For the ICRH-only cases the inferred reaction rate at ≈4 MW is ≈1x10^{15} reactions/sec, implying an actual Q≈.001, which is comparable to that for D-D reactions with ≈30 MW NBI [25], and considerably smaller than that for D-^{3}He minority heating in JET [26].

Note that there are several large uncertainties in this estimate of the D-^{3}He reaction rate from the lost MeV ion flux, even if it is assumed that all the loss at 90^0 is due to classical first-orbit loss. First, if the actual alpha source profile is different from the D-D source profile, then the inferred D-^{3}He reaction rate varies with the assumed source profile; for example, a symmetrical source with a variation of FWHM/a=0.5±0.2 results in a first-orbit loss variation of ±50%, and an asymmetrical source would cause a variation depending on its average R (see Sec 5.3). Second, if the escaping alpha energy is Doppler actually upshifted by up to ≈6-7 MeV, the light produced per ion is increased by about a factor of two from that assumed above, thus potentially reducing this estimate of the reaction rate by about x2. This overestimation effect is further increased by the ≈50% higher first-orbit rate expected for such higher energy alphas.

The conclusion of this section is that the measured ICRH-induced MeV ion loss at 90^0 increases monotonically with ICRH power, as expected for first-orbit loss of D-^{3}He fusion product loss. With ICRH-only the loss signals increase proportionally to (ICRH power)^3, similar to the variation (ICRH-power)$^{2.0-3.5}$ observed on PLT[14] and the (ICRH-power)$^{5/3}$ seen on JET[26]. If the observed loss is first-orbit loss of 3.7 MeV alphas, the inferred reaction rate varies in the range from ≈0.1-1x10^{16} reactions/sec, within a systematic uncertainty of at least x3.

5. Modeling of D-^{3}He Alpha Particles

This section first describes computer modeling results for the D-^{3}He reaction rate and its radial profile for a typical 2 MA TFTR case. The predicted rate and radial profile agree fairly well with the conclusions from the analysis of the lost alpha signals for the 90^0 detector (Sec. 4.5 and 4.7). The other two parts of this section describe attempts to model the anomalies observed in the gyroradius distribution (Sec. 4.2) and the $45^0/90^0$ loss ratio (Sec. 4.6).

5.1 D-^{3}He Reaction Rate Profile

In the usual ICRF heating scenario, the resonant minority ions become very energetic. In the case of ^{3}He-minority heating this will cause a large increase in the D-^{3}He fusion reaction rate. Modeling of the minority tail distribution has generally been done with the Stix theory [27], and good agreement between such modeling and measurements of the tail energy and D-^{3}He gamma emission rate has been established at JET [28,29].

For TFTR the D-^{3}He reaction rate is calculated using FPP/SPRUCE, a bounce-averaged quasilinear and Fokker-Planck code for comprehensive simulation of NBI and ICRH heating of tokamak plasmas. SPRUCE [29,30] solves a full wave equation for the ICRF fast wave propagation and damping, including the effects of fundamental and second harmonic ion damping, electron damping, and mode conversion. FPP [31,32] solves the bounce-averaged Fokker-Planck equation (including a bounce-averaged quasilinear operator which uses the wave fields calculated by SPRUCE) to find the fast ion distribution function as a function of energy, magnetic moment, minor radius, and time.

Fig. 24 shows the predicted ^{3}He reaction rate profile and its tail

"temperature" (defined as 2/3 of the average energy) for a 2 MA ICRH+NBI discharge similar to that shown in Fig. 12 (#54316), but with a somewhat larger 5.2 MW of ICRH power (i.e. #54320). The calculated D-^{3}He source profile has a FWHM/a$\approx$0.5, and a total source rate of $\approx 1.6 \times 10^{16}$ D-^{3}He reactions/sec (equivalent to 45 kW of D-^{3}He fusion power). This rate is similar to the measured peak D-D neutron production for #54320 of 1.7×10^{16} neutrons/second, which is dominated by beam-target reactions from the 23 MW of deuterium beam injection. The average energy of the ^{3}He near the plasma center is $\approx$0.8 MeV, which incidentally is about half the average energy of the slowing down distribution for fusion product alphas from either D-^{3}He or D-T.

The predicted D-^{3}He rate is somewhat sensitive to the assumed ^{3}He concentration (which was based on the measured density rise during the ^{3}He gas puff but which assumes 100% recycling and ignores any ^{3}He residual from previous shots). Doubling the ^{3}He concentration from 1.25% to 2.5% causes the predicted D-^{3}He rate to increase only 50%, as the increase in the number of ^{3}He ions is partially offset by the drop in their average energy.

Analysis of the MeV ion data for the 90^0 detector from the closest available shot, with only 3.7 MW ICRH (#54316, in Fig. 12(a)), gives a global D-^{3}He reaction rate of $\approx 0.9 \times 10^{16}$ alphas/sec, as inferred from the ratio of the escaping alpha flux during ICRH to the escaping D-D fusion product flux during NBI (see Sec. 4.7). If the D-^{3}He reaction rate increases $\approx$linearly with ICRH power as it does for the 1.4 MA ICRH+NBI cases of Fig. 23, then the inferred reaction rate for 5.2 MW ICRH power would be $\approx 1.3 \times 10^{16}$ reactions/sec, i.e. only about 20% below the prediction of the modeling. The data on the pitch angle dependence of the escaping MeV ions (Fig. 13) is also roughly consistent with the model-inferred source profile of FWHM/a=0.5, although there is considerable uncertainty here since the data contains contributions from both alphas and D-D fusion products for this case.

In summary, the available modeling predicts a D-^{3}He reaction rate and radial source profile roughly comparable to that inferred from the escaping MeV ion data at 90^0. The primary uncertainty lies in the unmeasured concentration of ^{3}He ions near the plasma center, which can influence the tail temperature and resulting reaction rate.

5.2 Doppler Shifted Gyroradius Distributions

As noted in Sec. 4.2, the measured gyroradius distribution of lost MeV ions during ICRH-only discharges shows a peak at a higher ρ than expected from simple first-orbit loss of 3.7 MeV alphas. The most plausible explanation was that the alpha birth energy was significantly changed by the Doppler shift expected from the high energy ^{3}He tail. This Doppler shift broadens the birth energy distribution symmetrically, but the scintillator responds more to higher energy alphas.

Fig. 25 shows the previous data for the gyroradius disiribution of an ICRH-only shot (as in Fig. 7) along with model curves for assumed alpha energies from 1.7 MeV to 6.7 MeV. Each curve includes the appropriate foil energy attenuation factor, the relative scintillator response, and the optical and geometrical broadening. Evidently the observed distribution is fairly well fit by a single energy component between 5.7 and 6.7 MeV, although the contribution of lower energy components can not be ruled out due to their relatively small detector response (although note that the peak location can be changed considerably by a relatively small low energy component).

As mentioned in Sec 4.3, the expected Doppler shift ΔE of the alpha energy spectrum due to the ^{3}He tail ion energy is quite large, being at most (for colinear ^{3}He and alpha ions) $\Delta E \approx (1\ \text{MeV})(T_{^3He}/200\ \text{keV})^{1/2}$. Thus for the calculated tail temperatures of $T_{^3He} \approx 0.4\text{-}0.8$ MeV (Fig. 24),

the expected alpha energy for ions perpendicular to B (the direction of the ^{3}He ions) is ≈5-6 MeV, roughly consistent with the fit of Fig. 25. Note that the higher energy ions would also have a larger first-orbit loss to the bottom detector (e.g. by 40% for 6 MeV alphas), further reducing the expected effect of the down-shifted alphas in the spectrum. Note also that reactions between the ^{3}He tail and the NBI fast ions would also contribute to the Doppler width, but only at a rate proportional to the beam ion fraction (<10%).

Thus the expected Doppler spread in alpha energy is a plausible cause for the observed ρ distributions, but possible non-first-orbit loss contributions can not yet be excluded. In order to do this, further efforts are needed in the calculation of the Doppler-broadened spectrum, such as in Refs. [21] and [33], including the radial variability of the calculated ICRH tail energy (Sec. 5.1) and anisotropic source distributions within the first-orbit loss code. There are also some remaining instrumental uncertainties to be clarified, for example, in the detector's gyroradius resolution, particularly near the large-ρ edge of the scintillator plane, and in the detector response function vs alpha energy.

5.3. Asymmetric Source Profiles

The anomalously large loss of MeV ions at 45^0 poloidally has been described in Sec. 4.6 and summarized by Fig. 18, which shows that the ratio of loss at $45^0/90^0$ is about twice as large for ICRH-only discharges as for NBI-only discharges (with considerable scatter about this ratio). One possible explanation could be an asymmetric source profile for the D-^{3}He reaction rate, which could bias the first-orbit loss process toward 45^0.

This mechanism was illustrated by Fig. 15(a), which shows the

alpha-like "fattest banana" orbits for 45^0 and 90^0 for a 1.4 MA case. If the D-^{3}He source happened to be concentrated along the 45^0 loss orbit, and not so concentrated along the 90^0 orbit, then the $45^0/90^0$ loss ratio obviously could increase substantially. At first sight such an extremely asymmetric source profile seems highly unlikely. However, it is plausible that the D-^{3}He source profile is localized where the high energy ^{3}He tail ions are localized, which is with their banana tips at the resonant layer ($R \approx 2.63$ m), as shown by a typical 0.5 MeV ^{3}He orbits in Fig. 15. This would cause the D-^{3}He source to be localized somewhat outside in major radius from the RF resonance layer (note that this effect was poloidally averaged in the simulation results of Sec. 5.1).

A modeling study of this effect was made by assuming that the D-^{3}He source was confined to a vertical band at a variable R, with a separately variable vertical and horizontal Gaussian FWHM/a. Calculated $45^0/90^0$ first-orbit loss ratios for the 1.4 MA case are shown in Fig. 26. The vertical source profile was chosen to be either FWHM/a=0.5 or 1.0, and the horizontal FWHM/a was fixed at 0.1 m for these cases.

Fig. 26 shows that the calculated $45^0/90^0$ first-orbit loss ratio can vary from the nominal 0.4 (for a normally symmetric source profile with FWHM/a=0.5) over the range 0.2-0.6 for the R range examined. The largest ratio of $\approx$0.6 occurred for a profile centered at $R \approx 2.9$ m with a vertical FWHM/a=0.5. This profile choice had a 90^0 pitch angle distribution reasonably close to (but somewhat narrower than) the one measured for the ICRH-only case shown in Fig. 6. Choosing a narrower vertical profile increases this ratio, but causes an increasingly poor fit to the 90^0 pitch angle distribution (since the source would become similar to a very narrow symmetric one, as for Fig. 16). Choosing a higher alpha energy (as suggested in Sec. 5.2) would only result in a lower $45^0/90^0$ ratio, since as the ion energy increases the first-orbit loss becomes more nearly vertically downward.

Note that vertically asymmetrical source profiles such as those used for Fig. 26 do not tend to significantly change the expected location in the peak of the pitch angle distribution in the 90^0 detector, since the fattest banana orbit has it closest approach to the plasma center near R=300 cm, so even for symmetrical profiles the source near 300 cm dominates the distribution. However, a very narrow asymmetrical source at R>300 cm could be distinguished by its shifted and peaked pitch angle distribution, which was not observed in the data.

The tentative conclusion from this modeling is that only a relatively small part of the increased $45^0/90^0$ loss ratio with ICRH can be easily explained by a plausible vertical source asymmetry. Since the the other possible "classical" explanations are also unlikely (see Sec. 4.6), this implies that this asymmetry is primarily due to some non-first orbit loss process. For example, during H-minority heating direct MeV ion tail loss of $\approx$1 MeV protons is very clearly seen at 45^0 and not at all at 90^0[9].

6. Summary and Conclusions

This paper described measurements and interpretations of the loss of MeV ions during ^{3}He ICRH minority heating in TFTR. Three potential loss mechanisms were possible: 1) first-orbit loss of fusion-product alphas created by D-^{3}He fusion reactions, 2) loss of the high energy ^{3}He minority tail itself, and 3) ICRH-wave-induced deconfinement of previously confined D-D or D-^{3}He fusion products. The measurements at the detector 90^0 below the midplane were generally consistent with the first process, while the measurements at 45^0 below the midplane suggested the additional influences of one or both of the latter two processes.

The first-orbit loss of the D-^{3}He alpha particle was initially

suggested by the time dependence of its emission, which coincided with an increased MeV ion loss during the application of ICRH power in the ^{3}He minority heating mode. For instance, the MeV ion loss signal to the detector 90^0 below the midplane increased by a factor of 2-3 with $\approx$4 MW of ICRH during $\approx$20 MW of NBI, despite the fact that the D-D neutron rate did not increase during the ICRH. The measured gyroradius and pitch angle dependence of the MeV ion loss during ICRH were were also approximately consistent with the expected first-orbit loss of alphas, which has gyroradius and single-particle confinement similar to the D-D fusion products normally seen during NBI. The somewhat larger than expected gyroradius observed for the ICRH-only case could be explained by the Doppler shift due to a ^{3}He tail temperature in the calculated range of 0.4-0.8 MeV.

By tentatively assuming that the MeV ion loss to the 90^0 detector was entirely due to first-orbit loss of alphas, the rate of D-^{3}He alpha particle production and its approximate radial profile were inferred by comparison with D-D fusion product loss. The resulting D-^{3}He reaction rate profile was similar to the D-D reaction rate profile during NBI, i.e. with a Gaussian FWHM/a$\approx$0.5, and the inferred total reaction rate was up to $\approx 10^{16}$ reactions/sec with 3-4 MW ICRH. These experimental inferences agreed well with model calculations for the D-^{3}He reaction rate based on ICRH wave physics for the one case studied, although there are systematic uncertainties of at least x3 in the inference of the absolute D-^{3}He reaction rate by this means, particularly since the lost alpha fraction at 1.4 MA is only about 10% [18].

The alpha loss was also measured as a function of the ICRH heating power. With ICRH-only the lost alpha signal at 90^0 increased proportionally to $\approx$(ICRH power)^3 within the ICRH-only power range 1.0-4.5 MW, but with ICRH+NBI($\approx$15-20 MW) the lost alpha signal increased approximately linearly with RF power in this range. At the maximum ICRH power of $\approx$4 MW the alpha loss rate (and probably the alpha creation rate) was $\approx$5 times larger during simultaneous NBI, most likely

due to the lower fast ion drag at the larger electron temperature in the latter case.

The main anomaly with this simple picture was that the ICRH-induced MeV ion loss 45^0 below the outer midplane was a factor of 3-10 times larger than expectations based on the observed D-D fusion product loss at this location. Several possible sources for this extra loss were discussed, including modified first-orbit loss due a possibly very narrow or asymmetric source profile, and the mechanisms #2 and #3 above. The modified first-orbit loss models were insufficient to explain the results; however, given the present lack of a clear physical model for the latter two processes, there is not yet a unique quantitative explanation for the anomalously large loss observed at 45^0.

Further progress in distinguishing between these three basic loss mechanisms could be made using majority and minority species scans with both ICRH-only and ICRH+NBI. For example, replacement of the D majority with ^{4}He could separate the D-^{3}He alpha production from the ^{3}He tail loss (brief experience with ICRH-only ^{4}He majority discharges in the 1990 run showed little or no MeV ion loss, confirming the dominant alpha particle contribution to the loss in the present D majority case. Also, varying the D-D reaction rate due to NBI with a fixed ICRH power could separate the possible wave-induced D-D fusion product loss from the other processes.

The most important near-term application of this study is to help anticipate complications which will arise during the interpretation of MeV ion loss during D-T discharges with simultaneous ^{3}He minority heating, such as planned for TFTR and JET. In those cases the fast ion populations in the ^{3}He tail should still be larger than the D-T alpha populations, therefore the direct loss due to the ^{3}He tail or to ICRH-deconfined D-D fusion products would need to be understood separately from the fusion-product alpha effects. In the longer term, if the D-^{3}He reaction rate can be increased to $\approx 10^{18}$ reactions/sec, then the resulting

confined alphas (and protons) might be used to simulating alpha particle collective effects without the use of D-T fuel [34].

Acknowledgments:

We thank E. Fredrickson, J. Hosea, L. Johnson, D. Mikkelsen, D.K. Owens, J.Y. Park, J.D. Strachan, J. Stevens, and K.M. Young for contributions to this project.

References

1) The JET Team, Plasma Physics and Controlled Nuclear Fusion Research, Proc. 13th Intl. Conf., Washington, 1990, Vol. 1, p. 679, IAEA, Vienna.

2) HOSEA, J.C., et al, Plasma Physics and Controlled Nuclear Fusion Research, Proc. 13th Intl. Conf., Washington, 1990, IAEA, Vienna, paper IAEA-CN-53/E-1-5.

3) FURTH, H.P, GOLDSTON, R.J., ZWEBEN,S.J., and SIGMAR, D.J., Nucl. Fus. **30**, 1799 (1990)

4) FUNAHASHI, A. and the JT-60 Team, Proc. 1991 European Physical Society Meeting, Berlin, Germany, paper A43, I-169.

5) SADLER, G.J., CONROY, S.W., JARVIS, O.W., van BELLE, P., ADAMS, J.M., and HONE, M.A., Fusion Technology **18**, 556 (1990).

6) MEDLEY, S., PPPL, private communication (1991)

7) ZWEBEN, S.J., BOIVIN, R.L., DIESSO, M., Hayes, S., HENDEL, H.W., et al, Nucl. Fus. **30**, 1551 (1990)

8) MANOS, D.M., STANGEBY, P.C., BUDNY, R.V., COHEN, S.A., KILPATRICK, S, and SATAKE, T., J. Nucl. Mat. 129 (1984) 319

9) HOSEA, J., PHILLIPS, C.K., STEVENS, J., Wilson, R., et al, Princeton Plasma Physics Laboratory Report PPPP-2738 (1991).

10) CHANG, C.S., HAMMETT, G.W., GOLDSTON, R.J., Phys. Fluids B 2 (1990) 2383.

11) CHEN, L., VACLAVIK, J, and HAMMETT, G., Nucl. Fus. **28** (1988) 389.

12) CHANG, C.S., Phys. Fluids B3 (1991) 256.

13) MURPHY, T.J. and STRACHAN, J.D., Nucl. Fus. **25** (1985) 383.

14) CHRIEN, R.E. and STRACHAN, J.D., Phys. Fluids 26, 1953 (1983).

15) HEIDBRINK, W.W., CHRIEN, R.E., and STRACHAN, J.D., Nucl. Fus. 23 (1983) 917.

16) STRACHAN, J.D., Nucl. Fus. 29 (1989) 163.

17) MARTIN, G., JARVIS, O.N., KALLNE, J., MERLO, V., SADLER, G., and Van BELLE, P., Physica Scripta T16, 171 (1987).

18) BOIVIN, R. Ph. D. Thesis, Princeton University, Oct. 1991

19) FELT, J., BARNES, C.W., CHRIEN, R.E., HEIDBRINK, W.W., MANOS, D. , and ZWEBEN, S., Rev. Sci. Inst. **61** (1990) 3262

20) ZIEGLER, J.F., Helium Stopping Powers and Ranges in all Elemental

Materials, Vol. 4, Pergamon Press, New York, 1977.

21) SADLER, G., et al, Proc. IAEA Technical Committee Meeting on Alpha Particles, Goteborg, Sweden, 1991 (to be published).

22) JOHNSON, L., PPPL, private communication (1991).

23) ZWEBEN, S.J., BOIVIN, R., CHANG, C.S., HAMMETT, G.H., and MYNICK, H.E., PPPL Report PPPL-2770 (1991), to be published in Nuclear Fusion.

24) BOIVIN, R., KILPATRICK, S., MANOS, D., and ZWEBEN, S., Rev. Sci. Inst. 61 (1990) 3206.

25) JASSBY, D., et al, Phys. Fluids B3 (1991) 2309.

26) BOYD, D.A., CAMPBELL, D.J., CORDEY, J.G, CORE W.G.F., et al, Nuclear Fusion **29** (1989) 593; also, JACQUINOT, J., SADLER, G. and the JET team, JET-P(91)07, 1991.

27) STIX, T.H., Nuclear Fusion **15** (1975) 737.

28) COTTRELL, G.A. and START, D.F., Nuclear Fusion 31, 61 (1991).

29) SMITHE, D.N., COLESTOCK, P.L., Kashuba, R.J., KAMMASH, T., Nuclear Fusion **27** (1987) 1319.

30) SMITHE, D.N., PHILLIPS, C.K., HAMMETT, G.W., COLESTOCK, P.L. "SNARF analysis of ICRF heating on TFTR", in the proceedings of the Eighth Topical Conference on Radio-Frequency Power in Plasmas, (Irvine, CA, 1989), Roger McWilliams, editor, (AIP Conference Proceedings 190).

31) HAMMETT,G.W., "Fast Ion Studies of Ion Cyclotron Heating in the PLT Tokamak", Ph.D. Dissertation (Princeton, 1986).

32) HAMMETT, G.W., DORLAND, W., KAITA, R., MEDLEY, S.S., SMITHE, D.N., and COLESTOCK, P.L., "Analysis of Charge Exchange Measurements During ICRF and ICRF+NBI Heating in TFTR", in the proceedings of the Eighth Topical Conference on Radio-Frequency Power in Plasmas, (Irvine, CA, 1989), Roger McWilliams, editor, (AIP Conference Proceedings 190).

33) HEIDBRINK, W.W., ReV. Sci. Inst. **56**, 1098 (1985); also Nucl. Inst. and Methods in Physics Research, **A236**, 380 (1985).

34) YAMADA, M., PPPL, private communication (1991).

Figure Captions

1) Layout of the escaping MeV ion detectors in TFTR. The #6, #9 and #11 detectors of the poloidal array are nearly identical but located at 90^0, 60^0, and 45^0 poloidally below the outer midplane, respectively. The "midplane" detector is of a similar design but inserted through the porthole above #11.

2) Mechanical design of the MeV ion detectors. The 2.5 cm x 2.5 cm ZnS(Ag) scintillator screen lies face-down at the top of a light-tight box. The pinhole/slit aperture pair defines the toroidal pitch angle χ and gyroradius ρ of particles hitting the screen. The two dimensional (ρ,χ) light emission pattern from the screen is viewed by an intensified video camera through a lens+fiber bundle imaging system.

3) Typical MeV ion signal vs time for the 90^0 detector showing the increased MeV ion loss due to D-^{3}He fusion reactions during ICRH. In (a) is a case with $\approx$3.1 MW of ICRH added to 19.5 MW NBI, and in (b) is a very similar case but without the ICRH. The 2.5 MeV neutron rate is shown in both cases, normalized to the D-D fusion product loss for the NBI-only case. These signals were obtained from a PM tube monitoring a spot near the peak emission region in (ρ,χ) at the scintillator.

4) MeV ion loss signals vs time for the 90^0 detector during ICRH. In 4(a) is a comparison between the MeV ions loss with 19 MW of NBI and a very similar shot with 19 MW plus an additional 5.2 MW of ICRH. In 4(b) is a shot in which 4.6 MW of ICRH-only was applied shortly after deuterium pellet injection. These signals were obtained using the video camera, and are integrated over the peak region of the (ρ,χ) plane. After correction for the different camera gating times, the ICRH-induced part of the signal in case (a) is $\approx$5 times larger than that in (b). However, the 2.5 MeV neutron rate in the ICRH-only shot was only about 1/100th that in the NBI+ICRH shot, as shown in Fig. 4(c), implying that the detected signal with ICRH-only is almost entirely due to D-^{3}He

reactions.

5) The 2-D scintillator light emission pattern vs the MeV ion coordinates (ρ,χ) for an ICRH-only shot in 5(a) and for a NBI-only shot in 5(b), both of which were taken at 1.4 MA. To a first approximation, the (ρ,χ) pattern is similar in (a) and (b), as expected for the loss of 3.7 MeV alphas for the ICRH-only case (since the gyroradius is similar for these alphas and D-D fusion products).

6) MeV ion pitch angle distributions χ, averaged over ρ=2-11 cm. In 6(a) is a comparison between the ICRH-only and NBI-only shots of Fig. 5 showing a similar pitch distribution, as expected for first-orbit loss of 3.7 MeV alphas in the ICRH-only case. In 6(b) is a comparison of the ICRH-only data with first-orbit model predictions assuming two different source profile distributions, with FWHM/a=0.2 and 0.5. The latter agrees better, as expected from the comparison in 6(a), since for the D-D fusion products the source profile was measured to be FWHM/a=0.4-0.5.

7) MeV ion gyroradius distributions for the ICRH-only and NBI-only cases of Fig. 5. The gyroradius distribution for the ICRH-only case has a peak location at $\rho\approx$6.8 cm, somewhat larger than the ρ=5.4 cm expected for 3.7 MeV alphas (and larger than that for the D-D fusion products in the NBI-only case). This is most likely due to the large Doppler spread in the alpha birth energy distribution.

8) Comparison between loss orbits to the 90^0 detector for 3.7 MeV alphas and 15 MeV protons at 1.4 MA in 8(a) and 2.0 MA in 8(b). In all cases these orbits are the ones with the largest expected first-orbit loss, i.e. the orbits which pass closest to the high-source rate region near the plasma center. The 15 MeV protons can be lost to the detector from near the plasma center at both of these currents.

9) Comparison between the expected gyroradius distributions for first-

orbit loss of 3.7 MeV alphas and 15 MeV protons. Although a large contribution from the 15 MeV protons seems to be able to explain the peak location in the data, the expected efficiency for the detection of 15 MeV protons is actually too low to do so.

10) Comparison between the expected pitch angle distributions for 3.7 MeV alphas and 15 MeV protons and the data for the 1.4 MA ICRH-only case. The first orbit loss of 15 MeV protons is expected to peak at $\chi \approx 78^0$, in contrast to the observed peak near 67^0, implying that the first-orbit loss of 15 MeV protons is not contributing significantly to the results.

11) Comparison between the pitch angle distributions for the low gyroradius and high gyroradius parts of the same 2-D scintillator pattern for the 1.4 MA ICRH-only case. At the high gyroradius region of the pattern there is only a small component which could be attributed to the first-orbit loss of 15 MeV protons at their expected $\chi \approx 78^0$.

12) In 12 (a) is the MeV ion loss signal vs time for a 2.0 MA shot with 3.7 MW ICRH and 23 MW NBI (#54316). The MeV ion loss during ICRH increases by a factor of 2-3 above the level for a similar shot with no ICRH, while the 2.5 MeV neutron rate does not increase during ICRH, similarly to the 1.4 MA case in Fig. 4(a). In 12(b) is a 2.0 MA ICRH-only show with 4.1 MW of ICRH, which behaves similarly to the 1.4 MA ICRH-only shot of Fig. 4(b).

13) Pitch angle distributions of the MeV ion loss at 2.0 MA for the ICRH+NBI (at 3.6-3.9 sec) and ICRH-only cases of Fig. 12. The peak pitch angle shifts to lower χ than for the 1.4 MA case, and is very similar to that for a NBI-only shot at the same NBI power (#54308), as expected for the first-orbit loss of 3.7 MeV alphas. The calculated pitch distribution for the assuming a source profile with FWHM/a=0.5 is somewhat narrower than the data.

14) Comparison of the pitch angle distributions for the NBI-only and ICRH+NBI parts of the same 1.4 MA and 2.0 MA discharges (#54271 and #54316). Their similarity implies that the D-^{3}He source profile during ICRH is similar to the D-D source profile during NBI.

15) Calculated "fattest banana" orbits for detectors at poloidal angles of 90^0 and 45^0 (for 3 MeV protons) for plasma currents of 1.4 MA and 2.0 MA. The detector at 45^0 can detect loss orbits originating closer to the high source region near the plasma center. Also shown in 15(c) are typical orbits of 0.5 MeV ^{3}He tail ions, with banana tips located at the resonant layer.

16) Calculated ratio of the expected first-orbit loss to the detector at 45^0 compared to the detector at 90^0 (for 1.4 MA), integrated over the $\chi \approx 45^0$-85^0 detector acceptance range, plotted as a function of the assumed source profile width. As the assumed source profile narrows, the expected $45^0/90^0$ ratio increases due to the orbit effect shown in Fig. 15(a).

17) MeV ion loss signals measured by the 45^0 detector vs time for 1.4 MA and 2.0 MA cases with ICRH+NBI. The MeV ion loss increases by a factor of >10 during ICRH (compared with the same shot during NBI-only). This increase is much larger than the corresponding increase in the 90^0 detector, e.g. Figs. 4(a) and 12(a).

18) Measured $45^0/90^0$ MeV ion loss ratio for a set of 1.4 MA discharges. This ratio is higher for ICRH-only than for NBI-only shots, and increases with ICRH power for ICRH+NBI shots. This data is taken from the video camera signals near the peak of the D-D and D-^{3}He (χ,ρ) patterns.

19) Patterns of the scintillator light emission in the 45^0 detector for three different shots in Fig. 18. The patterns for the NBI-only in (a) and ICRH-only in (b) are consistent with first-orbit loss of D-D and D-^{3}He ions. The pattern with ICRH+NBI in (c) shows a distortion toward lower

ρ and higher χ apparently associated with non-first orbit loss of MeV ions. A similar distortion with ICRH+NBI is shown in (d), but at 1.8 MA.

20) Comparison of the ρ and χ distributions for the three 45^0 detector, 1.4 MA patterns shown in Fig. 19. The ICRH+NBI case has a peak χ higher than either the NBI-only or ICRH-only cases, but a peak ρ similar to that for the NBI-only case. This anomaly suggests that the loss in the ICRH+NBI case is not simple first-orbit loss.

21) Variation of the ICRH-induced MeV ion loss signal with ICRH power in both the 90^0 and 45^0 detectors, for a set of 1.4 MA ICRH-only discharges. The loss to both detectors increases proportionally to (ICRH power)^3 in this range.

22) Variation in the ICRH-induced MeV ion loss to the 90^0 detector vs ICRH power for a set of ICRH+NBI discharges, as monitored by a PM tube. The relative ICRH-induced loss was determined by subtracting out the MeV ion loss signal expected for first-orbit loss of D-D fusion products. The ordinate also represents the inferred global D-^{3}He reaction rate (in units of 10^{15} reactions/sec), calculated by normalizing to the measured D-D ion loss during the NBI-only part of each shot, and assuming an escaping alpha energy of 3.7 MeV.

23) Variation in the MeV ion loss to the 90^0 detector vs ICRH power for another set of 1.4 MA ICRH+NBI discharges, compared with the MeV ion loss for a set of ICRH-only discharges. A given level of ICRH power produces more MeV ion loss during NBI than without simultaneous NBI, suggesting that the D-^{3}He reaction rate is larger in the former case. The ordinate again represents the inferred global D-^{3}He reaction rate (in units of 10^{15} reactions/sec), assuming that the signals are predominantly from first-orbit loss of 3.7 MeV alphas.

24) Calculation of the D-^{3}He reaction rate profile and its effective tail energy for a 2 MA ICRH+NBI case (#54320). The calculated total

reaction rate is $\approx 10^{16}$/sec, and the central tail temperature is $\approx$1 MeV. These are at least qualitatively similar to the inferences from the lost alpha measurements. This modeled shot had $T_e(0)$=9.4 keV, $n_e(0)=5.1\times10^{13}$ cm^{-3}, and $n(^3He)/n_e \approx 1.25\%$.

25) Calculated detector response curves vs inferred gyroradius for various assumed alpha energies compared with the data from an ICRH-only case at 90^0. Each model curve was calculated using the known geometrical and optical detector resolutions, the appropriate foil attenuation factors, and the estimated scintillator light output for that energy (an equal number of incident alphas was assumed for all cases). The best fit to the data is for E$\approx$6 MeV.

26) Model calculations showing the expected $45^0/90^0$ ratio for first-orbit loss of alphas with an asymmetrical vertically-elongated source profile. For both curves the profile was assumed to have a horizontal Gaussian FWHM=10 cm with a variable major radial location. The vertical source profile shape was a Gaussian with FWHM/a indicated. The resulting $45^0/90^0$ signal ratios can increase by only about 50% above the nominal 0.4 calculated for a symmetrical profile with FWHM/a=0.5, i.e. not quite enough to explain the data of Fig. 18.

TABLE 1: Shot List for D-^{3}He

Shot Range	I(MA)	ICRF (MW)	NBI (MW)	Detector
51712-51735	1.4	≤ 3.6	14 - 10	PM + Camera
51783-51798	1.6	≤ 2.9	10 - 17	PM + Camera
53220-53244	1.4	≤ 3.4	14-26	Camera
54264-54281	1.4	≤ 5.2	12 - 24	Camera
54308-54320	2.0	≤ 5.0	11 - 23	Camera
55505-55540	1.4	≤ 4.2	0	Camera
55451-55454	2.0	≤ 4.0	0	Camera

PPPL#91X0299

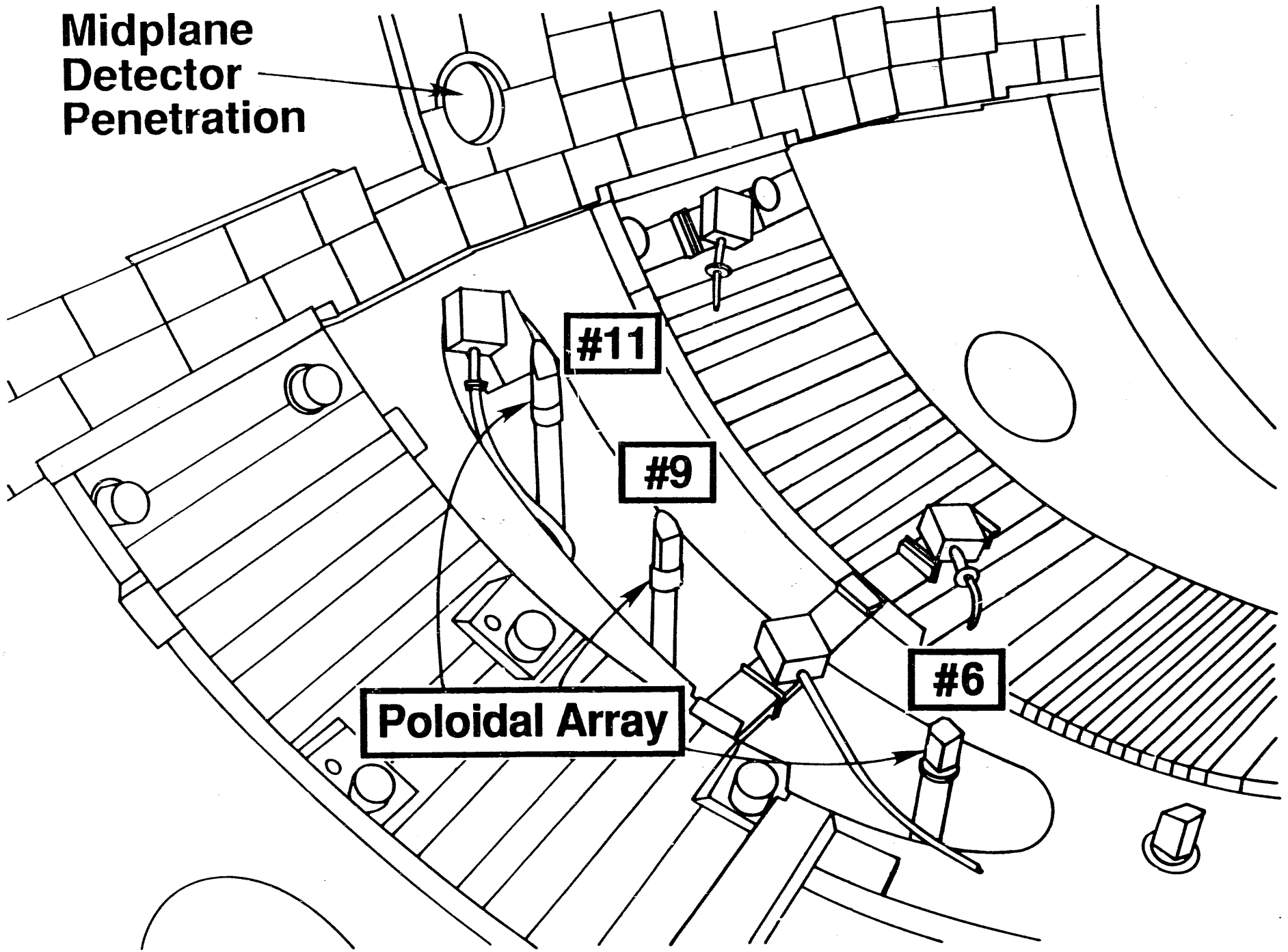

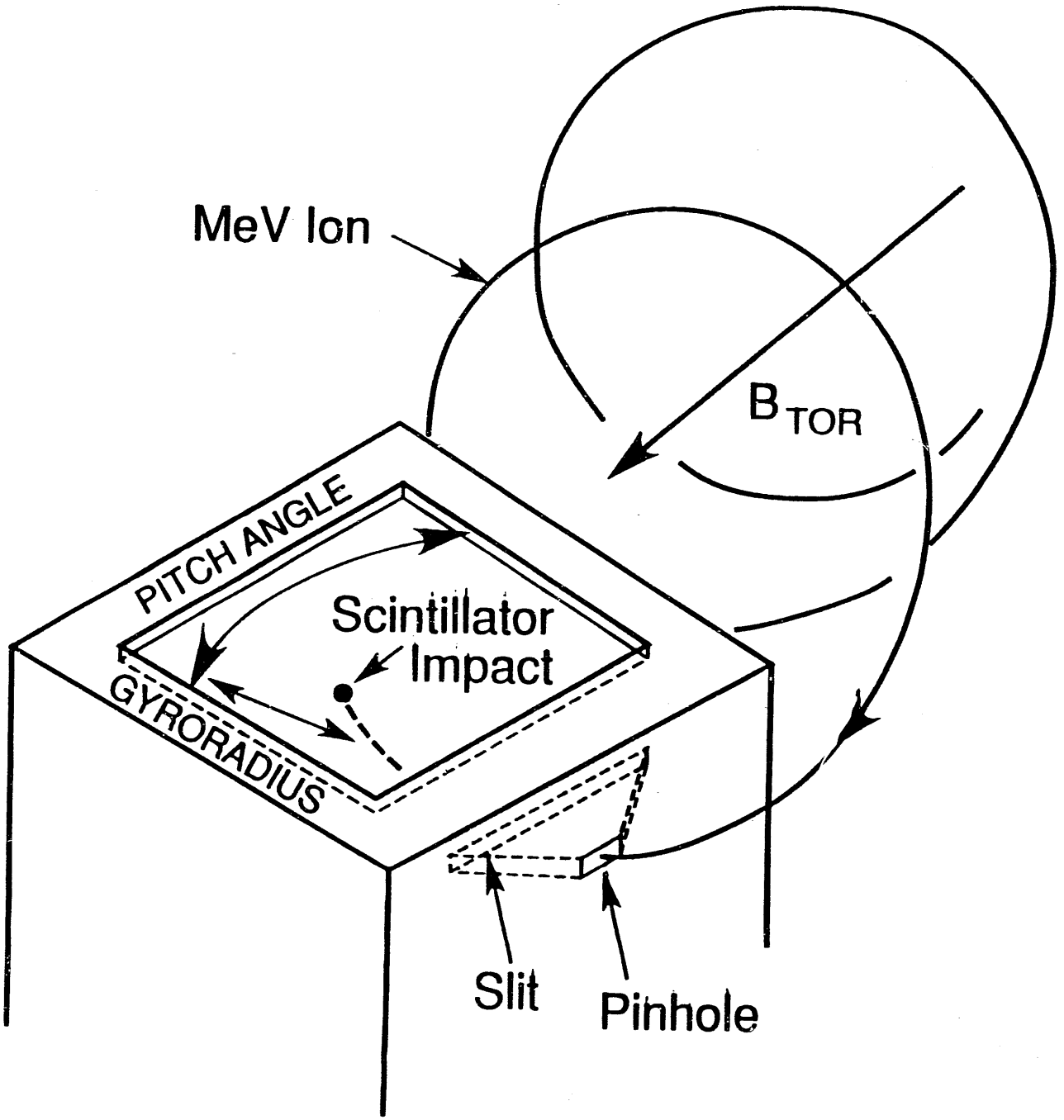
MeV Ion
B_{TOR}
PITCH ANGLE
Scintillator
Impact
GYRORADIUS
Slit
Pinhole

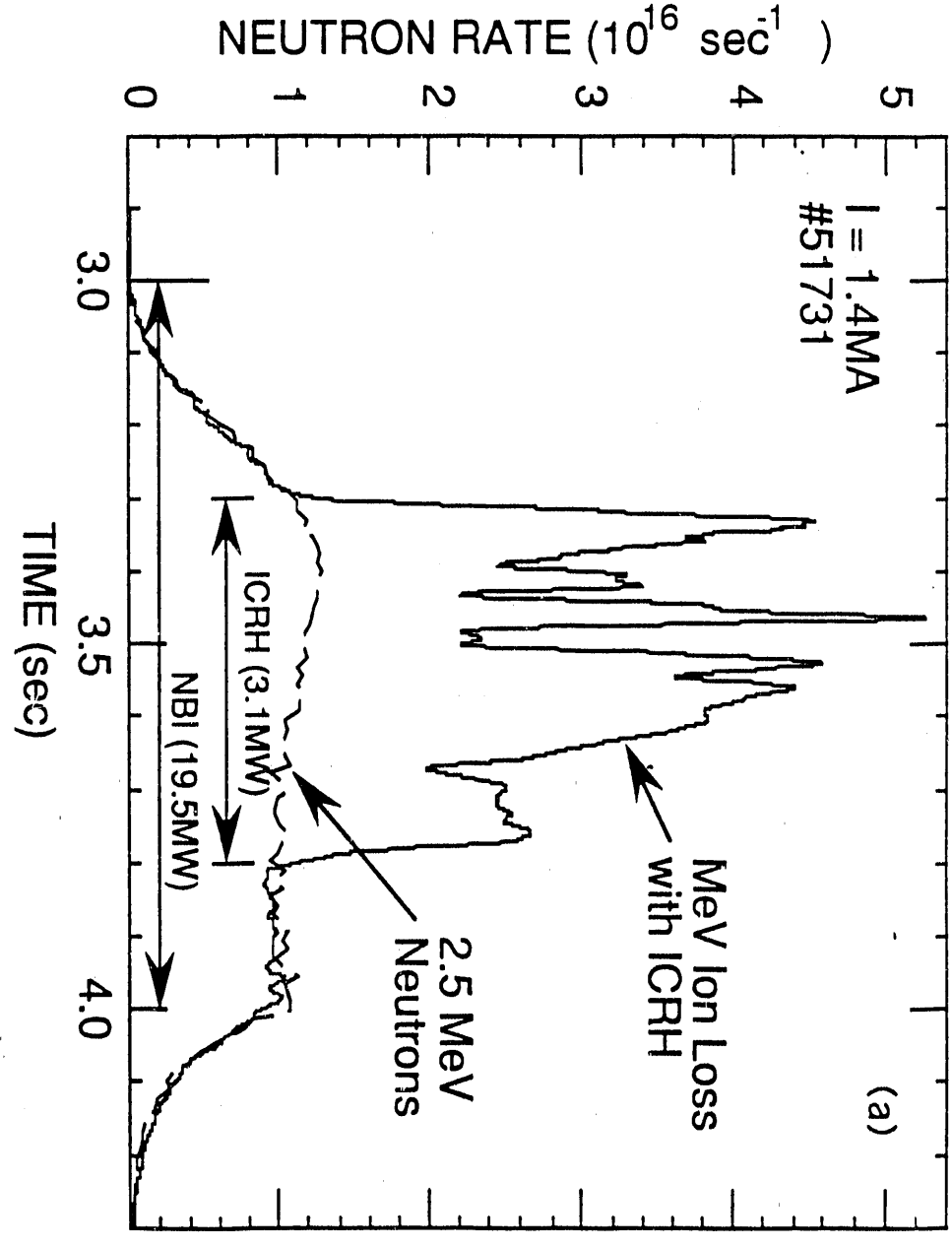
NEUTRON RATE (10^{16} sec^{-1})
0
1
2
3
4
5
I = 1.4MA
#51731
(a)
MeV Ion Loss
with ICRH
2.5 MeV
Neutrons
ICRH (3.1MW)
NBI (19.5MW)
3.0
3.5
4.0
TIME (sec)
PPPL#91X0436

3(a)

3(b)

PPPL#91X0437
(b)
I = 1.4MA
#51734
MeV Ion Loss
without ICRH
2.5 MeV Neutrons
Normalized
NBI (19.5MW)
NEUTRON RATE (10^{16} sec^{-1})
TIME (sec)
0
1
2
3
4
5
3.0
3.5
4.0

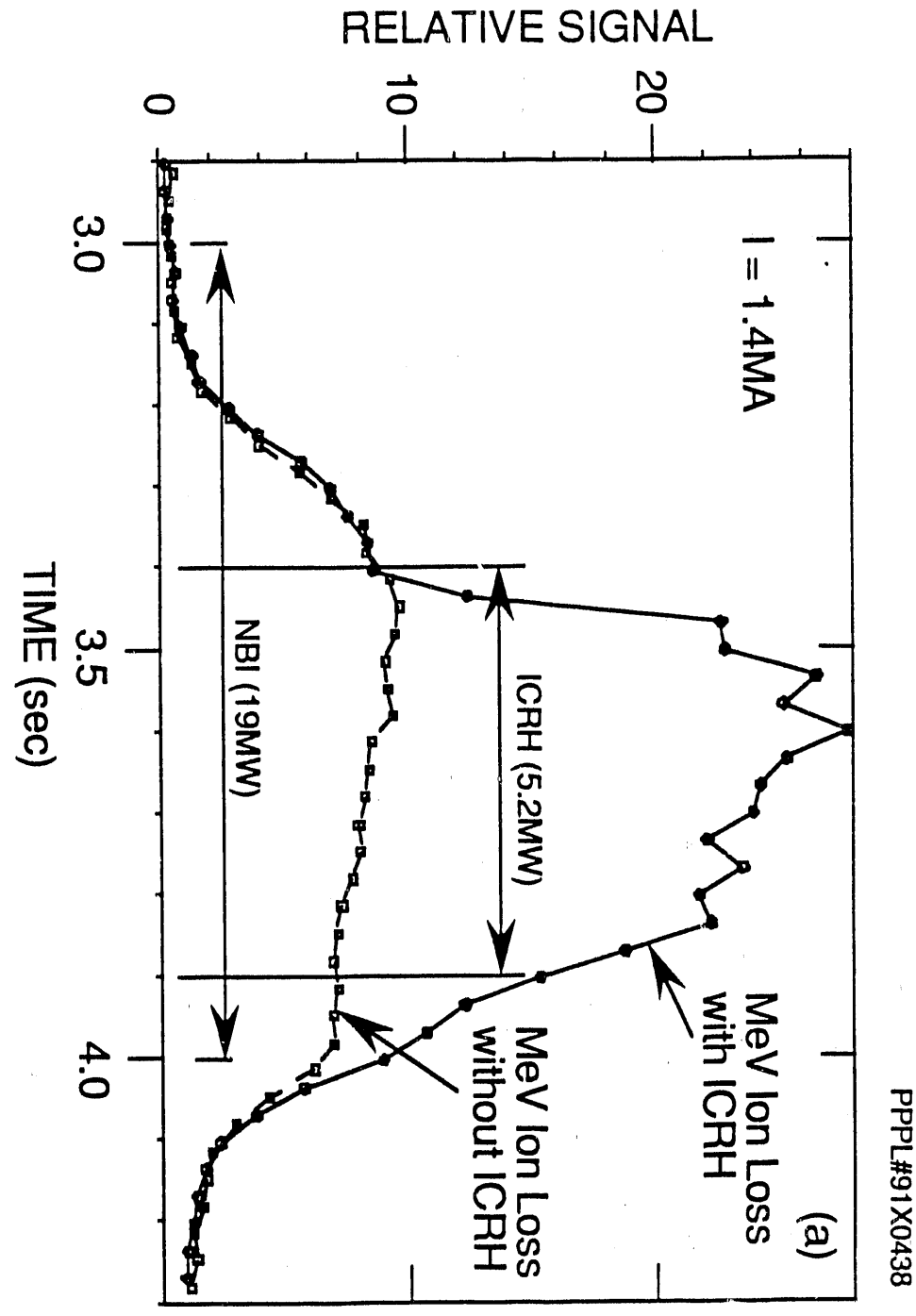
RELATIVE SIGNAL
0
10
20
3.0
3.5
4.0
TIME (sec)
I = 1.4MA
NBI (19MW)
ICRH (5.2MW)
MeV Ion Loss
with ICRH
MeV Ion Loss
without ICRH
(a)
PPPL#91X0438

4(a)

PPPL#91X0439
(b)
MeV Ion Loss
ICRH–Only
(#55540)
ICRH (4.6MW)
RELATIVE SIGNAL
0
10
20
3.5
4.0
4.5
TIME (sec)

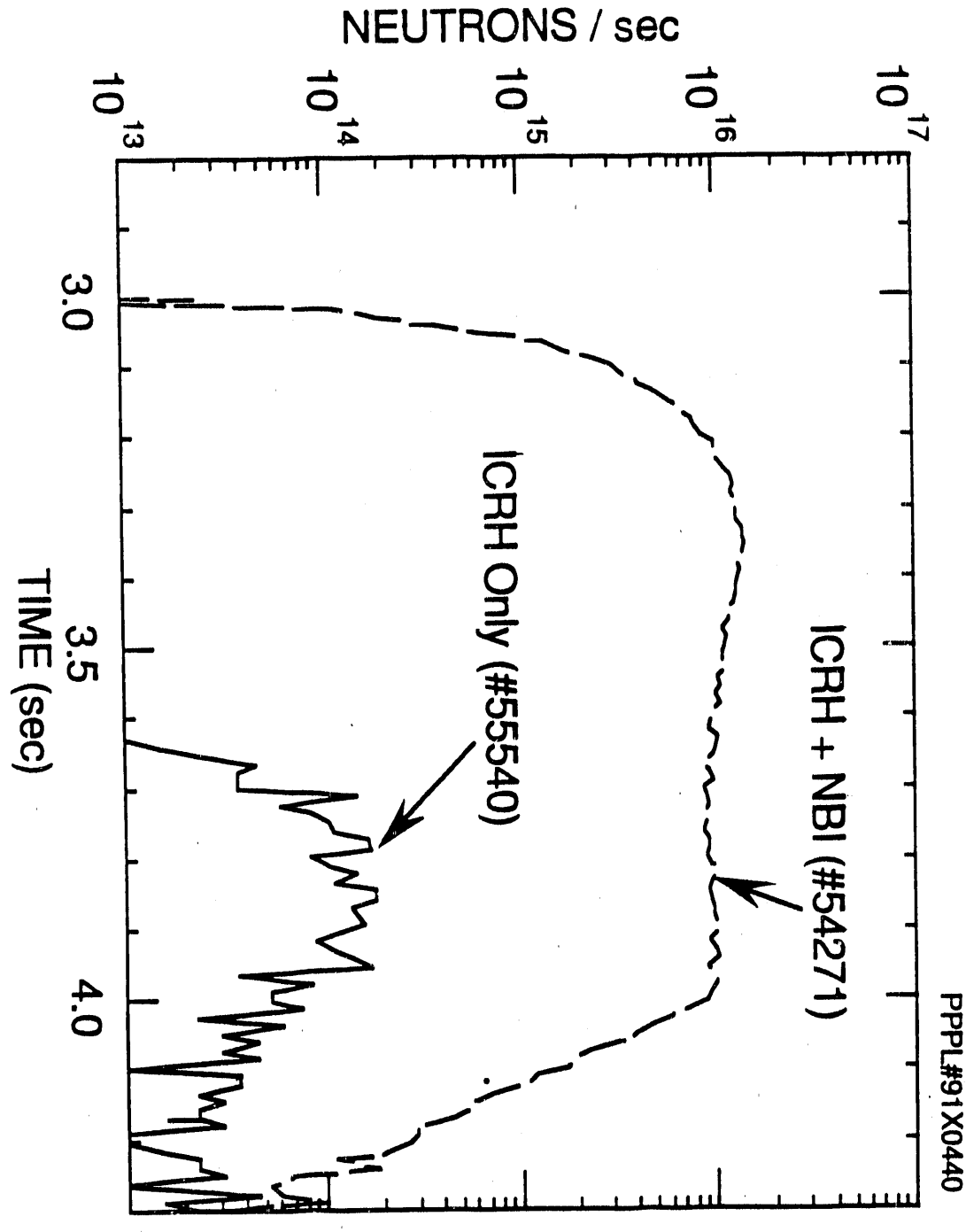
NEUTRONS / sec
10^{13}
10^{14}
10^{15}
10^{16}
10^{17}
3.0
3.5
4.0
TIME (sec)
ICRH Only (#55540)
ICRH + NBI (#54271)
PPPL#91X0440

4(c)

PPPL#91X0441
(a)
90° Detector, ICRH-only
(#55540)
11 cm
2 cm
45°
90°
ρ
χ
LINE
-10
-20
-30
10
20
30
PIXEL

5(a)

PPPL#91X0442
(b)
90° Detector, NBI-only
(#54274)
11 cm
2 cm
45°
90°
ρ
χ
LINE
-10
-20
-30
10
20
30
PIXEL

5(b)

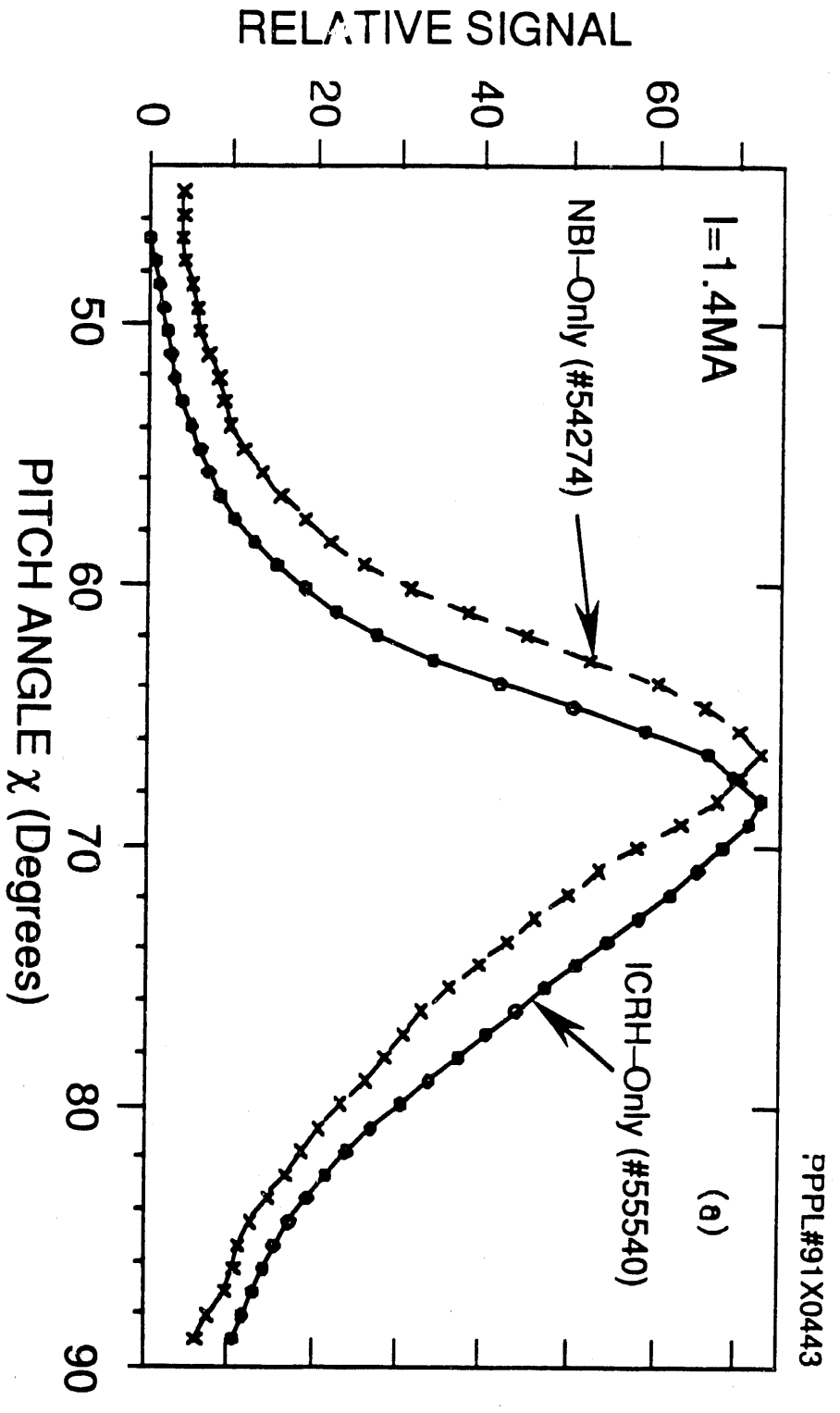
RELATIVE SIGNAL
0
20
40
60
I=1.4MA
NBI–Only (#54274)
ICRH–Only (#55540)
(a)
PPPL#91X0443
50
60
70
80
90
PITCH ANGLE χ (Degrees)

6(a)

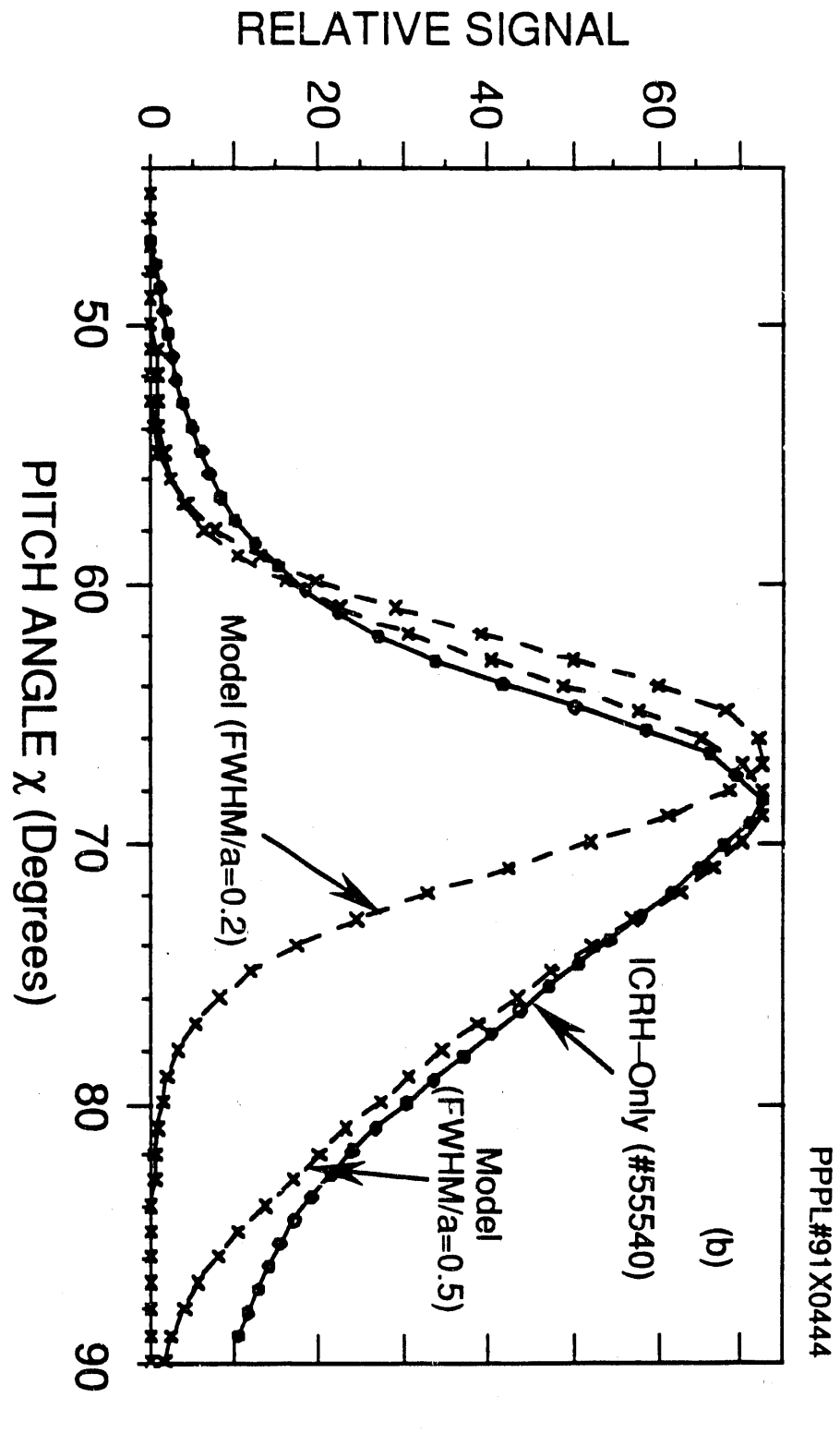
RELATIVE SIGNAL
0
20
40
60
50
60
70
80
90
PITCH ANGLE χ (Degrees)
Model (FWHM/a=0.2)
ICRH–Only (#55540)
Model
(FWHM/a=0.5)
(b)
PPPL#91X0444

6(b)

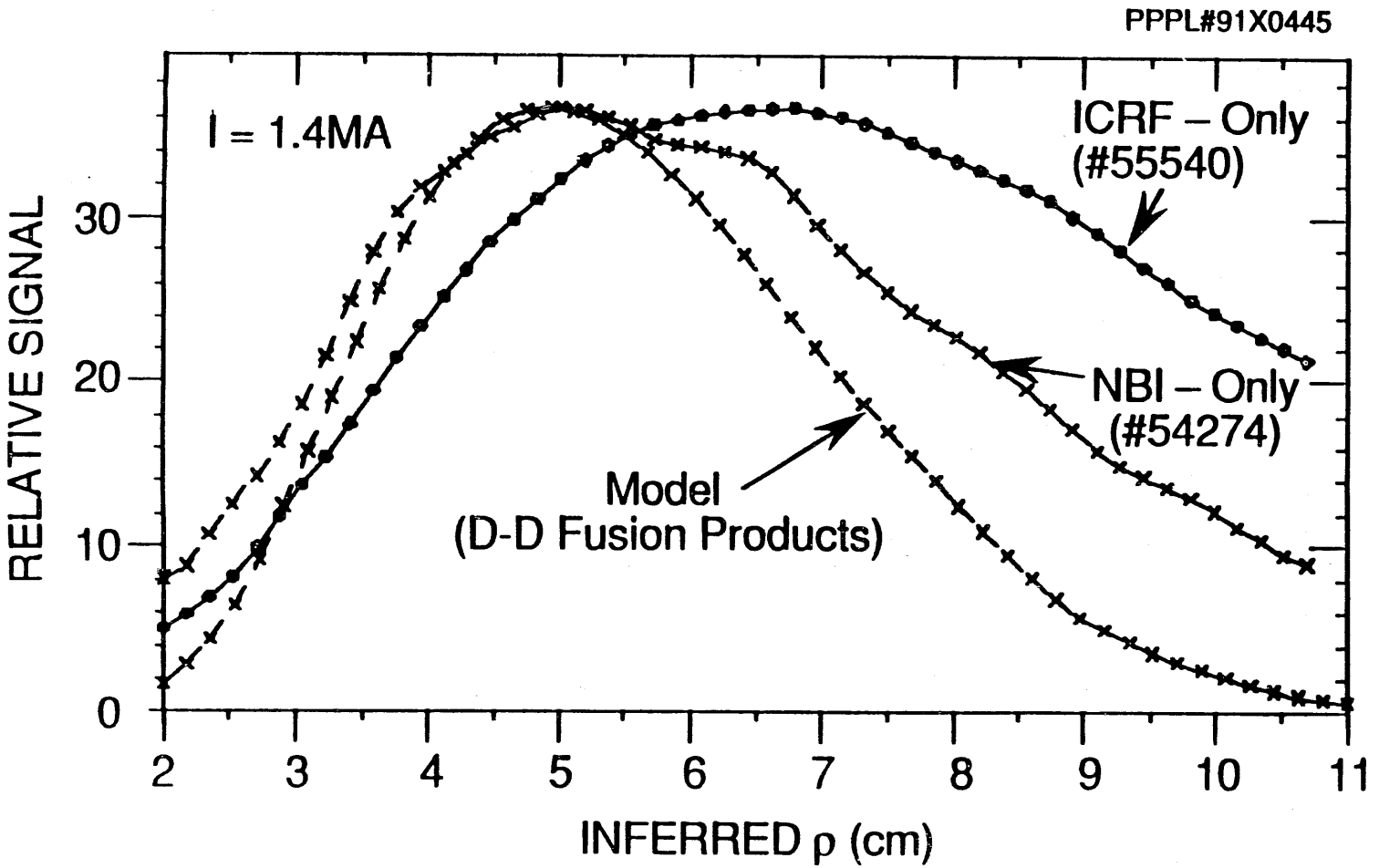
PPPL#91X0445
I = 1.4MA
ICRF – Only
(#55540)
NBI – Only
(#54274)
Model
(D-D Fusion Products)
RELATIVE SIGNAL
0
10
20
30
2
3
4
5
6
7
8
9
10
11
INFERRED ρ (cm)

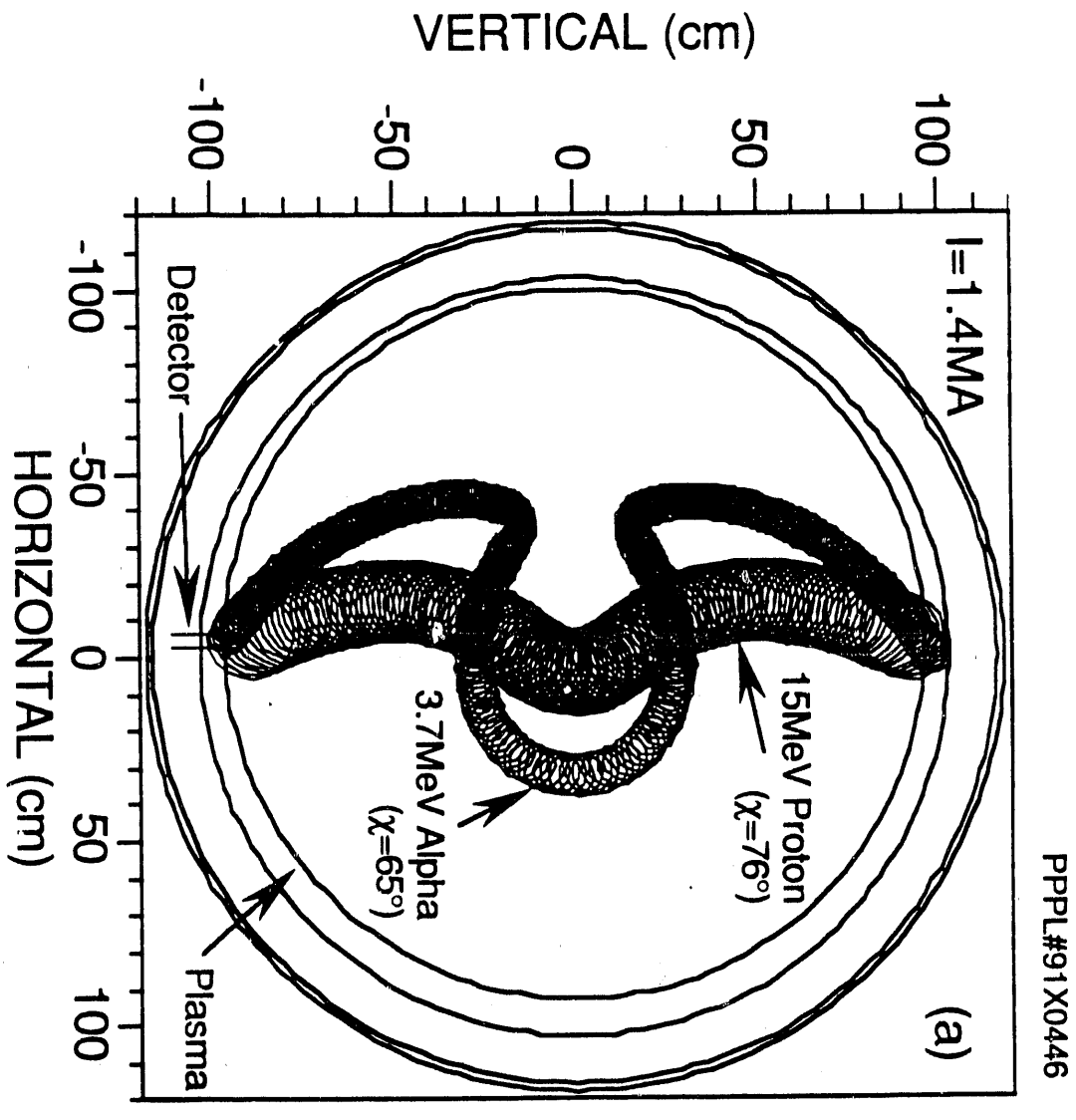
VERTICAL (cm)
-100
-50
0
50
100
I=1.4MA
(a)
PPPL#91X0446
Detector
15MeV Proton
(χ=76°)
3.7MeV Alpha
(χ=65°)
Plasma
HORIZONTAL (cm)
-100
-50
0
50
100

8(a)

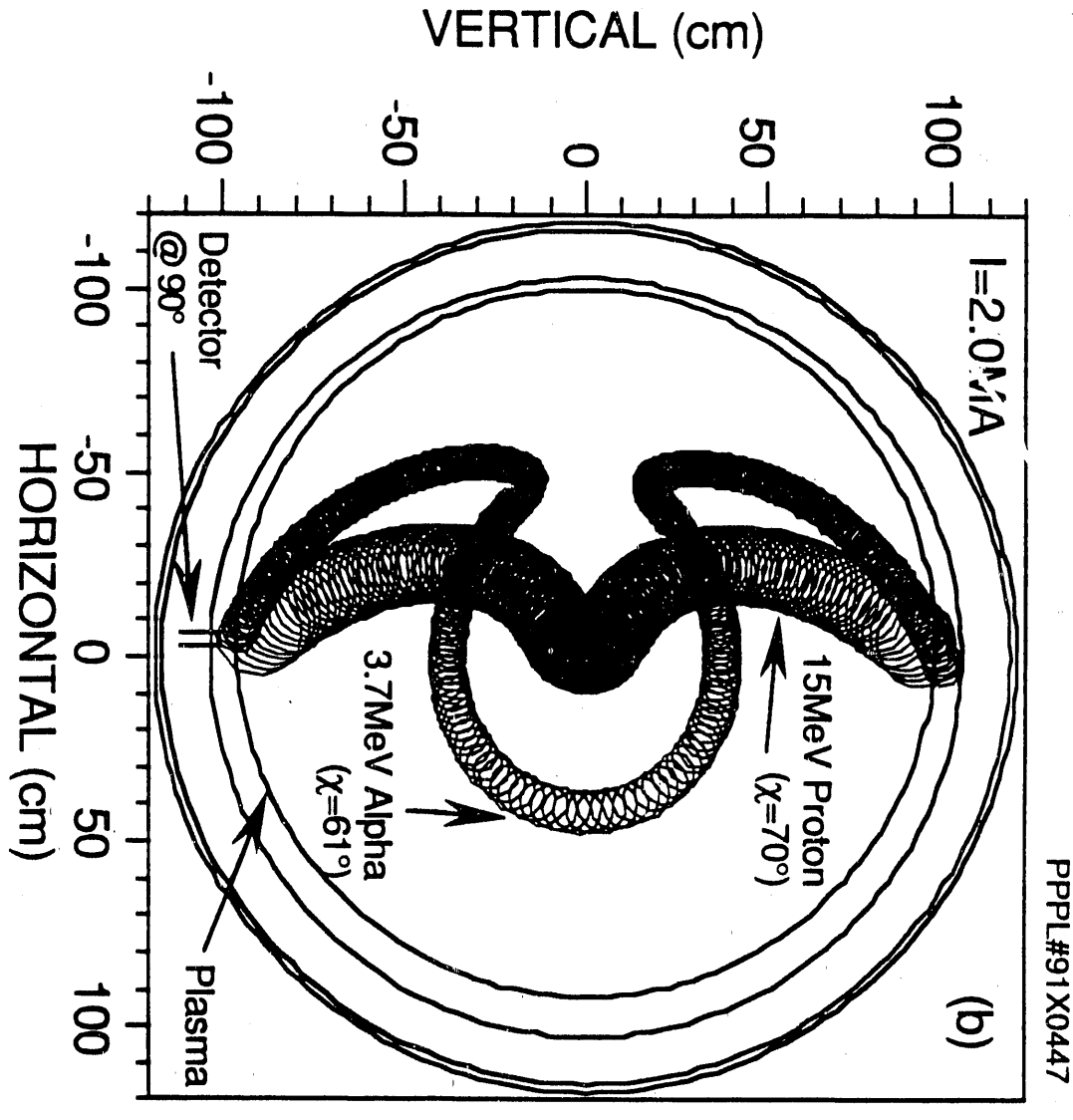
VERTICAL (cm)
-100
-50
0
50
100
HORIZONTAL (cm)
-100
-50
0
50
100
I=2.0MA
Detector
@90°
15MeV Proton
(χ=70°)
3.7MeV Alpha
(χ=61°)
Plasma
(b)
PPPL#91X0447

8(b)

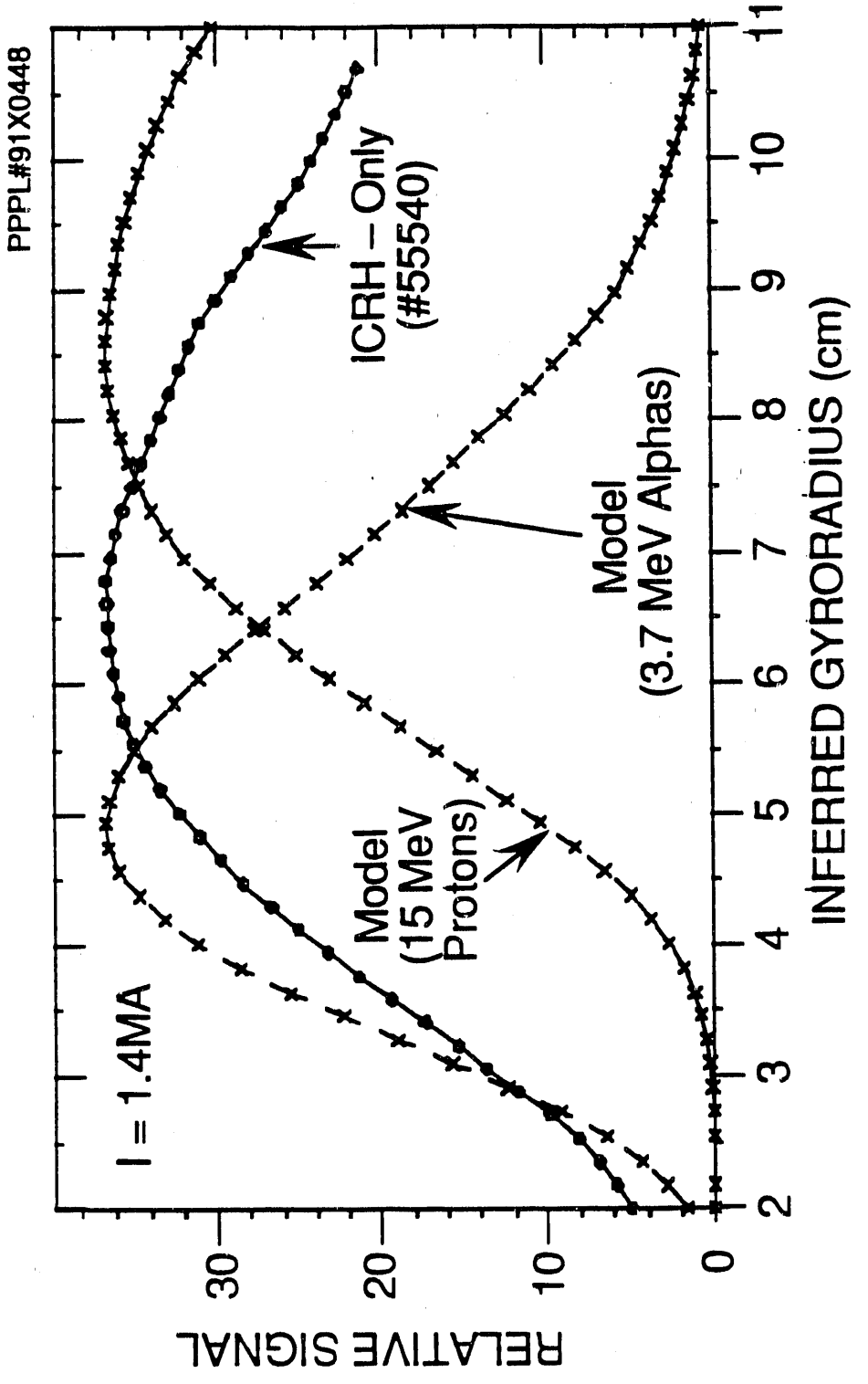
PPPL#91X0448
I = 1.4MA
ICRH – Only
(#55540)
Model
(15 MeV
Protons)
Model
(3.7 MeV Alphas)
RELATIVE SIGNAL
INFERRED GYRORADIUS (cm)
0
10
20
30
2
3
4
5
6
7
8
9
10
11

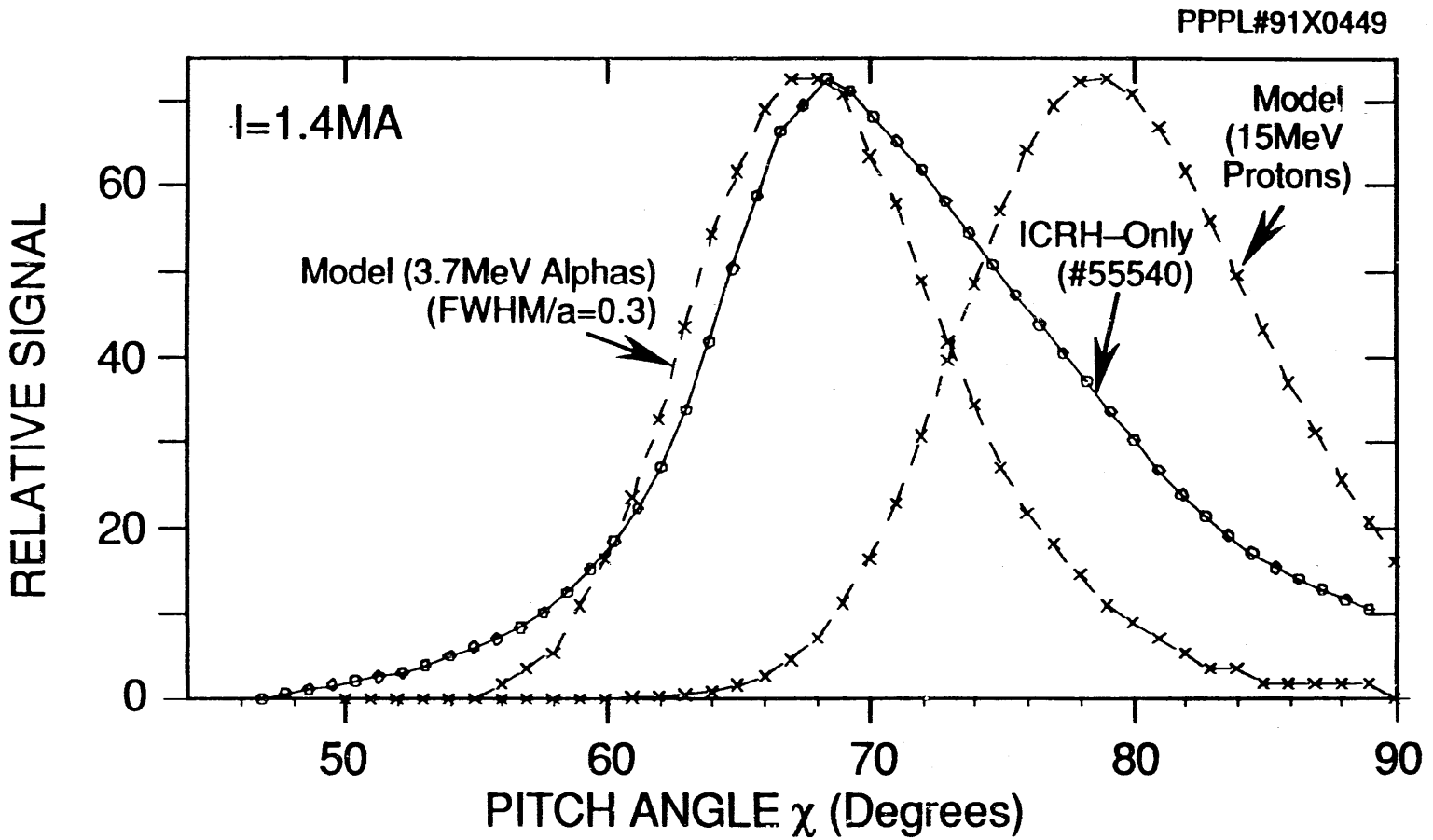
PPPL#91X0449
I=1.4MA
Model (3.7MeV Alphas)
(FWHM/a=0.3)
Model
(15MeV
Protons)
ICRH–Only
(#55540)
RELATIVE SIGNAL
0
20
40
60
50
60
70
80
90
PITCH ANGLE χ (Degrees)

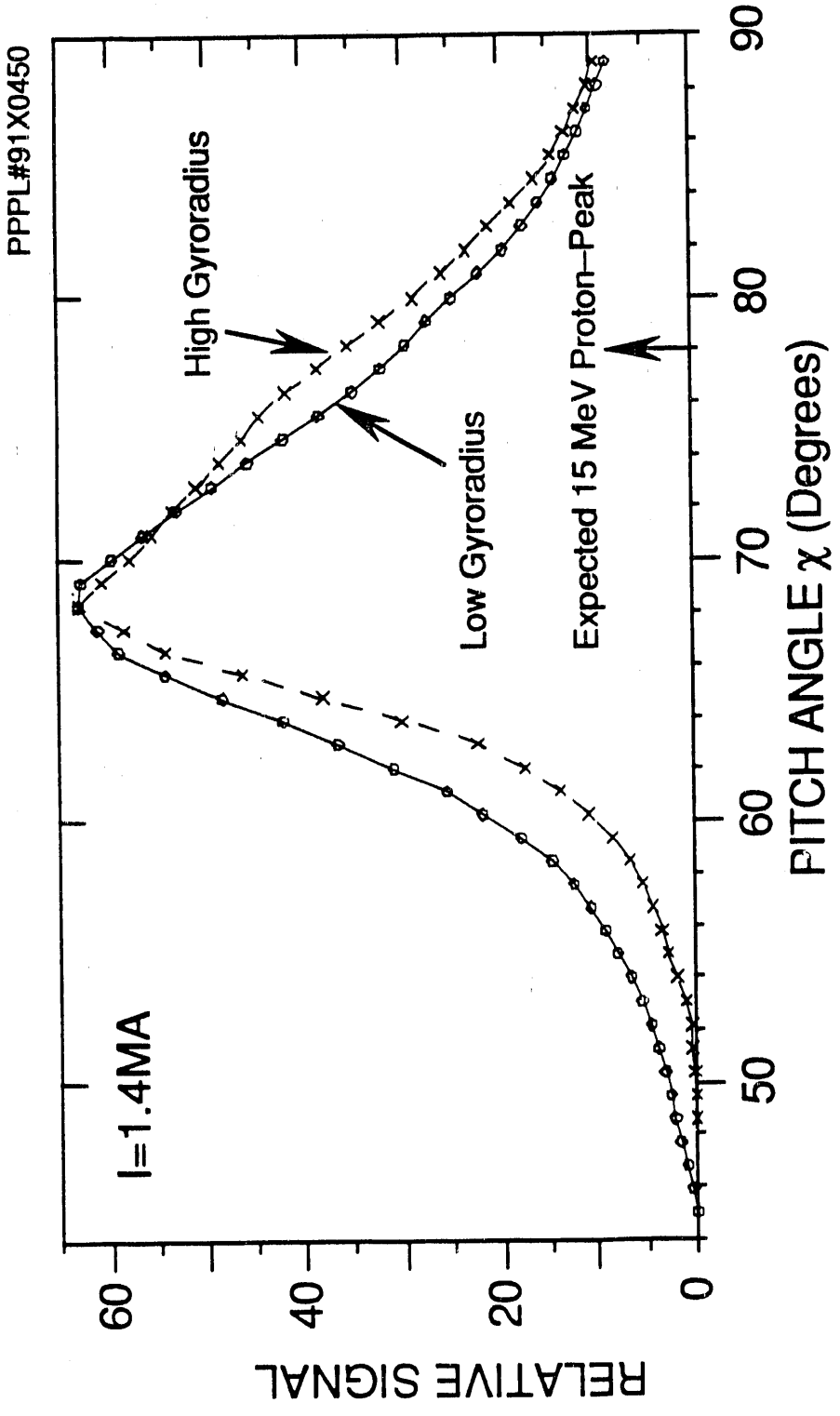
PPPL#91X0450
High Gyroradius
Low Gyroradius
Expected 15 MeV Proton–Peak
I=1.4MA
RELATIVE SIGNAL
0
20
40
60
50
60
70
80
90
PITCH ANGLE χ (Degrees)

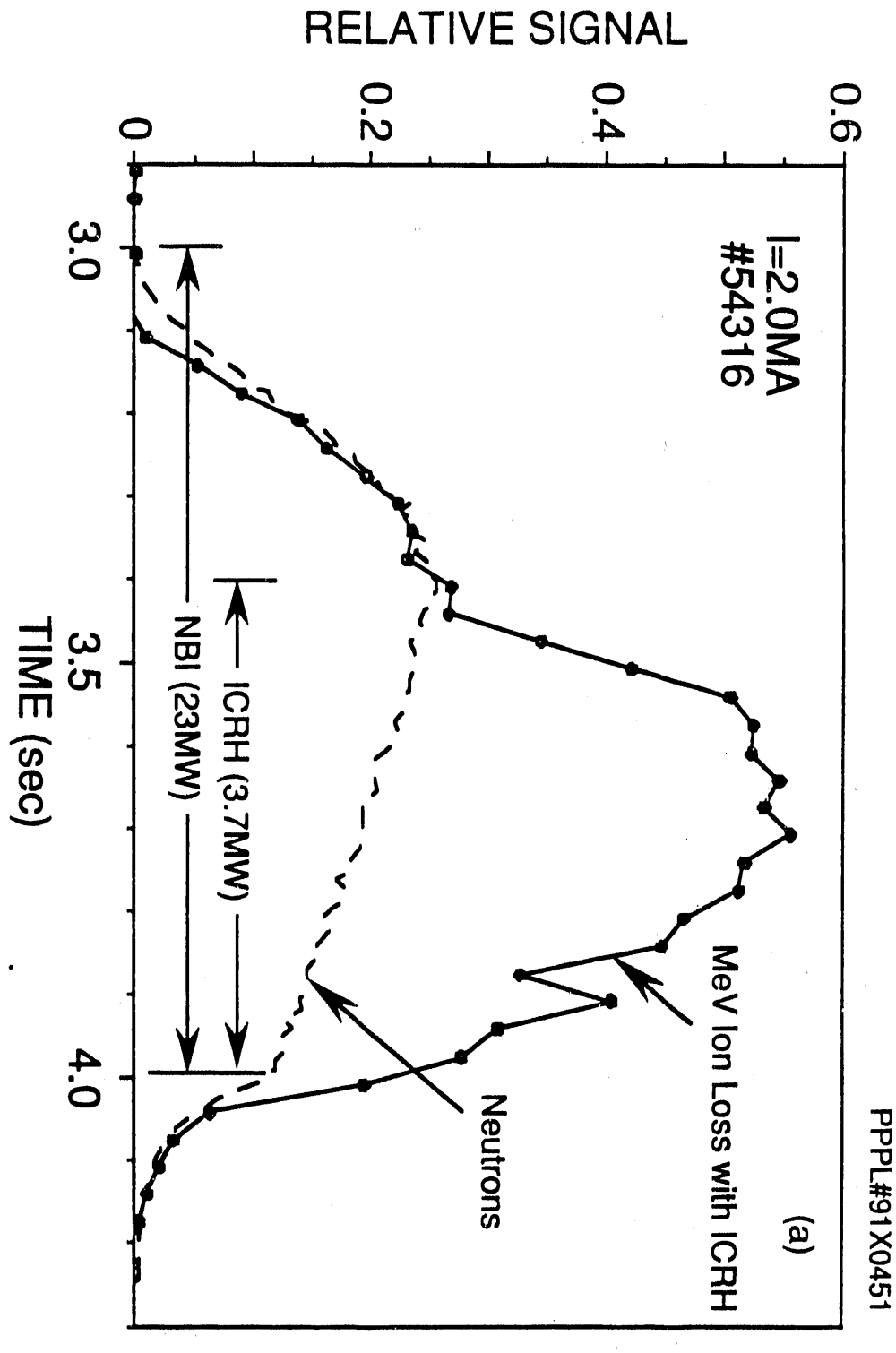
RELATIVE SIGNAL
0
0.2
0.4
0.6
3.0
3.5
4.0
TIME (sec)
I=2.0MA
#54316
NBI (23MW)
ICRH (3.7MW)
MeV Ion Loss with ICRH
Neutrons
(a)
PPPL#91X0451

12(a)

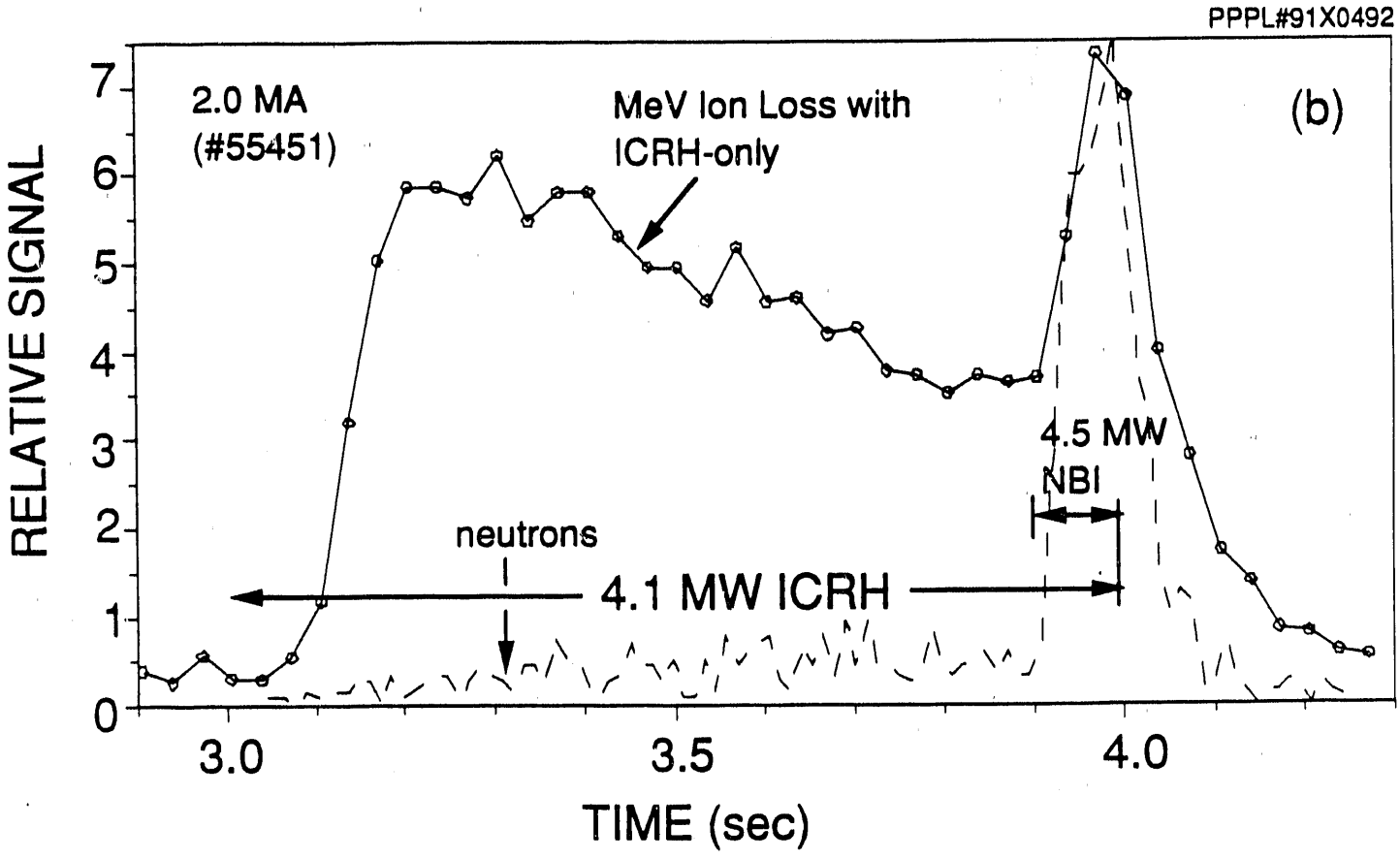
PPPL#91X0492
2.0 MA
(#55451)
MeV Ion Loss with
ICRH-only
(b)
4.5 MW
NBI
neutrons
4.1 MW ICRH
RELATIVE SIGNAL
TIME (sec)
0
1
2
3
4
5
6
7
3.0
3.5
4.0

12(b)

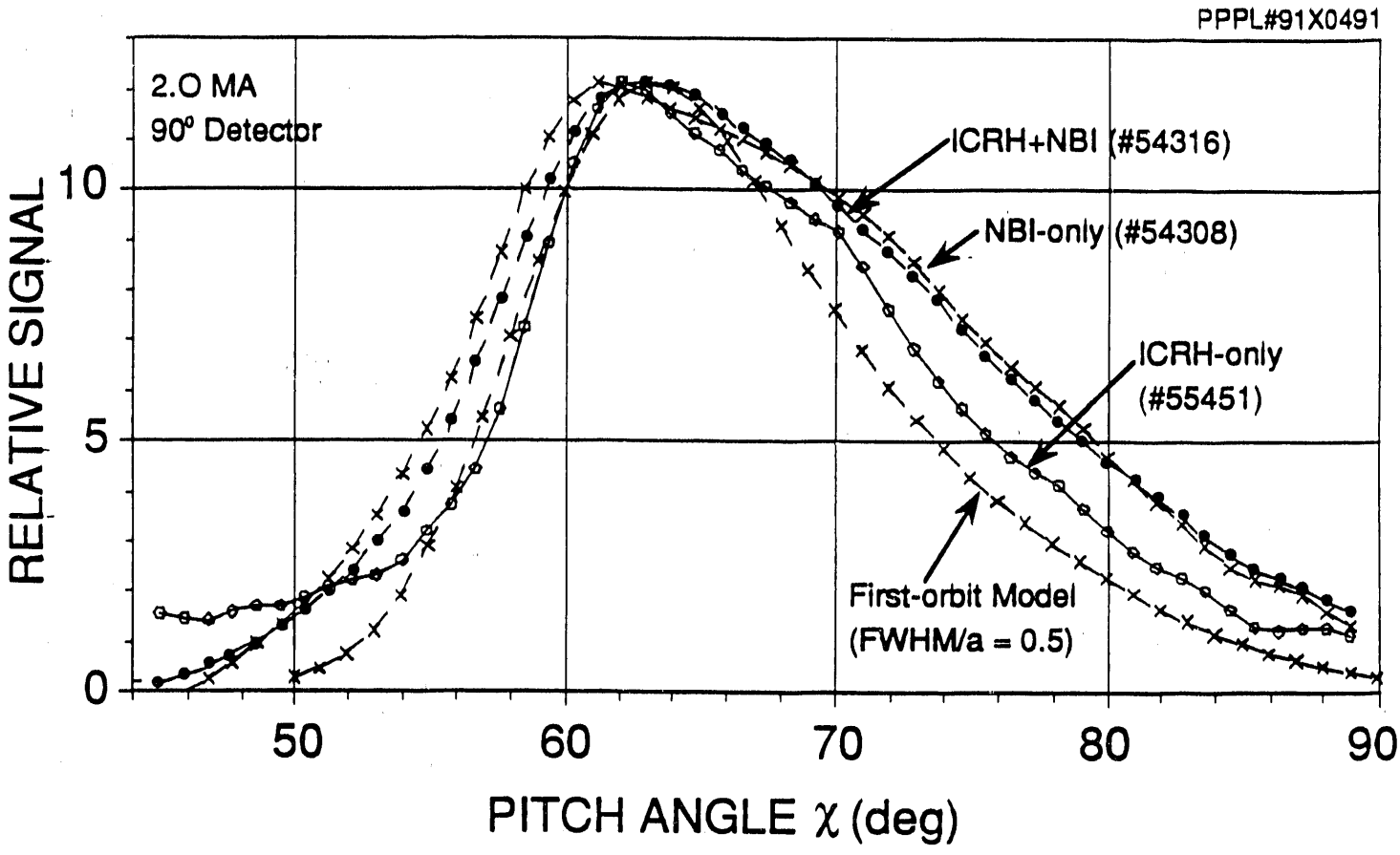
PPPL#91X0491
2.O MA
90° Detector
ICRH+NBI (#54316)
NBI-only (#54308)
ICRH-only
(#55451)
First-orbit Model
(FWHM/a = 0.5)
RELATIVE SIGNAL
0
5
10
50
60
70
80
90
PITCH ANGLE χ (deg)

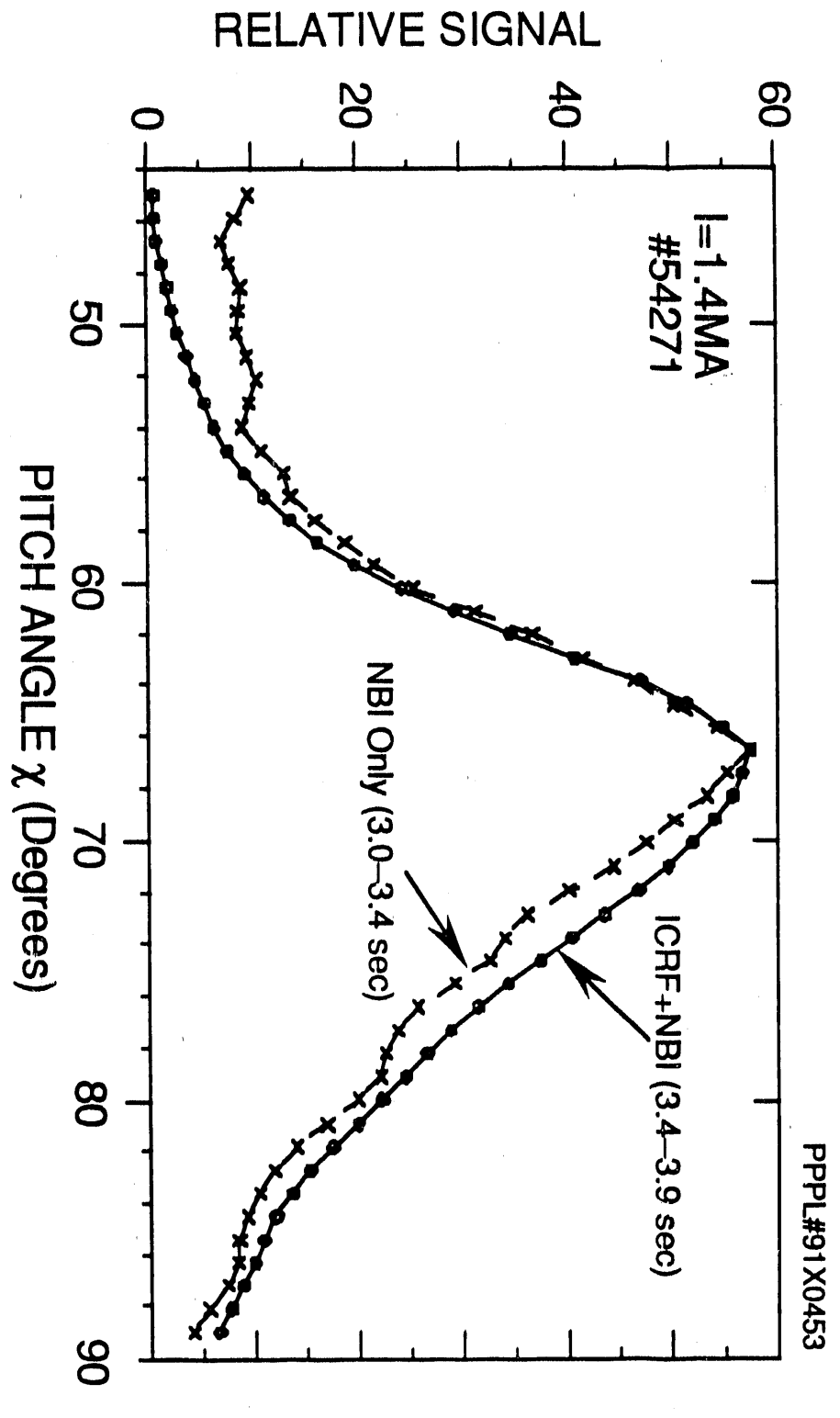
RELATIVE SIGNAL
0
20
40
60
I=1.4MA
#54271
50
60
70
80
90
PITCH ANGLE χ (Degrees)
NBI Only (3.0–3.4 sec)
ICRF+NBI (3.4–3.9 sec)
PPPL#91X0453

14(a)

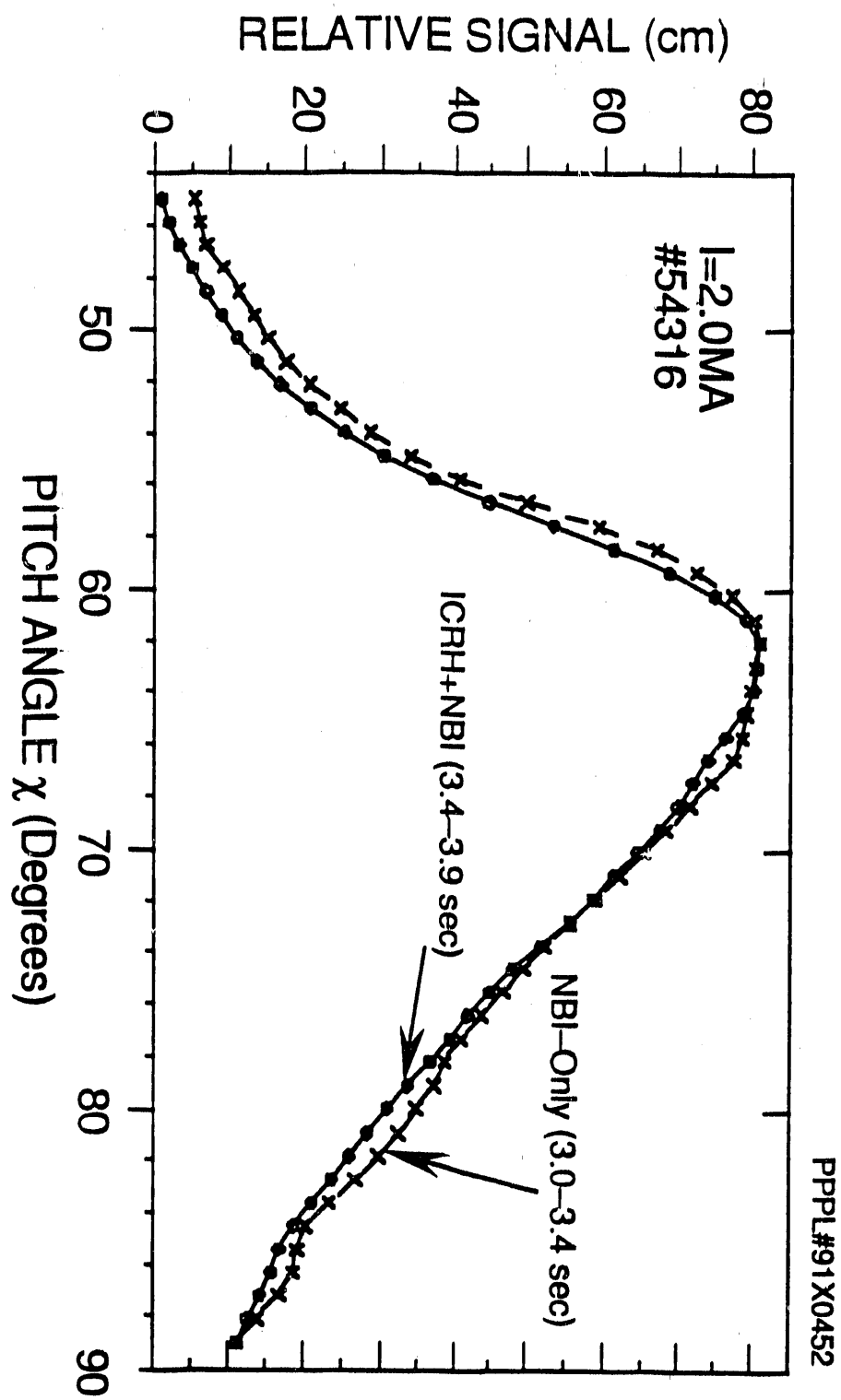
RELATIVE SIGNAL (cm)
0
20
40
60
80
I=2.0MA
#54316
ICRH+NBI (3.4–3.9 sec)
NBI–Only (3.0–3.4 sec)
PPPL#91X0452
50
60
70
80
90
PITCH ANGLE χ (Degrees)

14(b)

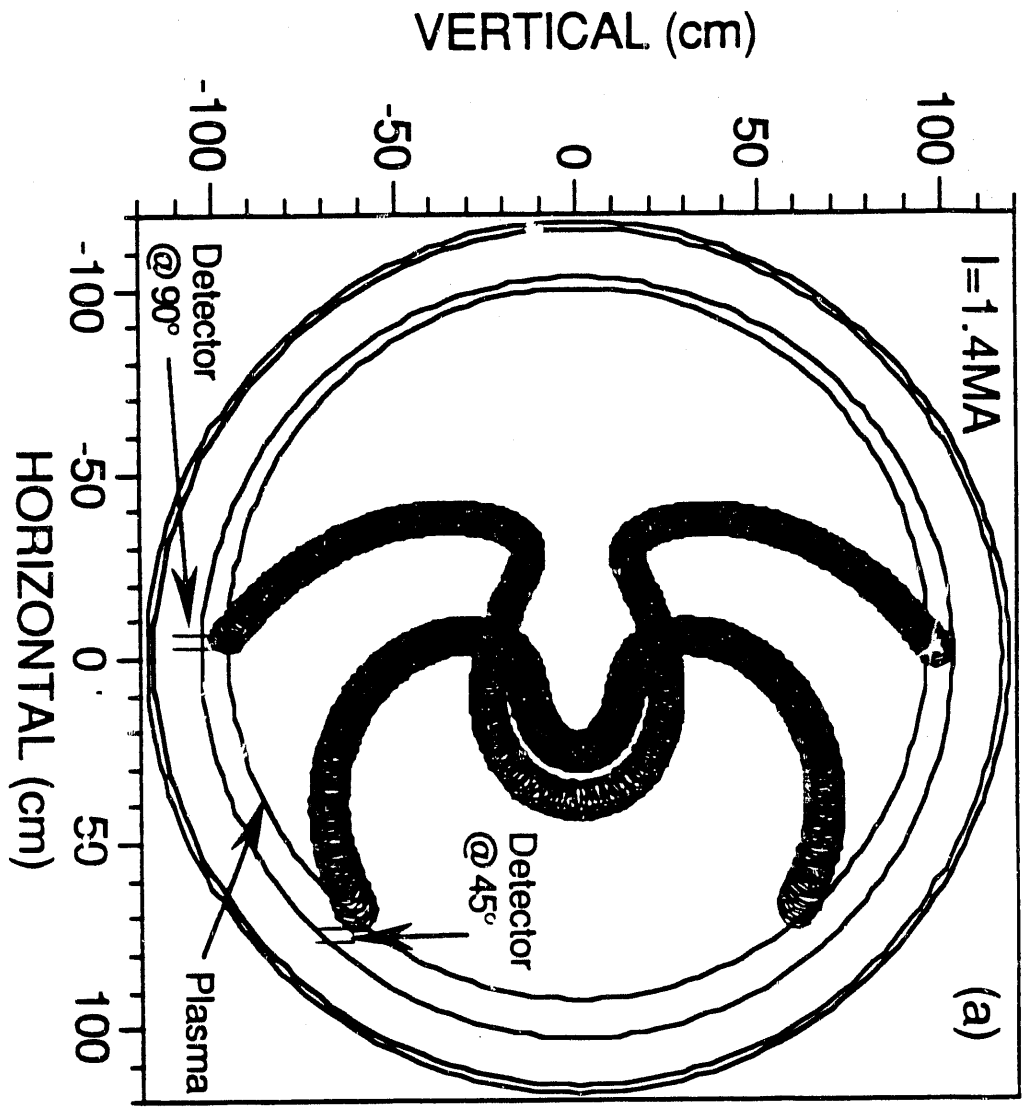
VERTICAL (cm)
-100
-50
0
50
100
HORIZONTAL (cm)
-100
-50
0
50
100
I=1.4MA
(a)
Detector
@ 90°
Detector
@ 45°
Plasma
PPPL#91X0455

15(a)

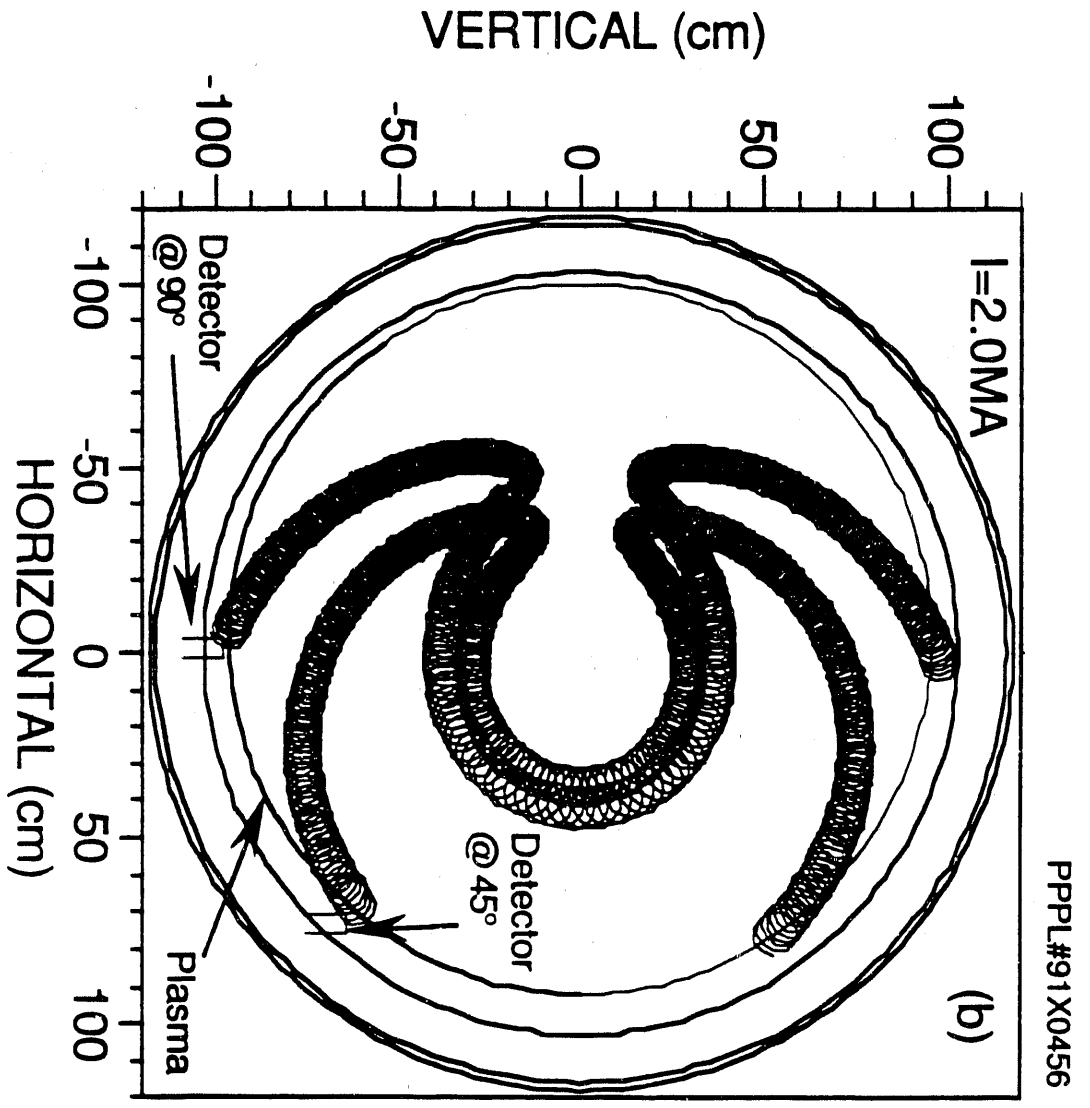
VERTICAL (cm)
-100
-50
0
50
100
I=2.0MA
(b)
Detector
@90°
Detector
@45°
Plasma
HORIZONTAL (cm)
-100
-50
0
50
100
PPPL#91X0456

15(b)

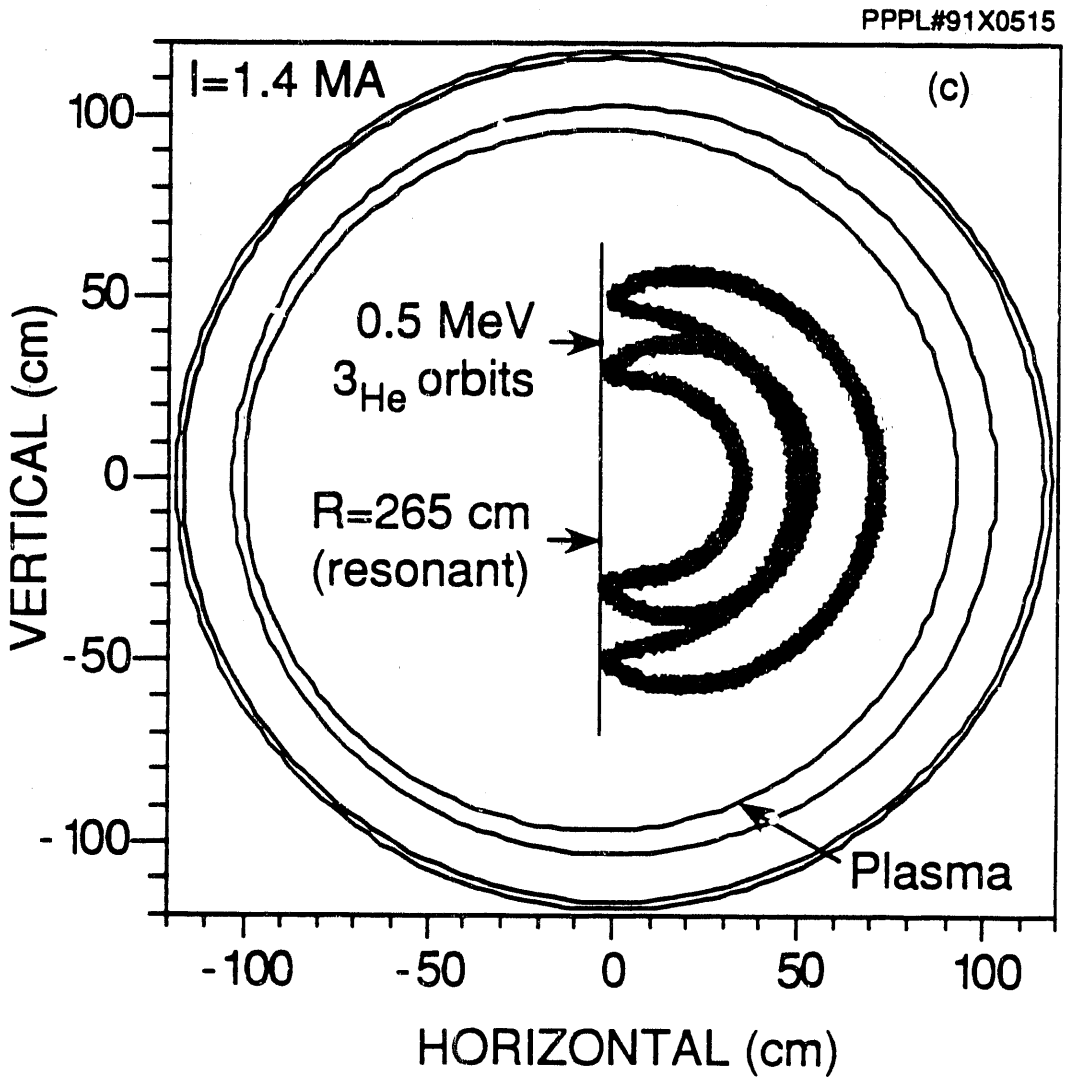
PPPL#91X0515
I=1.4 MA
(c)
0.5 MeV
^{3}He orbits
R=265 cm
(resonant)
Plasma
VERTICAL (cm)
HORIZONTAL (cm)
100
50
0
-50
-100
-100
-50
0
50
100

15(c)

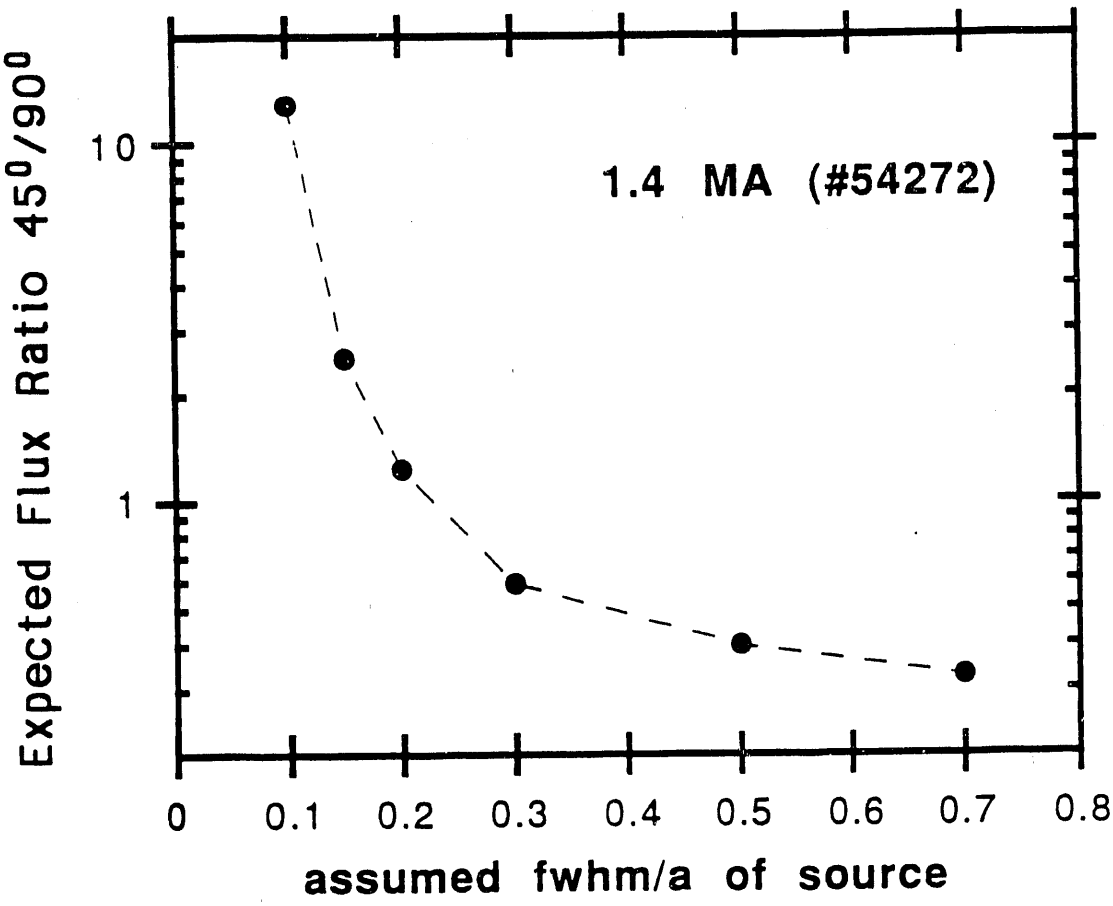
Expected Flux Ratio 45⁰/90⁰
10
1
1.4 MA (#54272)
0
0.1
0.2
0.3
0.4
0.5
0.6
0.7
0.8
assumed fwhm/a of source

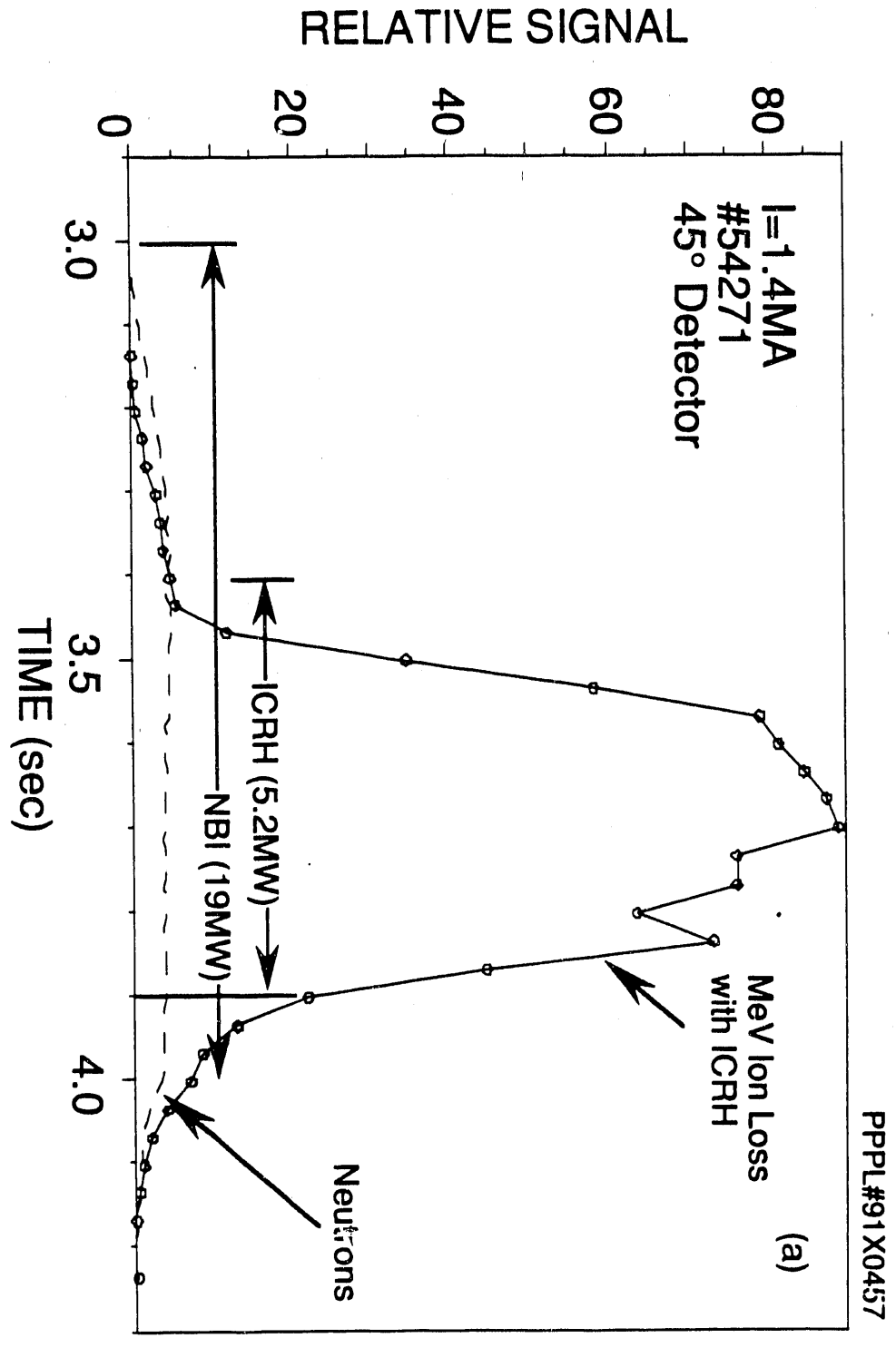
RELATIVE SIGNAL
0
20
40
60
80
I=1.4MA
#54271
45° Detector
(a)
MeV Ion Loss
with ICRH
Neutrons
ICRH (5.2MW)
NBI (19MW)
3.0
3.5
4.0
TIME (sec)
PPPL#91X0457

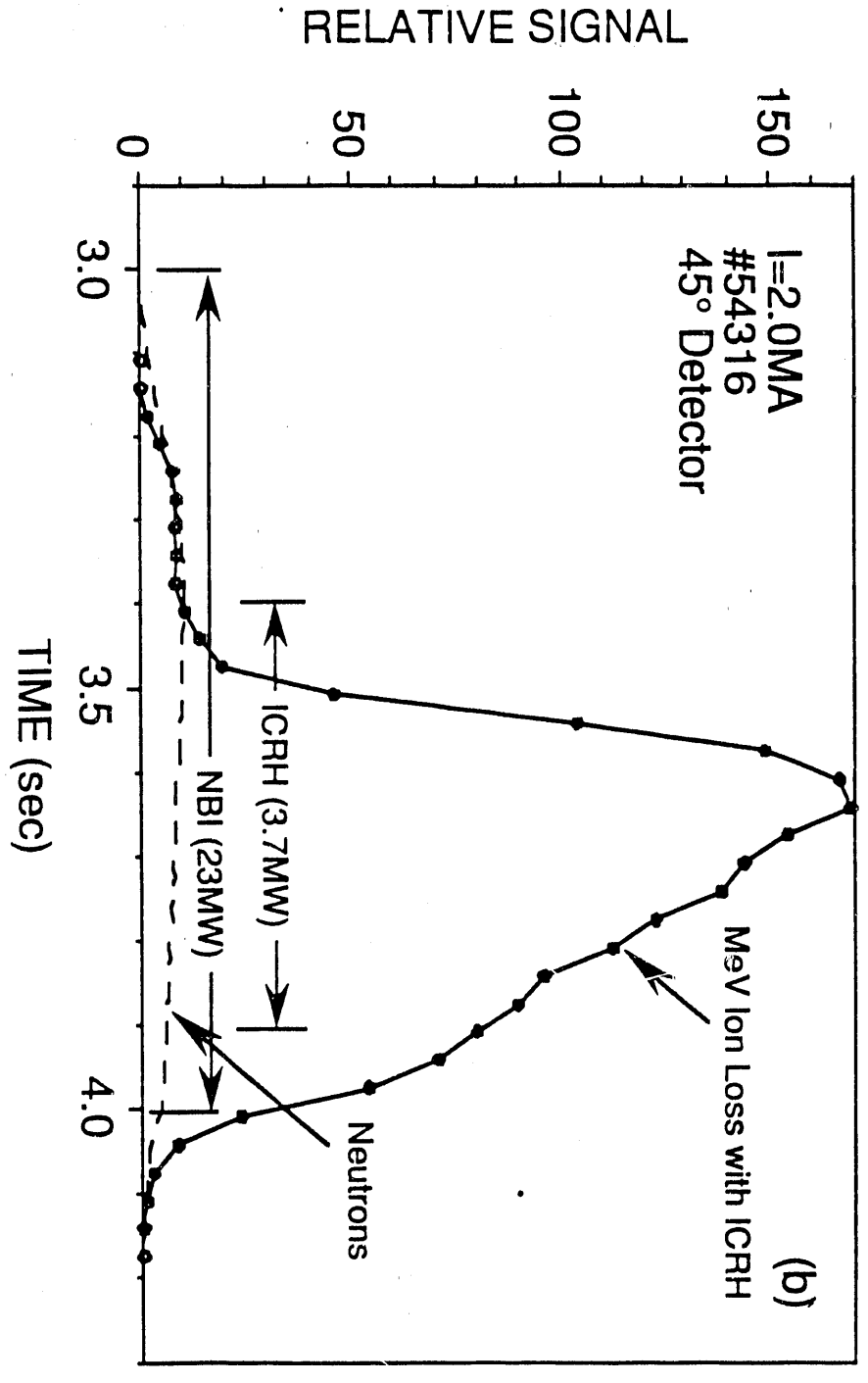
RELATIVE SIGNAL
150
100
50
0
3.0
3.5
4.0
TIME (sec)
I=2.0MA
#54316
45° Detector
(b)
MeV Ion Loss with ICRH
Neutrons
ICRH (3.7MW)
NBI (23MW)
PPPL#91X0458

17(b)

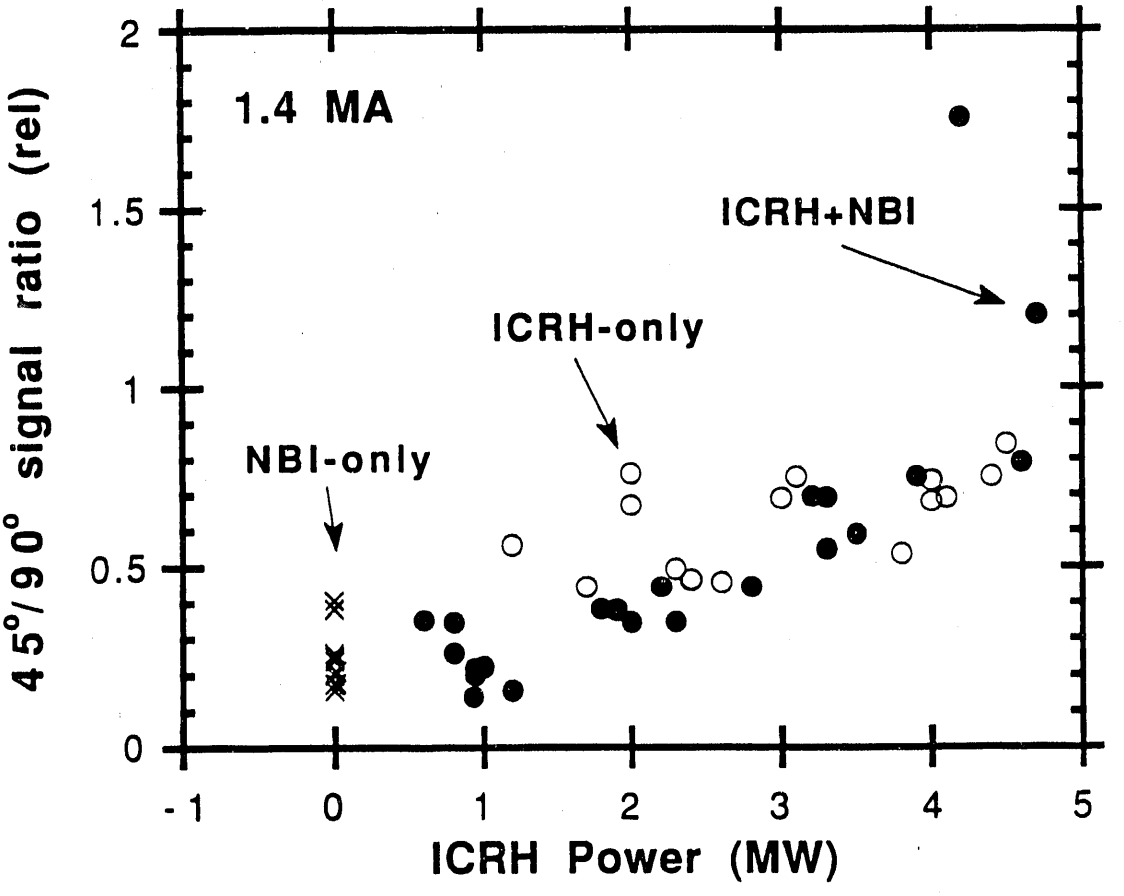
1.4 MA
ICRH+NBI
ICRH-only
NBI-only
45°/90° signal ratio (rel)
ICRH Power (MW)
2
1.5
1
0.5
0
-1
0
1
2
3
4
5

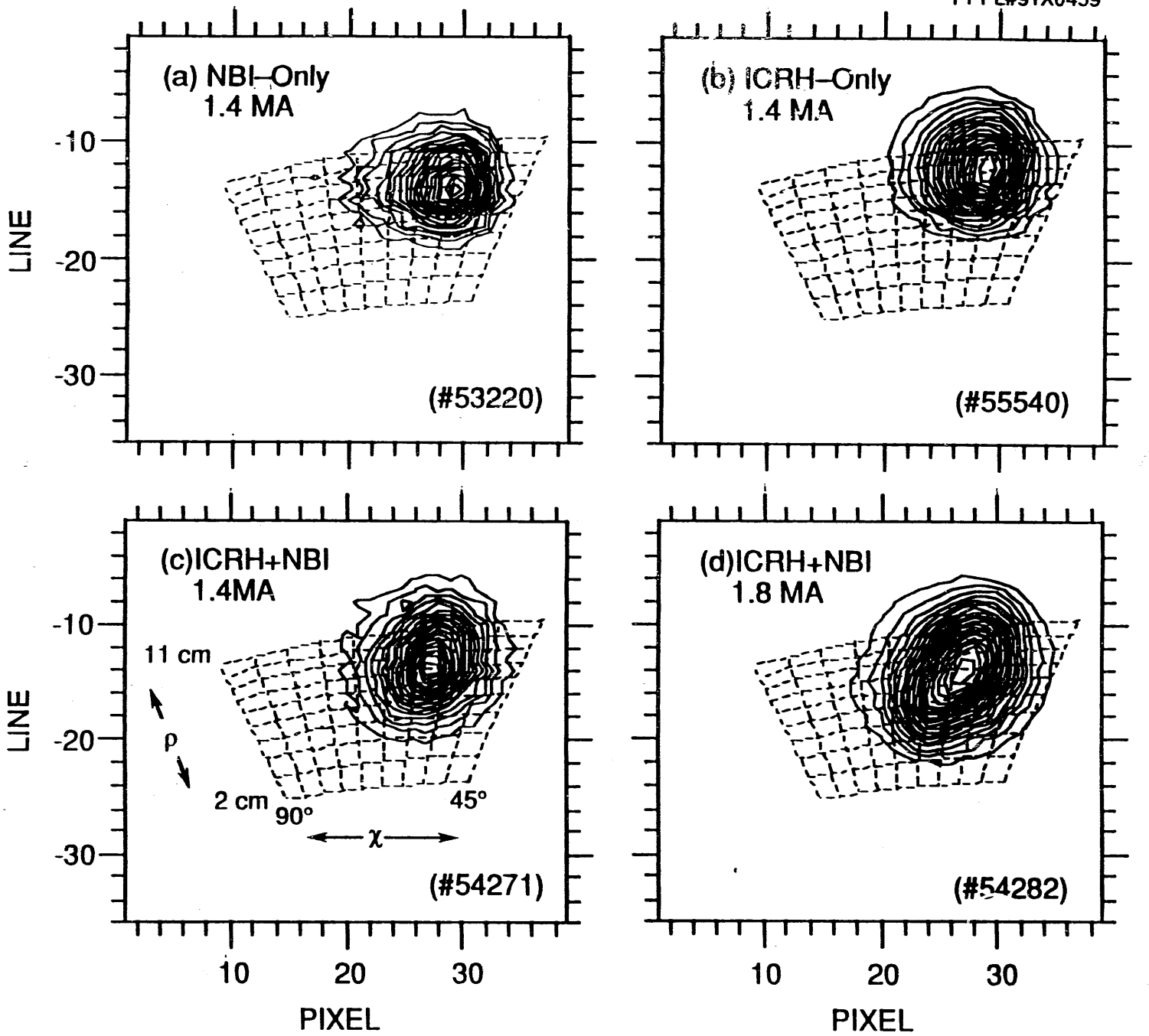
(a) NBI–Only
1.4 MA
(#53220)
(b) ICRH–Only
1.4 MA
(#55540)
(c)ICRH+NBI
1.4MA
11 cm
ρ
2 cm
90°
45°
χ
(#54271)
(d)ICRH+NBI
1.8 MA
(#54282)
LINE
-10
-20
-30
10
20
30
PIXEL

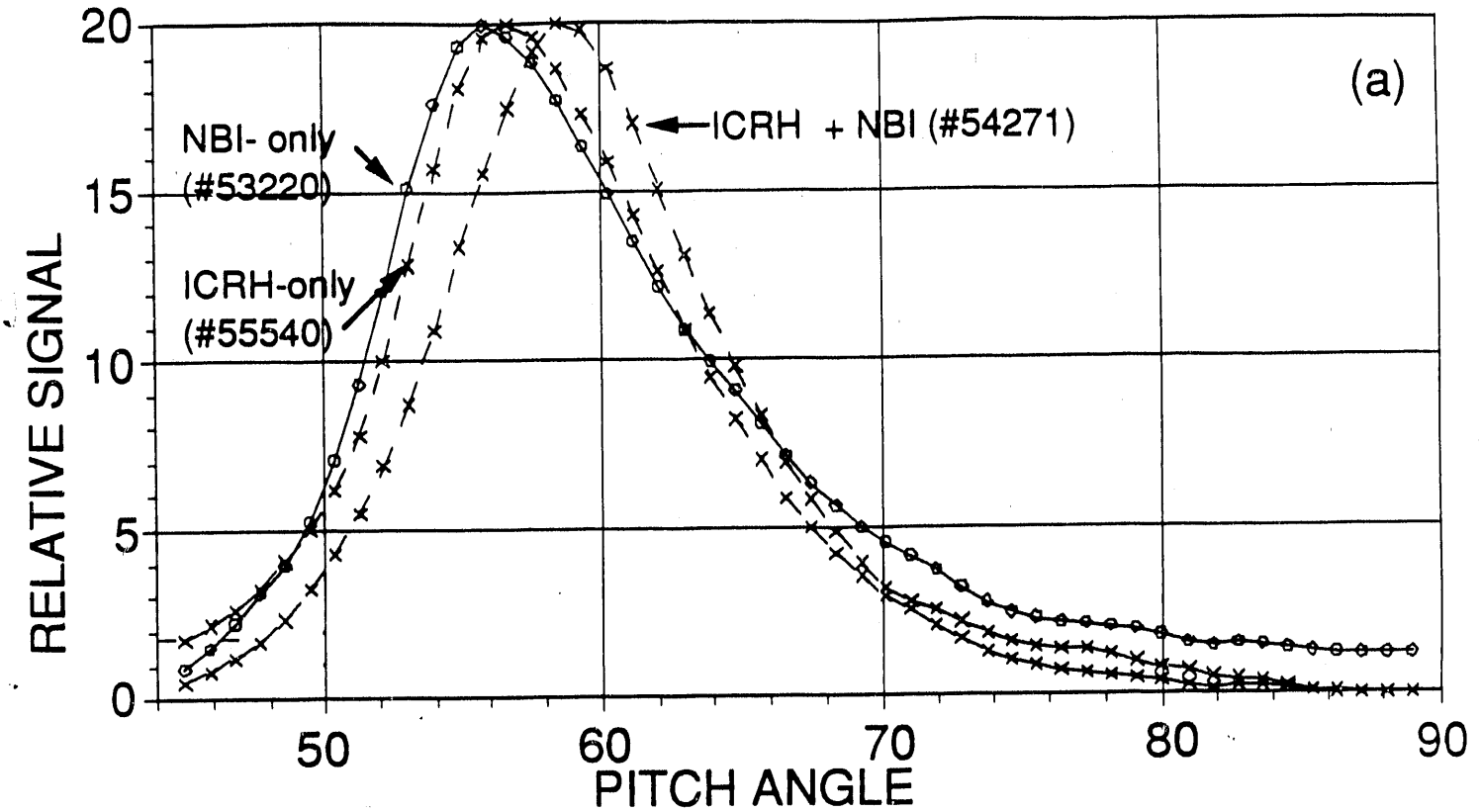
(a)
NBI- only
(#53220)
ICRH-only
(#55540)
ICRH + NBI (#54271)
RELATIVE SIGNAL
PITCH ANGLE
0
5
10
15
20
50
60
70
80
90

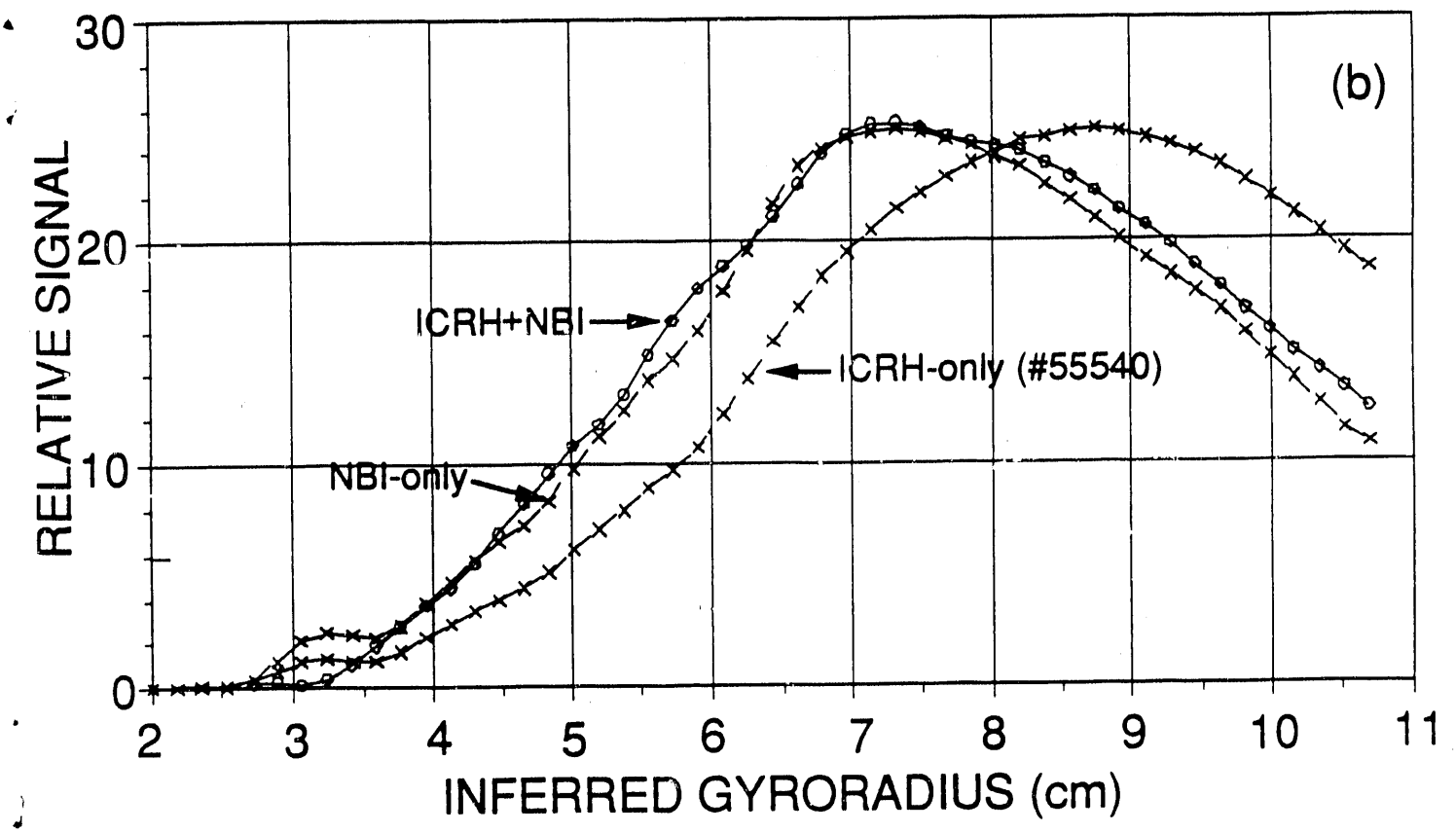
(b)
ICRH+NBI
ICRH-only (#55540)
NBI-only
RELATIVE SIGNAL
INFERRED GYRORADIUS (cm)
0
10
20
30
2
3
4
5
6
7
8
9
10
11

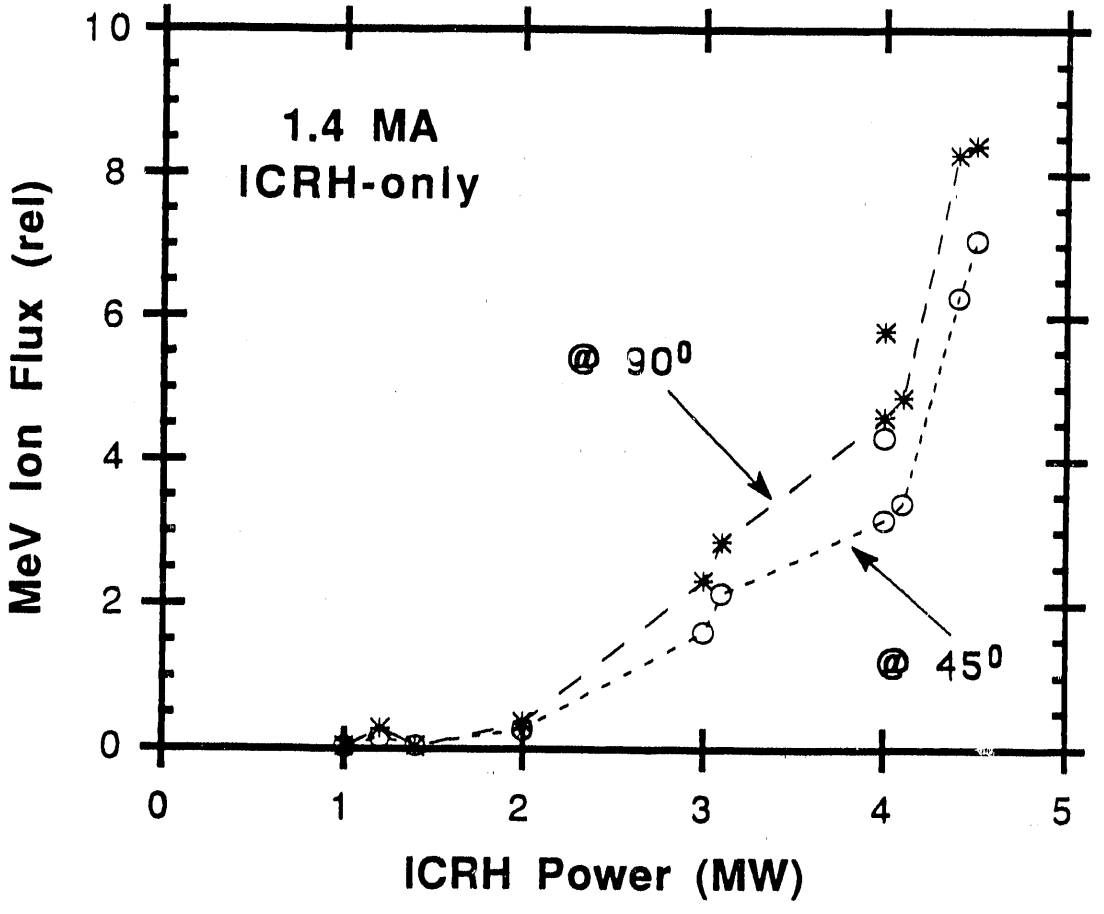
1.4 MA
ICRH-only
@ 90⁰
@ 45⁰
MeV Ion Flux (rel)
ICRH Power (MW)
0
2
4
6
8
10
0
1
2
3
4
5

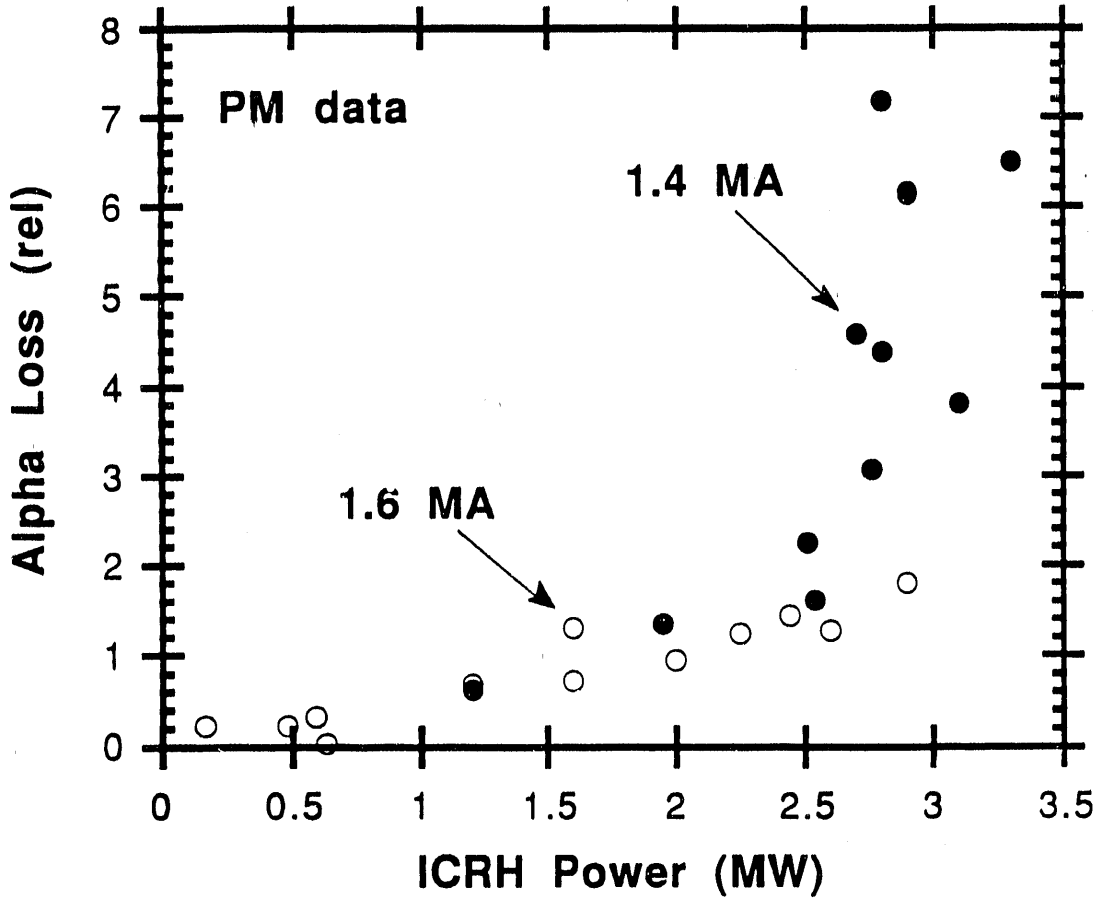
PM data
1.4 MA
1.6 MA
Alpha Loss (rel)
ICRH Power (MW)
0
1
2
3
4
5
6
7
8
0
0.5
1
1.5
2
2.5
3
3.5

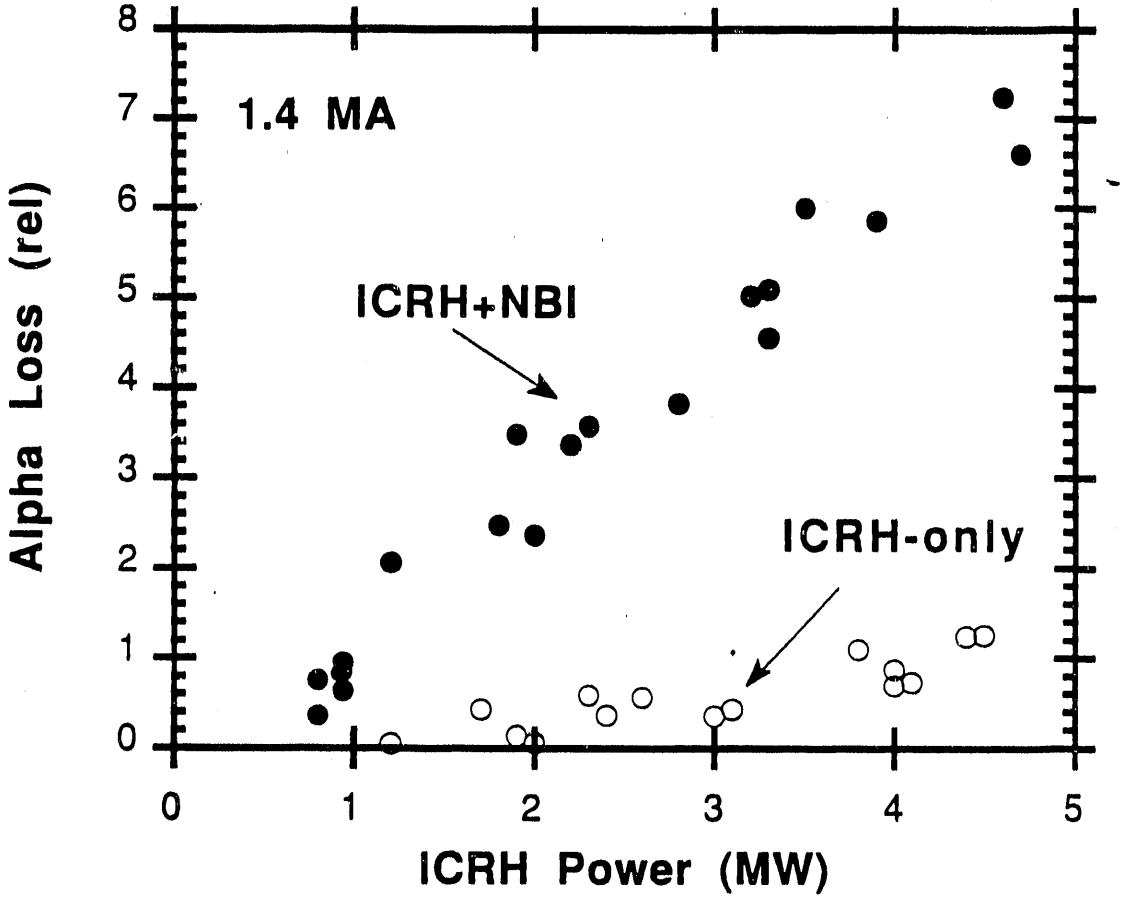
1.4 MA
ICRH+NBI
ICRH-only
Alpha Loss (rel)
ICRH Power (MW)
0
1
2
3
4
5
6
7
8

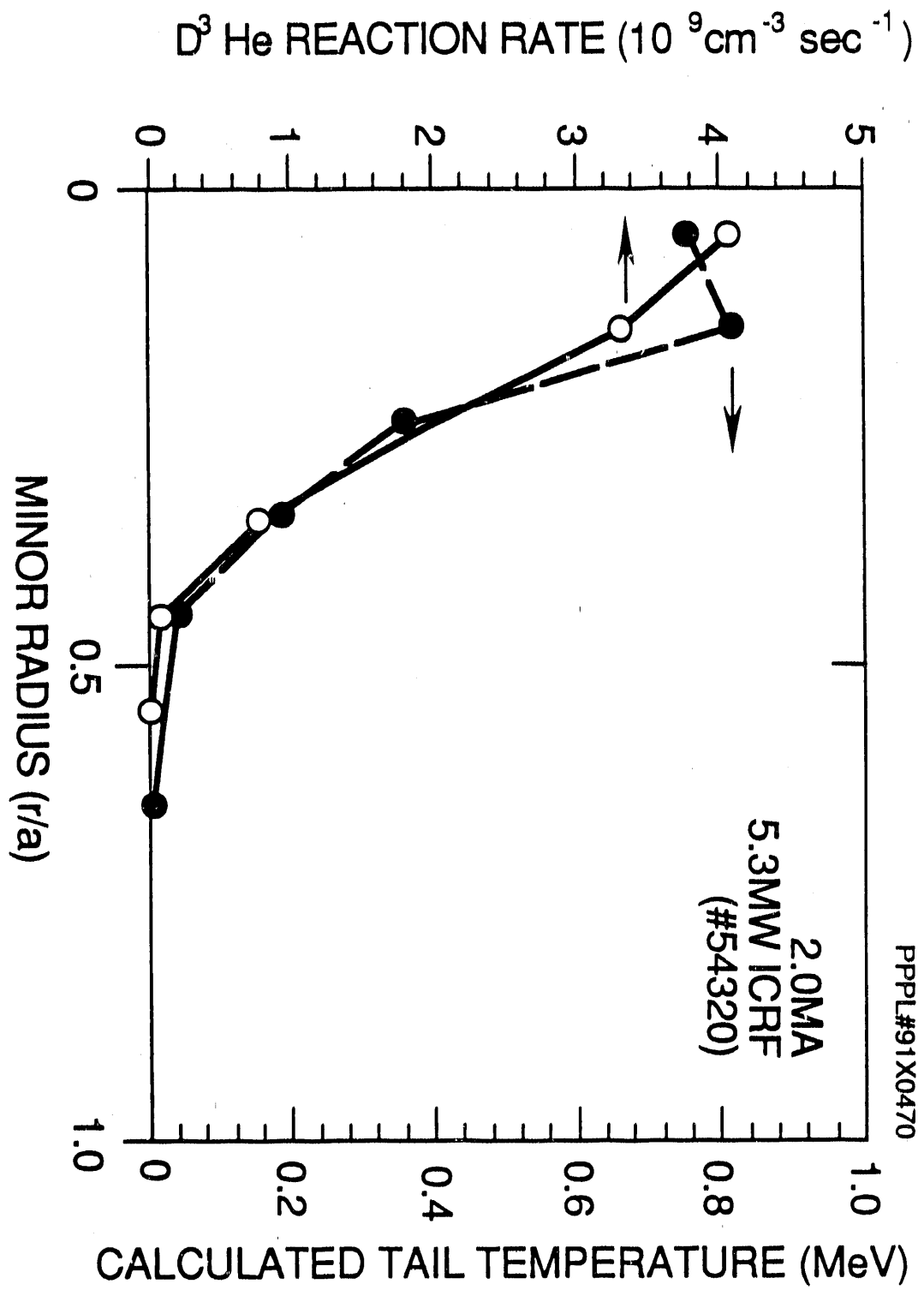
D3 He REACTION RATE (10 9cm-3 sec-1)
0
1
2
3
4
5
0
0.5
1.0
MINOR RADIUS (r/a)
0
0.2
0.4
0.6
0.8
1.0
CALCULATED TAIL TEMPERATURE (MeV)
2.0MA
5.3MW ICRF
(#54320)
PPPL#91X0470

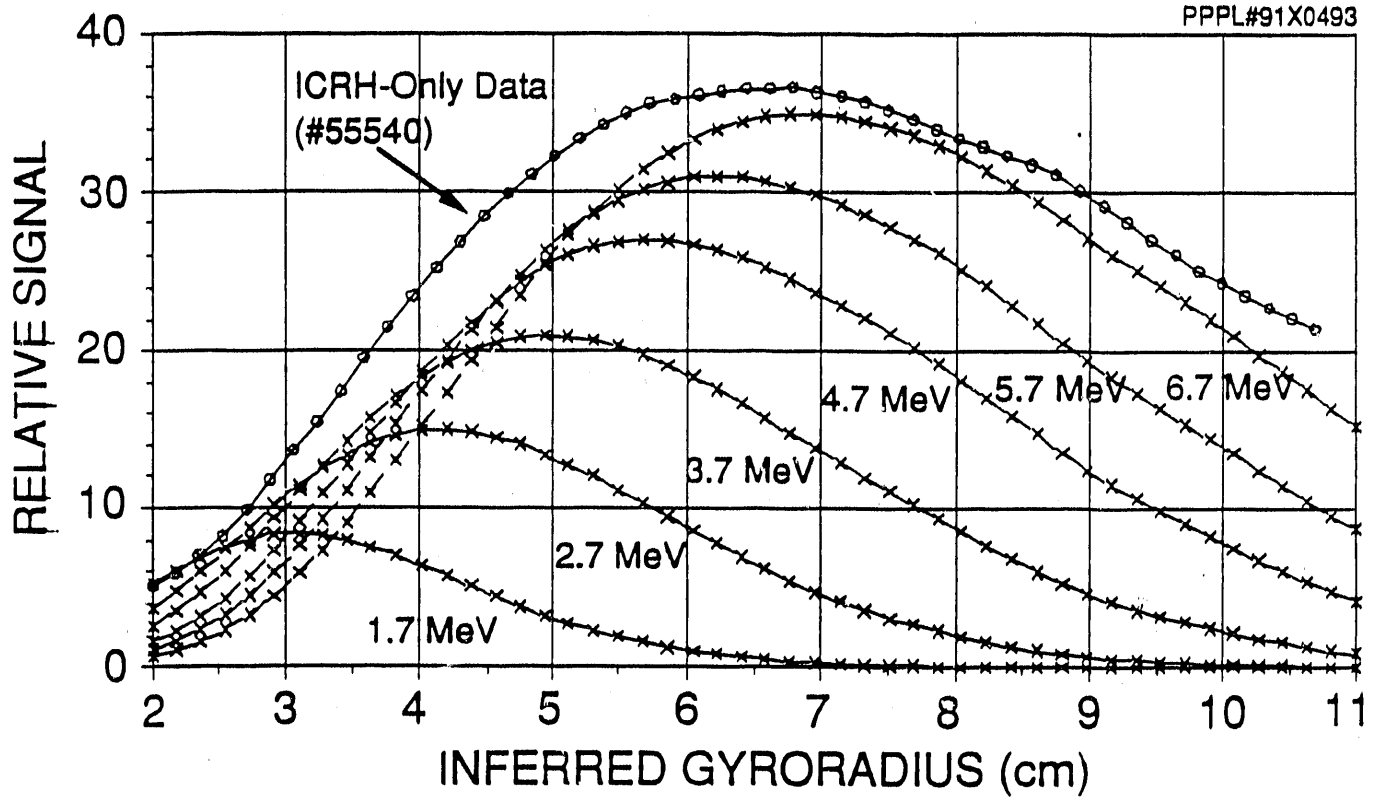
PPPL#91X0493
ICRH-Only Data
(#55540)
4.7 MeV
5.7 MeV
6.7 MeV
3.7 MeV
2.7 MeV
1.7 MeV
RELATIVE SIGNAL
INFERRED GYRORADIUS (cm)
0
10
20
30
40
2
3
4
5
6
7
8
9
10
11

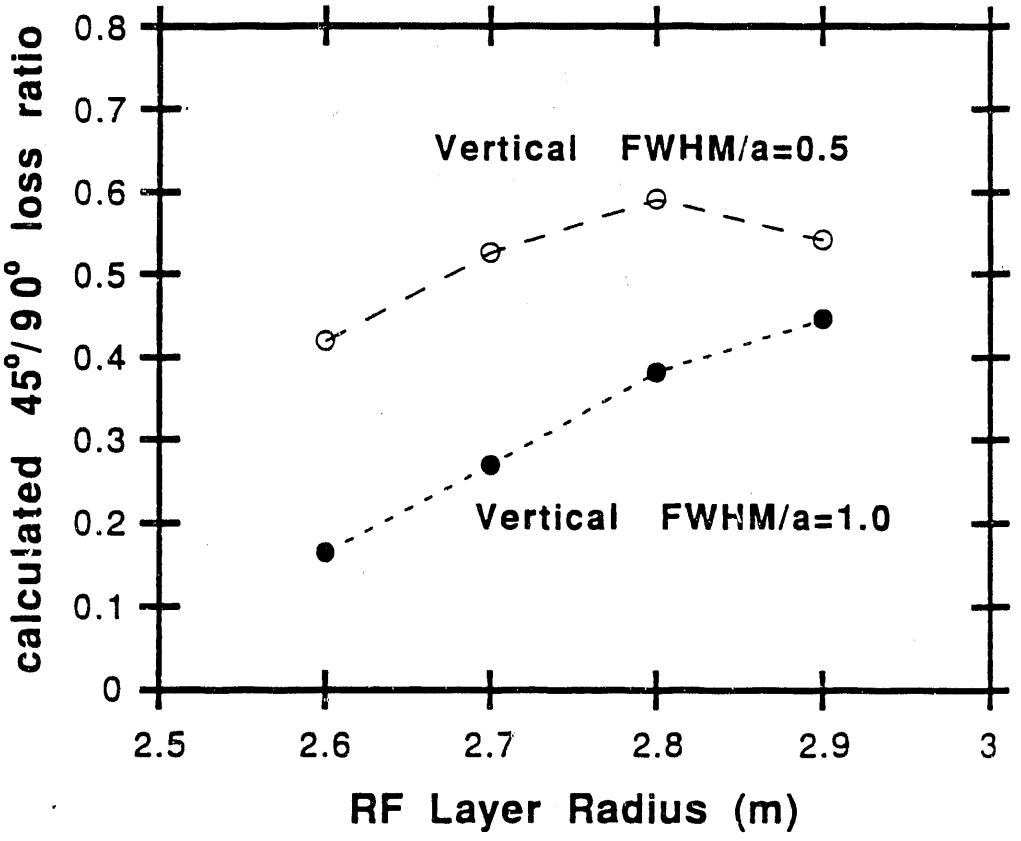
calculated 45°/90° loss ratio
0.8
0.7
0.6
0.5
0.4
0.3
0.2
0.1
0
Vertical FWHM/a=0.5
Vertical FWHM/a=1.0
2.5
2.6
2.7
2.8
2.9
3
RF Layer Radius (m)

EXTERNAL DISTRIBUTION IN ADDITION TO UC-420

Dr. F. Paoloni, Univ. of Wollongong, AUSTRALIA
Prof. M.H. Brennan, Univ. of Sydney, AUSTRALIA
Plasma Research Lab., Australian Nat. Univ., AUSTRALIA
Prof. I.R. Jones, Flinders Univ, AUSTRALIA
Prof. F. Cap, Inst. for Theoretical Physics, AUSTRIA
Prof. M. Heindler, Institut für Theoretische Physik, AUSTRIA
Prof. M. Goossens, Astronomisch Instituut, BELGIUM
Ecole Royale Militaire, Lab. de Phy. Plasmas, BELGIUM
Commission-European, DG. XII-Fusion Prog., BELGIUM
Prof. R. Boucique, Rijksuniversiteit Gent, BELGIUM
Dr. P.H. Sakanaka, Instituto Fisica, BRAZIL
Instituto Nacional De Pesquisas Espaciais-INPE, BRAZIL
Documents Office, Atomic Energy of Canada Ltd., CANADA
Dr. M.P. Bachynski, MPB Technologies, Inc., CANADA
Dr. H.M. Skarsgard, Univ. of Saskatchewan, CANADA
Prof. J. Teichmann, Univ. of Montreal, CANADA
Prof. S.R. Sreenivasan, Univ. of Calgary, CANADA
Prof. T.W. Johnston, INRS-Energie, CANADA
Dr. R. Bolton, Centre canadien de fusion magnétique, CANADA
Dr. C.R. James,, Univ. of Alberta, CANADA
Dr. P. Lukác, Komenského Universzita, CZECHO-SLOVAKIA
The Librarian, Culham Laboratory, ENGLAND
Library, R61, Rutherford Appleton Laboratory, ENGLAND
Mrs. S.A. Hutchinson, JET Library, ENGLAND
Dr. S.C. Sharma, Univ. of South Pacific, FIJI ISLANDS
P. Mähönen, Univ. of Helsinki, FINLAND
Prof. M.N. Bussac, Ecole Polytechnique,, FRANCE
C. Mouttet, Lab. de Physique des Milieux Ionisés, FRANCE
J. Radet, CEN/CADARACHE - Bat 506, FRANCE
Prof. E. Economou, Univ. of Crete, GREECE
Ms. C. Rinni, Univ. of Ioannina, GREECE
Dr. T. Mual, Academy Bibliographic Ser., HONG KONG
Preprint Library, Hungarian Academy of Sci., HUNGARY
Dr. B. DasGupta, Saha Inst. of Nuclear Physics, INDIA
Dr. P. Kaw, Inst. for Plasma Research, INDIA
Dr. P. Rosenau, Israel Inst. of Technology, ISRAEL
Librarian, International Center for Theo Physics, ITALY
Miss C. De Palo, Associazione EURATOM-ENEA , ITALY
Dr. G. Grosso, Istituto di Fisica del Plasma, ITALY
Prof. G. Rostangni, Istituto Gas Ionizzati Del Cnr, ITALY
Dr. H. Yamato, Toshiba Res & Devel Center, JAPAN
Prof. I. Kawakami, Hiroshima Univ., JAPAN
Prof. K. Nishikawa, Hiroshima Univ., JAPAN
Director, Japan Atomic Energy Research Inst., JAPAN
Prof. S. Itoh, Kyushu Univ., JAPAN
Research Info. Ctr., National Instit. for Fusion Science, JAPAN
Prof. S. Tanaka, Kyoto Univ., JAPAN
Library, Kyoto Univ., JAPAN
Prof. N. Inoue, Univ. of Tokyo, JAPAN
Secretary, Plasma Section, Electrotechnical Lab., JAPAN
S. Mori, Technical Advisor, JAERI, JAPAN
Dr. O. Mitarai, Kumamoto Inst. of Technology, JAPAN
J. Hyeon-Sook, Korea Atomic Energy Research Inst., KOREA
D.I. Choi, The Korea Adv. Inst. of Sci. & Tech., KOREA
Prof. B.S. Liley, Univ. of Waikato, NEW ZEALAND
Inst of Physics, Chinese Acad Sci PEOPLE'S REP. OF CHINA
Library, Inst. of Plasma Physics, PEOPLE'S REP. OF CHINA
Tsinghua Univ. Library, PEOPLE'S REPUBLIC OF CHINA
Z. Li, S.W. Inst Physics, PEOPLE'S REPUBLIC OF CHINA
Prof. J.A.C. Cabral, Instituto Superior Tecnico, PORTUGAL
Dr. O. Petrus, AL I CUZA Univ., ROMANIA
Dr. J. de Villiers, Fusion Studies, AEC, S. AFRICA
Prof. M.A. Hellberg, Univ. of Natal, S. AFRICA
Prof. D.E. Kim, Pohang Inst. of Sci. & Tech., SO. KOREA
Prof. C.I.E.M.A.T, Fusion Division Library, SPAIN
Dr. L. Stenflo, Univ. of UMEA, SWEDEN
Library, Royal Inst. of Technology, SWEDEN
Prof. H. Wilhelmson, Chalmers Univ. of Tech., SWEDEN
Centre Phys. Des Plasmas, Ecole Polytech, SWITZERLAND
Bibliotheek, Inst. Voor Plasma-Fysica, THE NETHERLANDS
Asst. Prof. Dr. S. Cakir, Middle East Tech. Univ., TURKEY
Dr. V.A. Glukhikh,Sci. Res. Inst. Electrophys.I Apparatus, USSR
Dr. D.D. Ryutov, Siberian Branch of Academy of Sci., USSR
Dr. G.A. Eliseev, I.V. Kurchatov Inst., USSR
Librarian, The Ukr.SSR Academy of Sciences, USSR
Dr. L.M. Kovrizhnykh, Inst. of General Physics, USSR
Kernforschungsanlage GmbH, Zentralbibliothek, W. GERMANY
Bibliothek, Inst. Für Plasmaforschung, W. GERMANY
Prof. K. Schindler, Ruhr-Universität Bochum, W. GERMANY
Dr. F. Wagner, (ASDEX), Max-Planck-Institut, W. GERMANY
Librarian, Max-Planck-Institut, W. GERMANY
Prof. R.K. Janev, Inst. of Physics, YUGOSLAVIA

END

DATE FILMED

3/3/92